Simulation of Compressible Gas-Liquid Flows in Physical Cleaning Applications: High-Speed Droplet Impact and Bubble Collapse

February 2019

Tomoki Kondo

Simulation of Compressible Gas-Liquid Flows in Physical Cleaning Applications: High-Speed Droplet Impact and Bubble Collapse

Thesis by

Tomoki Kondo

In Partial Fulfillment of the Requirements
for the Degree of
Doctor of Philosophy in Engineering

Graduate School of Science and Technology

Keio University

February 2019

Tomoki Kondo
ORCID: 0000-0003-2570-1324

論文要旨

本論文では，液体ジェット洗浄および超音波洗浄に代表される流体物理洗浄技術の洗浄メカニズム解明を目的として，高速液滴衝突および気泡崩壊に関する直接数値解析を実行する．それらに付随する音響現象（キャビテーション，衝撃波伝ぱ）と粘性現象（壁面せん断流の形成）を定量評価し，エロージョン (表面壊食) と付着粒子除去性能の観点から考察する．

第一に，高速液滴衝突に付随するキャビテーションによるエロージョンの影響を評価するための圧縮性・非粘性解析を行う．理論上，液滴内部を伝ぱする水撃衝撃波は液滴界面（音響インピーダンス不連続面）との干渉により負圧領域を生じるためキャビテーションは発生し得るが，この現象を数値的に再現した研究例はない．キャビテーションの評価には相変化を考慮しない液滴衝突の数値解析から液相圧力履歴を取得し，それを Rayleigh–Plesset 型方程式に入力することで，ある初期気泡核の運動を解析する．すなわち，one-way-coupling に基づく数値解析を行う．解析の結果キャビテーションの発生は数値的に確認され，そのキャビテーション気泡崩壊に伴う音響放射は，衝突に伴う水撃圧を上回る可能性が示された．

第二に，高速液滴衝突が壁面上にもたらす水撃圧および壁面せん断流の形成を評価する圧縮性・粘性解析を行う．ここでは乾燥壁面並びに液膜で覆われた壁面への衝突を考慮し，乾燥壁面への衝突では壁面せん断流の形成を再現するため，三相が接触する移動界面を正確に捉えるための滑り壁モデルを適用する．せん断流による粒子はく離を評価するためには，粒子がせん断流から受ける表面応力トルクとファンデルワールス力のトルクの比較に基づき，壁面せん断応力分布を粒子はく離の可能性を予測する無次元パラメータ分布へ写像する手法を提案する．本研究は液滴衝突による壁面せん断流形成が物理洗浄メカニズムに大きく寄与することを確認した．加えて壁面上の液膜厚さに依存する水撃圧・壁面せん断応力の減衰率をモデル化した．

最後に，壁面近傍気泡の非球形崩壊に伴うマイクロジェットの形成および壁面せん断流の形成を評価する圧縮性・粘性解析を行う．対象として，単一気泡および気泡間相互干渉を含む二気泡の崩壊を議論する．気泡崩壊では液滴衝突と異なり大幅な気相体積変化が数値的な界面鈍りを助長するため，界面捕獲の移流方程式にこれを修正するソース項を導入する．単一気泡崩壊の結果から，気泡壁面間距離の増加に伴ってマイクロジェットは増速するが，壁面せん断応力はべき乗則に従って減衰することを確認した．壁面に対して水平に位置する二気泡崩壊の結果では，気泡間相互干渉によってマイクロジェットの衝突角が他方の気泡方向へ傾斜する作用が観察され，その結果として壁面せん断応力の上昇は約 1/10 以下に著しく抑制されることを確認した．

Abstract

Spurred by the demand for cleaning techniques of low environmental impact, one favors physical cleaning that does not rely on any chemicals (e.g., liquid jet cleaning and ultrasonic cleaning). In the present work, the cavitation accompanied by droplet impact and wall shear flow generated by droplet impact and cavitation bubble collapse near a rigid wall are simulated to understand their roles for surface erosion and cleaning contributions. Problems are modeled by solving compressible multicomponent Navier–Stokes (or Euler) equations and we solve a high-order accurate finite volume method that can capture both shocks and material interface.

Cavitation accompanied by high-speed droplet impact against a deformable wall is simulated to see whether the collapse is violent enough to occur surface erosion. The evolution of pressure waves in a single droplet to collide with a deformable wall at speed up to 110 m/s is simulated and the preexisting bubble nuclei (micron or submicron in radii) show large growth to submilimeters based on a one-way coupling evaluation. It is also found, the radiated pressure from the cavitation bubble collapse can overwhelm the water-hammer pressure directly created by the impact.

Radially spreading wall shear flow generated by high-speed droplet impact is believed to achieve particle removal in liquid jet cleaning, but its mechanism is not well understood. We simulate high-speed droplet impact on a dry/wet rigid wall to investigate wall shear flow as well as water hammer after the impact. The impact of a spherical water droplet (200 μm in diameter) at velocity from 30 to 50 m/s against a dry/wet rigid wall are considered. In the dry wall case, the strong wall shear appears near the moving contact line at the wetted surface. Once the wall is covered with the liquid film, the wall shear stress gets weaker as the film thickness increases; the similar trend holds for the water-hammer shock loading at the wall. Thereafter, we compute hydrodynamic force acting on small adherent particles in a one-way-coupling manner. The hydrodynamic force is estimated under Stokes' assumption and compared to particle adhesion of van der Waals type, enabling us to derive a simple criterion of the particle removal.

Collapse of cavitation bubbles near a rigid wall leads to the formation of a high-speed reentrant microjet toward the surface which plays an important role in ultrasonic cleaning. The jet impact accompanies radially spreading wall shear flow capable of removing contaminants from the surface, but the particle removal mechanism is not well understood due to the experimental challenges. We simulate the so-called Rayleigh bubble collapse (100 μm in radius) near a no-slip, rigid wall to quantify the wall shear flow. Collapse of both single bubble and two bubbles are considered and the driving pressure ranges from 2

to 10 MPa. Our simulations show that generation of wall shear flow particularly after the jet impact. Lastly, the suppression effects on the wall shear stress due to the bubble-bubble interaction is clarified.

Acknowledgements

First and foremost, I would like to express my heartfeldt gratitude to my advisor, Prof. Keita Ando for his patient and enthusiastic guidance throughout the thesis project. Since I joined the laboratory, he was always supportive and gave me instructive advices which was essential for my growth and also my future career. I am very grateful for his generosity that respects my interests and opinions. Again, I do appreciate his considerate mentorship over the past six years. I also thank my committee members, Prof. Akiko Matsuo, Prof. Koji Fukagata and Prof. Satoko Fujioka for their time and valuable advices towards my thesis.

I acknowledge Prof. Tim Colonius, Prof. Kazuki Maeda and Dr. Jomela Meng for their meticulous suggestions and advices during my three-month visit at California Institute of Technology in 2015. I also express my glatitude to Prof. Eric Johnsen, Dr. Shahaboddin Alahyari Beig, Dr. Mauro Rodriguez, Kazuya Murakami and Minki Kim for their kindness and very constructive discussions during my eight-month visit at University of Michigan in 2017. Prof. Johnsen warmly welcomed me in his group and gave valuable comments and suggestions every week. I also particularly appreciate Shahab and Mauro for their time to discuss about state-of-the-art numerical schemes and to help my simulations on supercomputers. This collaborative research was especially precious for my study.

I appreciate weekly joint seminar with Prof. Shinnosuke Obi, Prof. Koji Fukagata and graduate students in their groups. Their constructive suggestions and comments were instructive and made great contributions to my study. It also helped me improve my academic presentation. I also appreciate Prof. Yoshiyuki Tagawa for having annual joint seminar and inter-laboratory collaborations. I am also grateful to Prof. Toshiyuki Sanada for his advices about studies of the droplet impact and the physical cleaning.

I truly wish to thank the past and present colleagues in Ando laboratory, Tatsuya Yamashita, Tatsuya Kobayashi, Takehiro Nakajima, Ryota Oguri, Masashi Sasaki, Eriko Shirota, Sosuke Fukui, Nobuyuki Nakamura, Risa Yamauchi, Kentaro Asano, Taisuke Sato, Yushi Yamakawa, Yoichiro Fukuchi, Atsuhide Inatomi, Yu Katano, Hiroki Kurahara and Ikumi Takemura for their warm encouragement and cooperation. Especially, I do appreciate Tatsuya Yamashita for wide-ranging discussions over the past six years. I am indebted for Tatsuya's in-depth insights into bubble dynamics as an experimentalist. I was very happy to spent time together in the laboratory.

Last but not least, I would like to thank my family, who were always extraordinarily supportive all the time.

This work was supported in part by MEXT Grant-in-Aid for the Program for Leading Graduate Schools and JSPS KAKENHI Grant Number JP17J02211.

List of publication

(1) Articles on periodicals (related to thesis)

1. T. Kondo, S. A. Beig, E. Johnsen and K. Ando, "Simulation of shear flow generated by collapsing bubbles near a rigid wall," *In preparation*.

2. T. Kondo and K. Ando, "Simulation of high-speed droplet impact against a dry/wet rigid wall for understanding the mechanism of liquid jet cleaning," *Phys. Fluids*, vol. 31, 013303, 2019.

3. T. Kondo and K. Ando, "One-way-coupling simulation of cavitation accompanied by high-speed droplet impact," *Phys. Fluids*, vol. 28, 033303, 2016.

(2) Articles on international conference proceedings (full-length articles)

1. T. Kondo and K. Ando, "Compressible Navier–Stokes Simulation of High-Speed Droplet Impact Against Rigid Walls", in Proc. of *3rd International Symposium on Multiscale Multiphase Process Engineering (MMPE2017)*, Toyama, Japan, May, 2017.

2. T. Kondo and K. Ando, "Numerical study of cavitation and water-hammer erosion caused by high-speed droplet impact", in Proc. of *The 13th Asian International Conference on Fluid Machinery (AICFM13)*, Tokyo, Japan, September, 2017.

3. T. Kondo and K. Ando, "Numerical simulation of cavitation accompanied by high-speed droplet impact", in Proc. of *2nd International Symposium on Multiscale Multiphase Process Engineering (MMPE2015)*, Hamburg, Germany, September, 2014.

Contents

List of Figures

List of Tables

Nomenclature

BC	Boundary condition
CFL	Courant–Friedrichs–Lewy
HLL	Harten–Lax–van Leer
HLLC	Harten–Lax–van Leer-Contact
JKR	Johnson–Kendall–Roberts
NASG	Noble-Able Stiffened gas
PRE	Particle Removal Efficiency
PSL	Polystylene latex
RCA	Radio Corporation of America
VOF	Volume of fluid
WENO	Weighted Essentially Non-Oscillatory

Chapter 1

Introduction

1.1 Motivation

Particulate contamination is one of the major issues in semiconductor manufacturing because it is directly related to yielding loss. The target contamination is becoming smaller (sub-micron or even smaller) as the semiconductor devices become further miniaturized (Li *et al.*, 1997). In this context, the central research topic is to develop a cleaning strategy that is highly efficient enough for ultra-precision manufacturing. Hereafter, cleaning is formally defined as removal of contaminant particles from material surfaces.

Historically, the popular cleaning method in industry is known as chemical immersion cleaning method. For instance, the Radio Corporation of America (RCA) cleaning method, one of the most popular immersion techniques, is composed of seven stages (Kern, 1990). Every stage requires immersion in solutions such as sulfuric acid, hydrogen peroxide, and hydrogen fluoride. Thereby, this classical type of static chemical immersion cleaning is time-consuming and its environmental impact is controversial. To deal with these issues, physical forces are incorporated in major recent cleaning processes to facilitate the particle removal efficiency (PRE) (Busnaina *et al.*, 2002; Okorn-Schmidt *et al.*, 2013).

In physical cleaning based on hydrodynamic force, interaction between wall shear flow and adhered particles is believed to play an essential role (Henry & Minier, 2014).

Particle removal under simple shear flow of liquid or gas has previously been studied experimentally and analytically (Fan *et al.*, 1997; Busnaina *et al.*, 2002; Burdick *et al.*, 2005; Zoeteweij *et al.*, 2009). The mechanism of the particle removal can be classified into *rolling, sliding*, and *lifting* (to be recalled in Chapter 3). These previous studies suggest that the rolling mechanism arising from the torque induced by the hydrodynamic drag plays a dominant role in the particle removal and the rotatory motion of particles are also visualized by an image processing (Agudo *et al.*, 2017*b*). In this sense, when it comes to facilitating the cleaning efficiency, it is essential to generate steep velocity gradients around attached particles. One of the promising methods is based on water jets that often involve fission into droplet fragments and collide with target surfaces (Watanabe *et al.*, 2009; Erkan & Okamoto, 2014; Frommhold *et al.*, 2015). The jet-based cleaning method has already become popular in precision processing and its performance improvement is one of the overarching goals. Furthermore, ultrasonic cleaning that uses the dynamics of acoustic cavitation bubbles in liquid batch is also known as high-efficient physical cleaning method (Gale & Busnaina, 1999; Kohli & Mittal, 2011; Yamashita *et al.*, 2018). As a particularly practical importance of ultrasonic cleaning, it is suitable for combination with chemical immersion.

In order to improve these types of physical cleaning, it is therefore imperative to fully understand two canonical multicomponent flow phenomena: high-speed droplet impact and bubble collapse. In what follows, these issues are addressed in further details.

1.2 Historical perspectives

1.2.1 High-speed droplet impact

High-speed droplet impact onto solid surfaces is relevant to a number of applications in industry. One of the classical examples is aircrafts whose wings are exposed to raindrop impact under their operation and eventually suffer from erosion due to the water-hammer

loading (Cook, 1928; Huang *et al.*, 1973). More recently, such erosion becomes a technical issue in ink-jet printing and physical cleaning based on liquid jets (Okorn-Schmidt *et al.*, 2013; Sanada *et al.*, 2008; Sanada & Watanabe, 2015; Tatekura *et al.*, 2015). One of the earliest theoretical studies is Heymann's work that considers one-dimensional droplet impact at high speed where liquid compressibility comes into play (Heymann, 1969). Extensions to the cases of deformable surfaces (Brunton & Rochester, 1979) and spherical droplets (Engel, 1955) were performed in the subsequent studies. Moreover, the impact of water droplets against solid walls has been studied experimentally in wide parameter space; the impact velocity ranges from 10^{-1} m/s to 10^{2} m/s and the droplet diameter varies between 10^{-5} m and 10^{-2} m (Visser *et al.*, 2015). In these studies, both acoustic and fluid-dynamic phenomena of the droplet impact have been widely studied (e.g., water hammer (Heymann, 1969; Dear & Field, 1988; Kennedy & Field, 2000; Haller *et al.*, 2002; Sasaki *et al.*, 2016), cavitation (Field *et al.*, 1989; Obreschkow *et al.*, 2011), splashing (Yarin & Weiss, 1995; Wal *et al.*, 2006; Thoroddsen *et al.*, 2011; Guo & Lian, 2017; Banitabaei & Amirfazli, 2017; Boelens & de Pablo, 2018; Charalampous & Hardalupas, 2017), side jetting (Lesser, 1981; Weiss & Yarin, 1999; Haller *et al.*, 2002) and rim instability (Regulagadda *et al.*, 2017; Huang *et al.*, 2018)).

It is interesting to note that recent studies suggest the potential role of cavitation within the impinging droplet in the issue of surface erosion (Field *et al.*, 2012; Obreschkow *et al.*, 2011). Experimentally, cavitation accompanied by high-speed droplet impact was observed by Brunton & Camus (1970) and Field *et al.* (1989). The cavitation can be explained by acoustic impedance mismatch at droplet interfaces. When a water-hammer shock wave (arising from the impact) reflects at the distal interface of the droplet, the resulting tension wave can rupture the droplet, nucleating cavitation bubbles as illustrated by Obreschkow *et al.* (2011). Haller *et al.* (2002, 2003) simulated the impingement of compressible droplets against a rigid wall. Their simulation supports the formation of

such a tension wave within the droplet. Nevertheless, the contribution of such cavitation (and its collapse often followed by strong shock emission) to the erosion is not yet clarified.

Though the high-speed droplet impact has remained a central research topic over the past decades, further knowledge of its dynamics is still demanded in context of the physical cleaning. To optimize the PRE of the jet-based cleaning, one can use monodisperse splay of micron-sized droplet train (Brenn *et al.*, 1997; Kim *et al.*, 2003; Sato *et al.*, 2011; Okorn-Schmidt *et al.*, 2013; Visser *et al.*, 2015). To evaluate the PRE quantitatively, previous researchers usually compared the number of contaminant particles between pre- and post-cleaned silicon wafers (Sato *et al.*, 2011; Fernando *et al.*, 2011; Okorn-Schmidt *et al.*, 2013). However, this evaluation is insufficient to identify the mechanism of the particle removal and it is challenging to experimentally evaluate the wall shear flow development and particle removal. In this context, numerical approach will be an important tool to quantify the near-wall flow profiles and the shear-induced particle removal. There are some numerical studies about shear-induced particle removal in incompressible laminar flow (Agudo *et al.*, 2017*a*), incompressible turbulent flow (Chen *et al.*, 2018), compressible air jet (Song *et al.*, 2014) and bubble collapse near a wall (Chahine *et al.*, 2016). However, to our knowledge, wall shear flow formation during the droplet impact has not yet been simulated. Furthermore, to promote the efficiency of liquid jet cleaning, higher impact velocity is favored but may give rise to erosion of the cleaning surface due to water-hammer shock loading from the impact. Hence, to understand cleaning contributions and erosion effects of high-speed droplet impact, both viscosity and compressibility of the fluids need to be accounted for.

1.2.2 Bubble collapse

Cavitation bubble collapse near solid boundaries is paid primal attention in a wide variety of applications because it may give rise to surface erosion. Such erosive effect is caused by the formation of a high-speed, reentrant microjet directed toward the wall surface during the bubble collapse phase (Plesset & Chapman, 1971; Lauterborn & Bolle, 1975; Shima & Tomita, 1981; Supponen *et al.*, 2017). In hydraulic applications, many researchers have long studied bubble collapse in the context of cavitation erosion (Knapp, 1955; Arndt, 1981). More recently, the dynamics of acoustic cavitation bubbles have been of benefit in biomedicine (Brujan, 2011; Brennen, 2015), sonochemistry (Crum, 1994) and physical cleaning (Chahine *et al.*, 2016; Yamashita *et al.*, 2018).

In the context of physical cleaning, the microjet impingement during the bubble collapse is an intriguing phenomenon because it may cause strong wall shear flow as seen in high-speed liquid jet cleaning (Watanabe *et al.*, 2009; Erkan & Okamoto, 2014; Frommhold *et al.*, 2015). However, due to the experimental challenge to resolve the bubble dynamics and the resulting fluid flow, the cleaning mechanism is not well understood. We thus take a numerical approach for the quantitative investigations. In what follows, detailed literature survey is provided for both experimental and numerical studies about the near-wall bubble collapse.

To experimentally investigate the bubble collapse near a wall, researchers mainly study its dynamics from a laser-induced cavitation bubble because it can highly control the position of cavitation inception by changing the focus location of a laser (Vogel & Lauterborn, 1988; Philipp & Lauterborn, 1998; Brujan *et al.*, 2002). For understanding the surface erosion by the near-wall bubble collapse, impulsive pressure rise during the collapse is measured by Tomita & Shima (1986). To quantify the characteristics of the microjet velocity, a unified scaling law is proposed by Supponen *et al.* (2016) and that can examine the velocity of the microjet only by the stand-off distance from the wall to

the bubble center without regard to various nonspherical collapse drivers (e.g., presence of the rigid surface, free surface, or pressure gradient). The near-wall fluid flow induced by the bubble collapse is visualized by Reuter *et al.* (2017*a*). Here, we note that bubble dynamics in underwater ultrasound is also studied from a laser-induced cavitation bubble for simplicity because it is challenging to control acoustic cavitation spatially and temporally. In this context, the accompanying wall shear flow formation and its surface cleaning effect have been reported by few researchers. Ohl *et al.* (2006*a*) investigate the transition of wall-attached fluorescent particles during the collapse of a near-wall, laser-induced cavitation bubble to visualize the contribution of cavitation-induced wall shear flow to the cleaning. Thereafter, Dijkink & Ohl (2008) measure the wall shear stress at several spots, which arises from the laser-induced cavitation bubble, by means of a constant temperature anemometer. The other experiment of wall shear stress from cavitation bubble is carried out based on electrochemical microscopy by Reuter & Mettin (2018) and its result is fairly reasonable in comparison to the former experiment (Dijkink & Ohl, 2008). We note that both the above experiments only focus on the case of single bubble collapse while the cavitation is often occurred as a cluster near the target surface in ultrasonic cleaning. On the other hand, Kim & Kim (2014) visualize disruptive bubble collapse near a wall in ultrasonic field for understanding the surface damage in ultrasonic cleaning. Yamashita & Ando (2019 in press) investigate the ultrasound-induced reentrant microjet formation of a trapped bubble on a glass surface in oxygen-supersaturated water. This work also qualitatively reports the effect of the bubble-bubble interaction in the collapse of a bubble pair attached to the wall.

When it comes to simulation studies, Johnsen & Colonius (2009) perform Euler flow simulation to quantify the jet velocity and pressure emission of bubbles collapsing near a wall. Compressible Navier–Stokes simulation of bubble collapse near a wall that is designed by solution-adaptive, high-resolution scheme is performed by Beig & Johnsen

(2015). Thereby, the detailed characteristics of the jet velocity, pressure and temperature is quantified but near-wall flow profiles are beyond their scope (Beig, 2018; Beig *et al.*, 2018). Their works also include the investigation of dynamics of a bubble pair in terms of microjet morphology. To understand the wall shear flow formation, Zeng *et al.* (2018) numerically reproduce the experiment of Dijkink & Ohl (2008) by compressible Navier–Stokes simulation based on a volume of fluid (VOF) method. However, the simulated wall shear stress disagrees with the corresponding experiment. The difficulty is mainly related to the treatment of the computational grid that can sufficiently resolve the physical viscosity. Since the viscous effects is only dominating in the vicinity of the wall in the bubble collapse simulation, fine grid spacing is only required locally near the wall. However, it tighten the Coulant–Friedrichs–Levi (CFL) condition and the simulation becomes crucially time-consuming. Therefore, obtaining the correspondence between the experimental and numerical works are still challenging. In context of the simulation of the multiple-bubble dynamics, Tiwari *et al.* (2015) investigate the nonspherical collapses of respective bubbles in a near-wall bubble cluster but viscosity is neglected. On the other hand, the near-wall bubble collapse under ultrasound irradiation is simulated by Boyd & Becker (2018); Ma *et al.* (2018); Qiu *et al.* (2018) and the reentrant microjet formation is reproduced like a laser-induced cavitation. Ochiai & Ishimoto (2017) numerically investigate the multiple-bubble oscillations for megasonic cleaning applications to clarify the effects of bubble-bubble interactions in the bubble morphology and the wall pressure evolution. However, wall shear flow formation is beyond their scope and the spatial resolution is insufficient to resolve the near-wall viscous effect. Hence, to understand the cleaning mechanism, there is a need for further numerical investigations of the near-wall collapse of both the single and a pair of bubbles, which can sufficiently resolve the compressible viscous flow.

1.3 Objectives and contributions

Accordingly, to provide a more concrete insight for the improvement of physical cleaning, numerical investigations of high-speed droplet impact and bubble collapse near a wall are conducted. The main objective of this work is to understand compressible and viscous flow physics of these phenomena by direct numerical simulation in terms of the surface erosion by water hammer and the cleaning effect coming from the wall shear flow. Moreover, coupled problems (e.g., cavitation during the droplet impact and particle removal in wall shear flow) are of great concern.

The main contributions of this thesis are summarized as follows:

- Correspondence between the current simulation and the previous experiment by Field *et al.* (1989) is obtained for cylindrical droplet impact and the cavitation occurrence within the droplet.

- Cavitation threshold pressure is suggested under the specific cases of the droplet impact.

- In Navier–Stokes flow simulation, droplet impingement against a dry wall, which involves stress singularities on the moving contact line, is robustly reproduced by implementing a partial velocity slip condition based on molecular dynamics.

- Wall shear stress generated by the droplet impact is characterized as a function of the water film thickness covering the rigid wall initially.

- Nondimensional parameter for judging the possibility of particle removal is proposed as a function of wall shear stress, which evaluates the torque balances between adherent force of van der Waals type and hydrodynamic surface torques from the wall shear flow.

- Wall shear stress generated by the cavitation bubble collapse is characterized as a function of the stand-off distance from the bubble center to the wall in the case of single bubble.

- As an effect of bubble-bubble interaction, remarkable decaying of wall shear stress is observed in the cases of two-bubbles collapse and the effect of the length of the inter-bubble distance is evaluated.

1.4 Organization of this thesis

This thesis is organized as follows. In Chapter 2, cavitation accompanied by high-speed droplet impact is numerically investigated to clarify its role in surface erosion. Two-dimensional Euler flow simulation of the thin cylindrical gelatin droplet impact is first implemented to reproduce the previous experiment. The cavitation within the droplet is reproduced by solving the equation of Rayleigh–Plesset type in one-way coupling manner. Chapter 3 presents impingement of the spherical droplet is simulated for understanding the mechanism of liquid jet cleaning. Axisymmetric two-dimensional Navier–Stokes flow simulation is implemented to investigate the water-hammer pressure and wall shear flow generated by the droplet impact. As a treatment of the (no-slip) rigid wall, both dry and wet condition is considered. Given the flow profiles near the wall, particle removal is evaluated from the nondimensional parameter for the particle removal judgement. Lastly, in Chapter 4, cavitation bubble collapse is simulated to investigate the resultant wall shear flow formation. Three-dimensional Navier–Stokes flow simulation is implemented to reproduce the collapse of single bubble and two bubbles. Noted that these Chapters 2 to 4 include the sections of physical/numerical modeling respectively because these three problems are simulated by different manners. Concluding remarks and suggestions for further study are stated in Chapter 5.

Chapter 2

Cavitation accompanied by high-speed droplet impact

2.1 Introduction and outline

In this chapter, we numerically investigate the possible role of the collapse of cavitation bubbles accompanied by high-speed droplet impact as a source of erosion. For simplicity, we study the cavitation bubble dynamics in a one-way-coupling manner; the evolution of pressure waves within the droplet to collide with a moving wall is obtained from multicomponent Euler flow simulation and is then substituted to a Rayleigh–Plesset-type equation to compute the dynamics of cavitation arising from small bubble nuclei that are supposed to exist inside the droplet. Particularly, we aim to see how large pressure radiation from the cavitation bubble collapse is in comparison to the initial water-hammer loading.

2.2 Physical modeling

2.2.1 Problem description

As a representative example, we numerically reproduce the experiment of Field *et al.* (1989). In their experiment, a cylindrical, two-dimensional 12 wt% gelatin droplet fixed between transparent plates whose separation is 3 mm (much larger than cavitation bubbles

nucleated in between) is set into collision with a solid material moving at speed V_i = 110 m/s (see Fig. 2.1). Their claim is that the gelatin viscoelasticity does not play a role in acoustic wave propagation inside the droplet. The diameter of the cylindrical droplet is 10 mm so that the Laplace pressure within the droplet is very small compared to the water-hammer pressure. The subsequent splash formation (where surface tention comes into play) is beyond our scope. Even though air entrapment between impinging droplets and a wall is reported for impact velocity up to O(10 m/s) (van Dam & Le Clerc, 2004; Li & Thoroddsen, 2015; Li *et al.*, 2015), it is ignored in our simulation with impact velocity of 110 m/s. Moreover, to be simple, we treat a deformable wall as a stiff fluid whose acoustic impedance is defined as the product of density and (longitudinal) speed of sound in the solid (Thompson, 1972; Sanada *et al.*, 2011).

After the impingement, the water-hammer shock wave reflects at the droplet interface as a tension wave due to acoustic impedance mismatch between the droplet and the ambient air. Here, we explore the possibility of cavitation inception from micron/submicron-sized gas bubble nuclei. Micron-sized gas bubbles exist naturally in tap water (O'Hern *et al.*, 1988; Mørch, 2015), so that the simulation will represent heterogeneous cavitation. On the other hand, unless contaminant gas bubbles are present in liquids, cavitation is expected to occur homogeneously from submicron-sized voids that randomly appear among thermally fluctuating liquid molecules (Herbert *et al.*, 2006; Caupin & Herbert, 2006). To numerically replicate homogeneous-like cavitation, we run Rayleigh–Plesset-type calculations, starting from submicron-sized bubble nuclei, based on continuum assumptions (Maxwell *et al.*, 2013; Tsuda *et al.*, 2015). For simplicity, the volume fraction of nuclei and the subsequent cavitation bubbles is assumed to be so low that the pressure field inside the droplet is not contaminated by the bubble dynamics; the bubble dynamics are then determined according to the pressure evolution (i.e., one-way coupling).

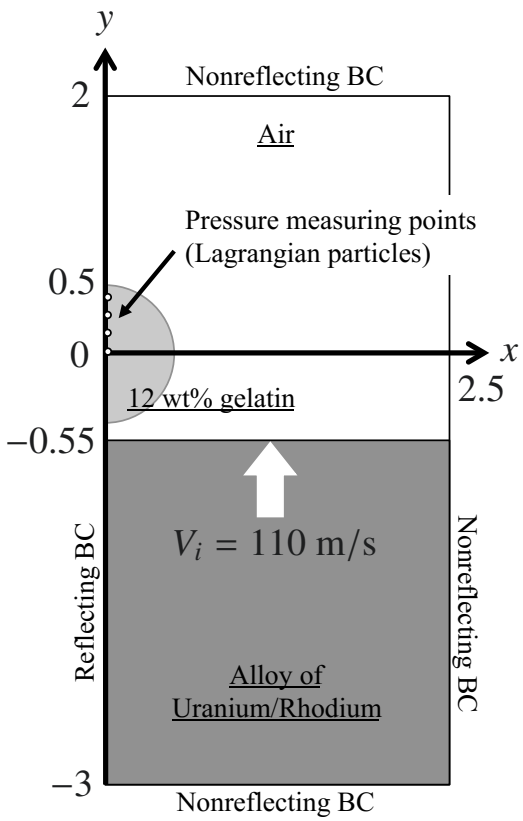

Fig. 2.1: Computational setup of a cylindrical droplet and a deformable wall moving at V_i (at time $t = 0$). Because the problem is symmetric about the y axis, the flow is simulated for $x \geq 0$ only, imposing the reflecting boundary condition (BC) along the y axis. Length scale is normalized by the droplet diameter.

2.2.2 Governing equations for the multi-component fluid flow

Accordingly, to capture the acoustic wave interaction in the high-speed droplet impact against a deformable wall, we solve multicomponent Euler equations modeled by five-equation formulation (Allaire *et al.*, 2002; Perigaud & Saurel, 2005). Even though interfaces separating the three components are physically discontinuous in the sense of continuum mechanics, interface smearing is introduced in the simulation. Conceptually speaking, the mixture of the two neighbor components appears in numerically diffused interfaces. Here, mass conservation (Eqs. (2.1-a), (2.1-b) and (2.1-c)) is treated for gas, liquid and solid components separately, while momentum and energy conservation (Eqs.

(2.1-d), (2.1-e) and (2.1-f)) are formulated for the mixture. The numerically diffused interfaces are represented by volume fraction and advected by Eq. (2.1-g) and (2.1-h).

$$\frac{\partial}{\partial t}\begin{pmatrix} \alpha_G\rho_G \\ \alpha_L\rho_L \\ \alpha_S\rho_S \\ \rho u \\ \rho v \\ E \\ \alpha_G \\ \alpha_L \end{pmatrix} + \frac{\partial}{\partial x}\begin{pmatrix} \alpha_G\rho_G u \\ \alpha_L\rho_L u \\ \alpha_S\rho_S u \\ \rho u^2 + p \\ \rho uv \\ u(E+p) \\ \alpha_G u \\ \alpha_L u \end{pmatrix} + \frac{\partial}{\partial y}\begin{pmatrix} \alpha_G\rho_G v \\ \alpha_L\rho_L v \\ \alpha_S\rho_S v \\ \rho uv \\ \rho v^2 + p \\ v(E+p) \\ \alpha_G v \\ \alpha_L v \end{pmatrix} = \begin{pmatrix} 0 \\ 0 \\ 0 \\ 0 \\ 0 \\ 0 \\ \alpha_G\nabla\cdot\mathbf{u} \\ \alpha_L\nabla\cdot\mathbf{u} \end{pmatrix}. \quad \begin{matrix} \text{(a)} \\ \text{(b)} \\ \text{(c)} \\ \text{(d)} \\ \text{(e)} \\ \text{(f)} \\ \text{(g)} \\ \text{(h)} \end{matrix} \tag{2.1}$$

Here, α_m is the volume fraction of component m where m = G, L and S stand, respectively, for the gas phase (air), liquid phase (gelatin) and solid phase (alloy), ρ_m is the density of component m, ρ is the mixture density (to be defined by Eq. (2.4)), u and v are velocities, respectively, in x and y coordinates, p is thermodynamic pressure, E is total energy (per unit volume), and $\nabla\cdot\boldsymbol{u}$ is the divergence of the velocity vector field $((\partial u/\partial x) + (\partial v/\partial y))$. Surface tension is neglected since capillary effects are expected to be less important in comparison to inertial effects in high-speed droplet impact Meng & Colonius (2015).

The system of Eq. (2.1) is closed by the stiffened gas equation of state:

$$\frac{p}{\gamma-1} + \frac{\gamma P_\infty}{\gamma-1} = E - \frac{1}{2}\rho\left(u^2+v^2\right), \tag{2.2}$$

where γ and P_∞ are thermodynamic constants for the mixture; the value of γ controls the material compressibility and P_∞ corresponds to the tensile strength of liquids or solids due to inter-molecular cohesive force. Equation (2.2) can model perfect gases by setting $\gamma = 1.4$ (the ratio of specific heats for air) and $P_\infty = 0$ (no cohesion between the gas molecules). In the five-equation model, we need to introduce the following mixture rule to define quantities in the mixture:

$$\alpha_G + \alpha_L + \alpha_S = 1, \tag{2.3}$$

$$\phi = \alpha_G\phi_G + \alpha_L\phi_L + \alpha_S\phi_S, \tag{2.4}$$

$$\boldsymbol{\phi} = \begin{pmatrix} \rho & \gamma & P_\infty \end{pmatrix}^{\mathrm{T}}, \tag{2.5}$$

$$\boldsymbol{\phi}_m = \begin{pmatrix} \rho_m & \gamma_m & P_{\infty,m} \end{pmatrix}^{\mathrm{T}}, \tag{2.6}$$

where $\boldsymbol{\phi}$ is a vector composed of respective mixture physical properties in Eq. (2.1) to (2.2) and $\boldsymbol{\phi}_m$ is a vector composed of respective physical properties of water (m = L), air (m = G) and an alloy (m = S). Table 2.1 summarizes the values of γ and P_∞ as well as other thermodynamic properties for materials of our concern (at standard temperature and pressure) (Gojani *et al.*, 2009; Coralic & Colonius, 2014; Saurel & Abgrall, 1999).

To record the pressure evolution within the droplet, Lagrangian fluid particles are initially set along the y-axis and labeled as $\boldsymbol{Y}_\epsilon$. This fluid particle position may represent that of a preexisting gas-bubble nucleus whose size is assumed to be small enough to ignore slip with respect to its surrounding flow. The no-slip assumption will be more reasonable for gelatin gel droplets (as in Field *et al.* (1989); Shirota & Ando (2015)) whose elasticity is expected to hinder the slip of bubble nuclei relative to the surrounding material. We set the particles at the droplet center ($\epsilon = 0$) and with the eccentricity (normalized by the droplet diameter) from the droplet center selected at 0.1, 0.2, 0.25, and 0.3. During the Euler flow simulation, the particle is traced according to the flow and the pressure it experiences is interpolated and recorded. The recorded pressure is used to determine the dynamics of a cavitation bubble to be nucleated at $\boldsymbol{Y}_\epsilon$ as explained in the Section 2.2.3.

2.2.3 Governing equation for the single bubble dynamics

The dynamics of a spherical cavitation bubble nucleated at $\boldsymbol{Y}_\epsilon$ are determined by the Gilmore equation (Gilmore, 1952), an extended Rayleigh–Plesset equation that takes liquid compressibility into account:

$$R\ddot{R}\left(1-\frac{\dot{R}}{C}\right)+\frac{3}{2}\dot{R}^2\left(1-\frac{\dot{R}}{3C}\right)=H\left(1+\frac{\dot{R}}{C}\right)+\frac{R\dot{H}}{C}\left(1-\frac{\dot{R}}{C}\right). \tag{2.7}$$

Table 2.1: Thermodynamic properties of air (ambient), water, 12 wt% gelatin (Gojani *et al.*, 2009; Coralic & Colonius, 2014) (droplet), and Uranium/Rhodium alloy (Saurel & Abgrall, 1999) (wall). Acoustic impedance is normalized by the value of water.

	Air (m = G)	Water (for reference)	12 wt% gelatin (m = L)	Alloy (m = S)
Density ρ_m [kg/m^3]	1.2	1000	1030	17200
Sonic speed c_m [m/s]	343	1450	1550	2740
Specific acoustic impedance [–]	2.84×10^{-4}	1.00	1.10	32.5
γ_m [–]	1.40	6.12	6.72	3.53
$P_{\infty,m}$ [GPa]	0	0.343	0.370	36.6

The dot denotes time derivative, R is the bubble radius, and C and H are the sonic speed and the enthalpy of the droplet, respectively, at the bubble wall:

$$C = \sqrt{\frac{\gamma(p_0 + P_\infty)}{\rho_{\mathrm{L}0}}\left(\frac{p_\mathrm{L} + P_\infty}{p_0 + P_\infty}\right)^{\frac{\gamma-1}{\gamma}} + (\gamma - 1)H}, \tag{2.8}$$

$$H = \frac{\gamma}{\gamma - 1}\frac{p_0 + P_\infty}{\rho_{\mathrm{L}0}}\left[\left(\frac{p_\mathrm{bw} + P_\infty}{p_0 + P_\infty}\right)^{\frac{\gamma-1}{\gamma}} - \left(\frac{p_\mathrm{L} + P_\infty}{p_0 + P_\infty}\right)^{\frac{\gamma-1}{\gamma}}\right]. \tag{2.9}$$

Subscripts L and 0 mean quantities attributed to the liquid phase (droplet) and values at the equilibrium state (one atmosphere), respectively. The (far-field) liquid pressure, p_L, is given by the pressure recorded at $\boldsymbol{Y}_\epsilon$ in the Euler flow simulation (see Section 2.2.2), and the bubble wall pressure (at the droplet side), p_bw, is described by

$$p_\mathrm{bw} = p_\mathrm{G} + p_\mathrm{v} - \frac{4\mu\dot{R}}{R} - \frac{2S}{R}, \tag{2.10}$$

where p_G is the partial pressure of gas contents inside the bubble, p_v is the saturated vapor pressure (2.3 kPa at the undisturbed liquid temperature 20°C due to the cold liquid assumption (Preston *et al.*, 2007; Prosperetti *et al.*, 1988)), and S is the surface tension. In this case, the gas pressure may be modeled by

$$p_\mathrm{G} = \left(p_0 - p_\mathrm{v} + \frac{2S}{R_0}\right)\left(\frac{R_0}{R}\right)^{3\kappa}, \tag{2.11}$$

where R_0 is the (equilibrium) radius of a gas bubble nucleus that is assumed to exist at $\mathbf{Y}_\epsilon$ and κ is a polytropic index; $\kappa = 1$ models isothermal gas behavior and $\kappa = \gamma$ corresponds to adiabatic behavior. For nonlinear bubble oscillations, we often rely on more sophisticated models of heat and mass transfer at the bubble wall (see for example Preston *et al.* (2007); Stricker *et al.* (2011); Warnez & Johnsen (2015)). In addition to the case of polytropic bubbles represented by Eq. (2.11), we consider dissipative effects of heat transfer inside the bubble and phase changes at the bubble wall based on the reduced-order model proposed by Preston *et al.* (2007). This model will be accurate for small bubbles whose Peclet numbers of heat and mass transfer are below or on the order of 10 (for details, see Preston *et al.* (2007)); the model constraint is almost satisfied in our problem setup.

If the distance h from the bubble center to the wall is much larger than the bubble size ($h(t) \gg R(t)$), the bubble can be considered as a point source so that the radiated pressure is approximated by

$$p_\mathrm{a} = \frac{\rho_\mathrm{L}}{h}\left(2R\dot{R}^2 + R^2\ddot{R}\right), \tag{2.12}$$

where $\dot{R}$ and $\ddot{R}$ are determined from integrating the Gilmore Eq. (2.7). The radiated acoustic pressure p_a is to be compared to the water-hammer pressure obtained from the droplet impact simulation explained in Section 2.2.2.

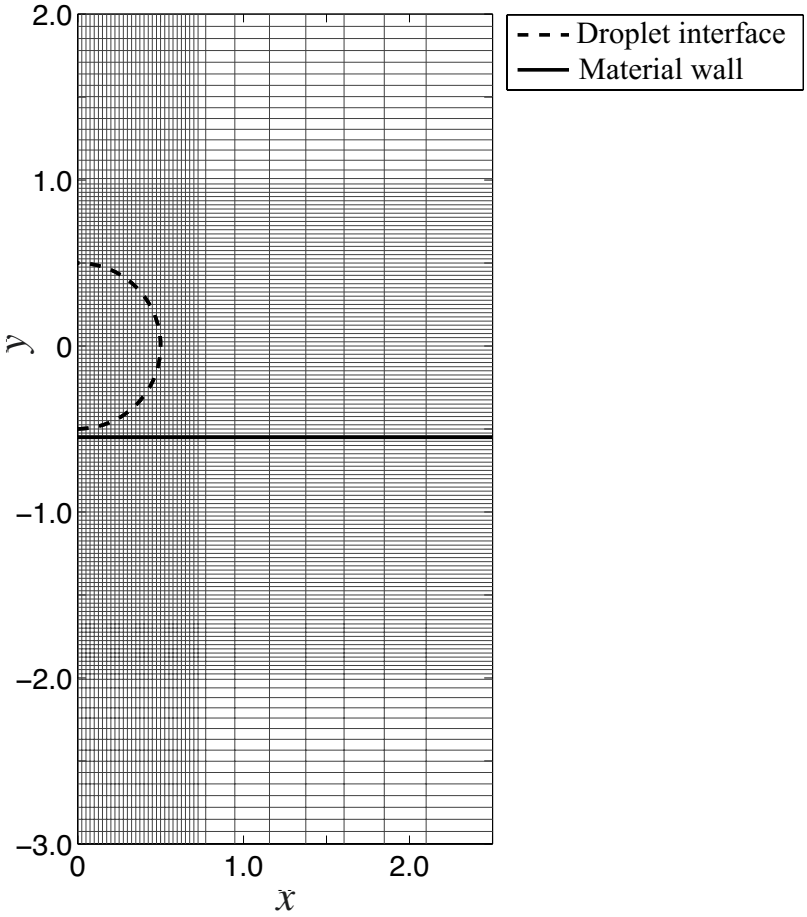

Fig. 2.2: Computational grid with the initial configuration of the droplet impact problem at $t = 0$. Gray line: computational grid (every 10 grid lines is presented). Blue and black lines: the nominal positions of numerically diffused material interfaces.

2.3 Numerical modeling

2.3.1 Spatial discretization and temporal integration of the Euler flow simulation

The numerical method we use is based on the shock-interface capturing scheme proposed by Johnsen & Colonius (2006) and Coralic & Colonius (2014), which allows us to stably simulate compressible flow involving both shocks and material interfaces. For spatial discretization, a third-order finite-volume weighted essentially nonoscillatory (WENO) scheme with the Harten–Lax–van Leer-Contact (HLLC) approximate Riemann solver

is adopted according to the previous droplet impact simulation by Meng & Colonius (2015). The component-wise WENO reconstruction is computed with primitive variables. The time integration is handled by a third-order total variation diminishing Runge–Kutta scheme (Gottlieb & Shu, 1998).

The numerical stability for the time integration is controlled by (dimensionless) Courant number C, which is the ratio of physical and numerical wave speeds:

$$C = \Delta t \max_{i,j} \left(\frac{c_{i,j} + |u_{i,j}|}{\Delta x_i}, \frac{c_{i,j} + |v_{i,j}|}{\Delta y_j} \right), \tag{2.13}$$

where the indicator i and j denote the numbers of computational cells in x and y direction, respectively. To stably capture the physical wave in simulations, it is necessary to satisfy the following Courant–Friedrichs–Lewy (CFL) condition:

$$0 < C \leq \frac{1}{N}, \tag{2.14}$$

where N stands for the number of spatial dimensions in the problem of concern. In this study, the time step is uniform with maximum Courant number set below 0.1.

The computational domain of the droplet impact is shown in Fig. 2.2. The grid is based on Cartesian coordinates. Since the flow is symmetric about the y axis, we solve the problem only for $x \geq 0$ by imposing the reflecting boundary conditions (Dadone & Grossman, 1994). While coarser grids are adopted away from the droplet in order to minimize spurious wave reflection together with nonreflecting boundary conditions (Thompson, 1987), finer grids (with 200 grid points used for the initial diameter of the droplet) are used to resolve the droplet. To avoid spurious oscillation at material interfaces, we use 8 grid points to diffuse interfaces in the initial configuration according to Johnsen & Colonius (2006). The nominal position of a numerically diffused interface is determined at $\alpha_{\mathrm{L}} = \alpha_{\mathrm{G}} = 0.5$ for the liquid/gas interface. We should note that air entrapment, which is reported experimentally in low-speed droplet impact (van Dam & Le Clerc, 2004; Li & Thoroddsen, 2015; Li *et al.*, 2015), cannot be observed because of the numerically diffused interfaces.

2.3.2 Temporal integration of the bubble dynamics simulation

Numerical integration of the Gilmore Eq. (2.7) is performed by ordinary differential equation (ODE) solver ODE15s, which is provided by MATLAB and designed for stiff systems, for stable and efficient calculations. As will be presented in Section 2.6, this method allows for resolving (numerically very stiff) violent collapse of cavitation bubbles.

2.4 One-dimentional droplet impact

Before discussing the impact of a cylindrical droplet against the solid wall (alloy), we reduce it to a one-dimensional problem. That is, we may numerically replicate the initial stage of the droplet impact as a one-dimensional water column collision with the wall. To be simple, the ambient air between the two materials is excluded from the simulation. The numerical method applied in this reduced problem is the same as in simulating the two-dimensional droplet impact with very fine grids with sufficiently small CFL number.

The impact speed of our concern is so high that nonlinearity would play a role in the acoustic wave propagation. In other words, it is inappropriate to use the celebrated water-hammer formula derived from linearized mass and momentum conservation laws. Heymann (1969) proposed the empirical formula to predict pressure generated from the high-speed impact:

$$p = \rho_{\mathrm{L}} c_{\mathrm{L}} V_{\mathrm{i}} \left(1 + a \frac{V_{\mathrm{i}}}{c_{\mathrm{L}}} \right), \tag{2.15}$$

where $\rho_{\mathrm{L}} c_{\mathrm{L}}$ is the acoustic impedance of the water (i.e., the product of density ρ_{L} and sonic speed c_{L}), V_{i} is the impact velocity, and a is a constant empirically determined at 2 for water. Note that Heymann's emprical formula reduces to the water-hammer formula by substituting $a = 0$. In Eq. (2.15), the solid is assumed to be rigid with infinite acoustic impedance, which may be reasonable from the large acoustic impedance of the alloy (see Table 2.1).

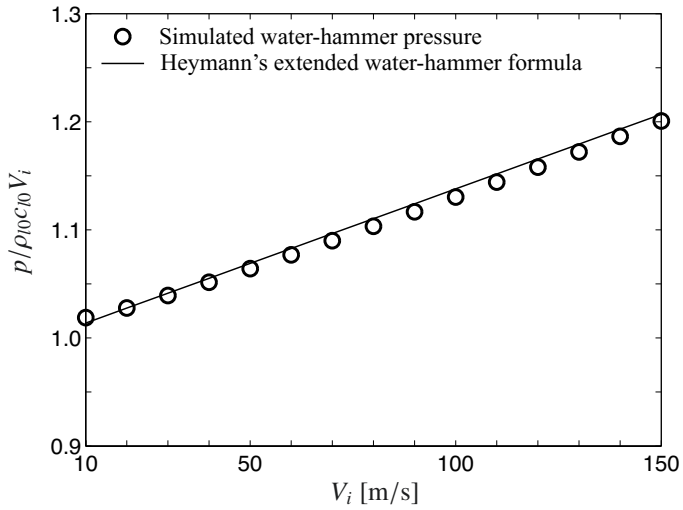

Fig. 2.3: Water-hammer pressures, simulated from the Euler flow simulation and predicted from Heymann's extended water-hammer Eq. (2.15), from one-dimensional impact of water and the solid wall (alloy) with varying the impact velocity V_i. The pressure p is normalized by $\rho_\mathrm{L} c_\mathrm{L} V_\mathrm{i}$.

In Fig. 2.3, the simulated pressure with varying V_i is compared to the empirical formula, Eq. (2.15). Here, the pressure is normalized by the (linear) water-hammer pressure $\rho_\mathrm{L} c_\mathrm{L} V_\mathrm{i}$, so that its deviation from unity represents nonlinear effects. It turns out that the simulation is well captured by the empirical formula. This simplified example suggests that nonlinear Euler flow simulations are essential to properly capture the dynamics of high-speed droplet impact.

2.5 High-speed cylindrical droplet impact

We numerically reproduce the cylindrical droplet (gelatin) impacted by the solid wall (alloy) moving at $V_\mathrm{i} = 110$ m/s. To see the evolution of acoustic waves arising from the impact, numerical Schlieren images at different times are presented, together with the experimental observation from Field *et al.* (1989) (see Fig. 2.4). It follows that important features reported in the experiment including water-hammer shock propagation and the focusing of the reflected wave from the droplet interface are well reproduced in the

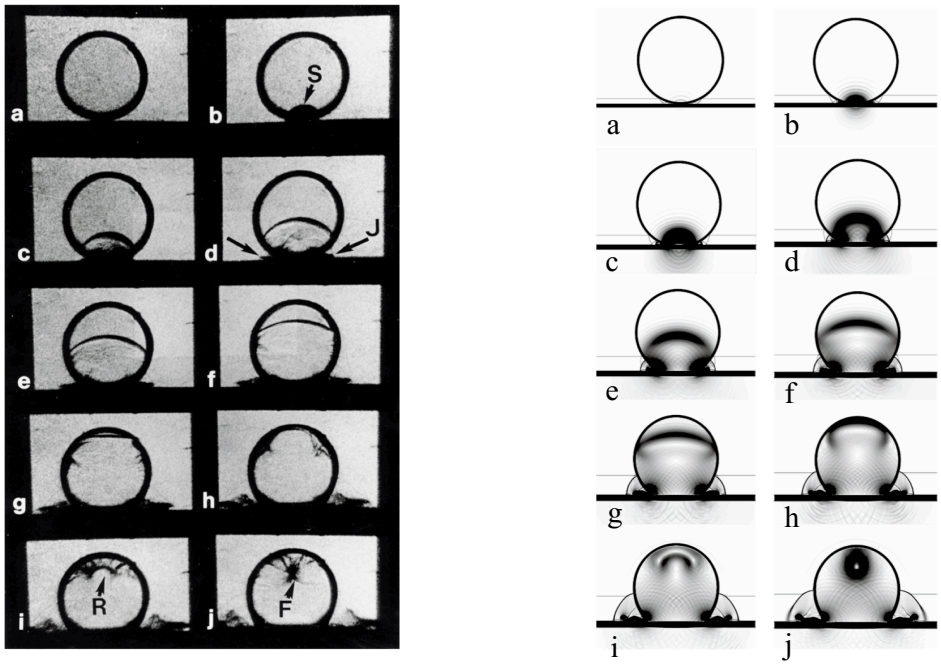

(a) (b)

Fig. 2.4: (a) High-speed cylindrical droplet impact in the experiment of Field *et al.* (1989). A 12 wt% gelatin droplet (10 mm in diameter) is impacted by a metal slider at V_i = 110 m/s. Labels S and J mean shock and jet formation. A reflected tension wave (labeled R) is focused (labeled F), rupturing the gelatin (i.e., cavitation). The interframe between snapshots is 1 μs. Reprinted with permission from J. E. Field *et al.*, "The effects of target compliance on liquid drop impact," *J. Appl. Phys.*, vol. 65, pp. 533–540. ©1989, AIP Publishing LLC. (b) Numerical Schlieren of the Euler flow simulation displayed at the same times as in (a).

simulation. The water-hammer shock propagates toward the distal side of the water-air interface of the droplet (frames a to h). Due to acoustic impedance mismatch, the shock is reflected as a tension wave (frame i), which is focused within the droplet (frame j). In the frame j of the experiment, it is reported that the gelatin was ruptured by the focused tension wave and a cloud of cavitation bubbles appeared in the focal spot.

To explain the cavitation observed in the experiment, we examine the evolution of the pressure field. Figure 2.5 shows the pressure distribution at selected times. From frames b to d, we observe the water-hammer shock propagation toward the distal side

of the droplet interface. The reflected wave is numerically confirmed as a tension wave (negative pressure) at frame e. Note that the liquid phase can support negative pressure (in absolute sense) owing to cohesion (represented by P_∞ in Eq. (2.2)) between closely populated molecules, unless cavitation occurs.

It is instructive to make a rough estimate of the cavitation inception pressure in Fig. 2.4. For this purpose, we superimpose the simulated pressure contours onto the experiment at $t = 10$ μs; see Fig. 2.6. We see that the bubble nucleation can be found roughly within the contour line of -20 MPa. That is, the gelatin gel can support its phase without rupturing on the way of approaching such a strong tension of about -20 MPa. The tensile strength (or equivalently a cavitation threshold) is close to the measurement of Maxwell *et al.* (2013) in which cavitation was induced by the interaction between preexisting bubbles and focused ultrasound pulses in gelatin phantoms and its threshold was measured using a hydrophone. It is also close to the cavitation threshold in distilled water (Herbert *et al.*, 2006). These observations imply that the cavitation in Fig. 2.4 might occur homogeneously as contaminant bubble nuclei or particles that possibly exist in the medium are not activated under such a short tension state.

Finally, we report on the pressure recorded at Lagrangian markers set at $\mathbf{Y}_\epsilon$ inside the droplet in Fig. 2.7. For the range of eccentricity ϵ, every Lagrangian particle is exposed to large tension after 10 μs (see Fig. 2.7 (a)). It follows that the most negative pressure (-33 MPa) is achieved at $\epsilon \approx 0.25$ (see Fig. 2.7 (b)). The recorded tension is far below the Blake threshold pressure, which is determined from the quasistatic mechanical balance of gas bubble nuclei under tension (Brennen, 2014; Harkin *et al.*, 1999; Ida, 2009) and is calculated at -5.6 MPa, for example, for $R_0 = 10$ nm. This clearly suggests the possibility of having cavitation, even from nanobubble nuclei, whose dynamics will be explored based on Rayleigh–Plesset-type calculations as a next step.

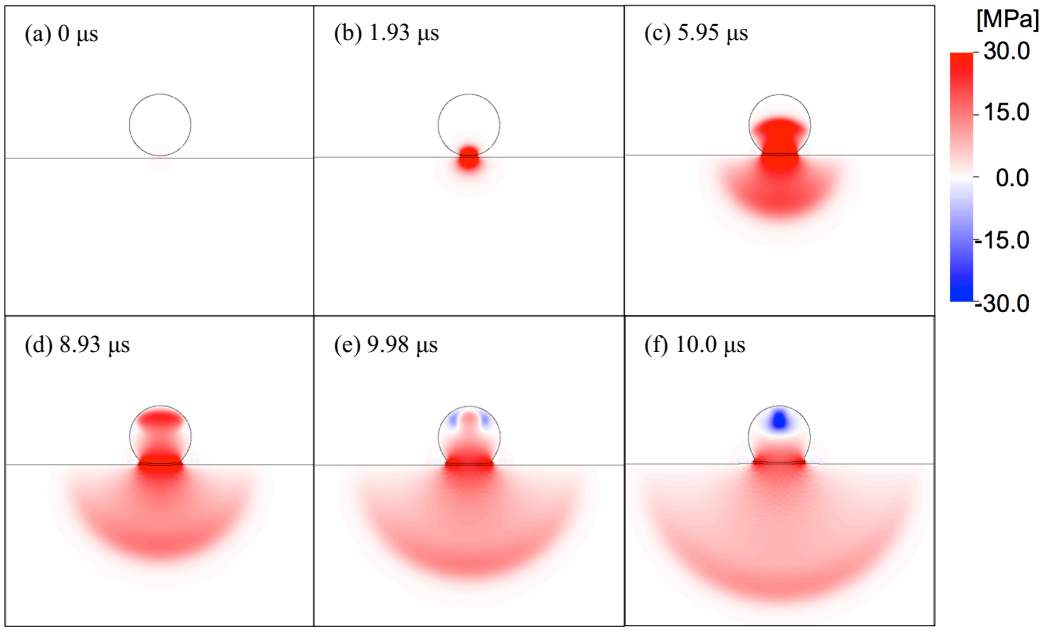

Fig. 2.5: Pressure distributions at different times. Solid lines represent material interfaces. Red and blue regions correspond to compression and tension, respectively.

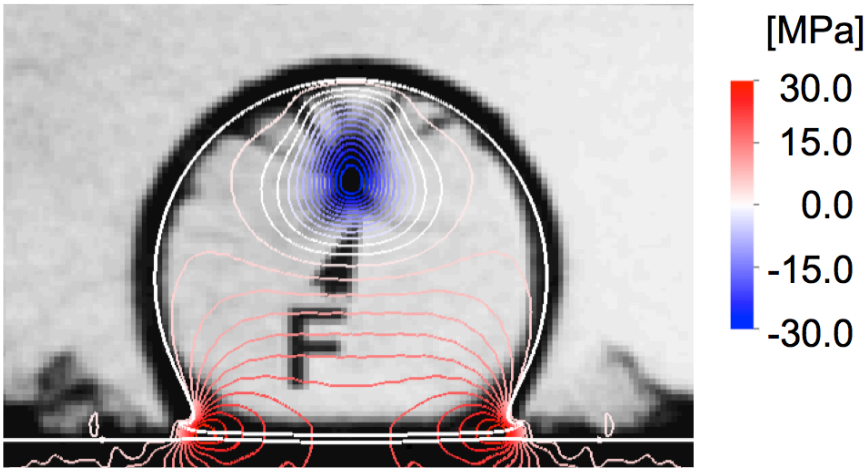

Fig. 2.6: The experimental result at $t = 10$ μs (see Fig. 2.4) superimposed by the simulated pressure contours. Reprinted with permission from J. E. Field *et al.*, "The effects of target compliance on liquid drop impact," *J. Appl. Phys.*, vol. 65, pp. 533–540. Copyright 1989, AIP Publishing LLC.

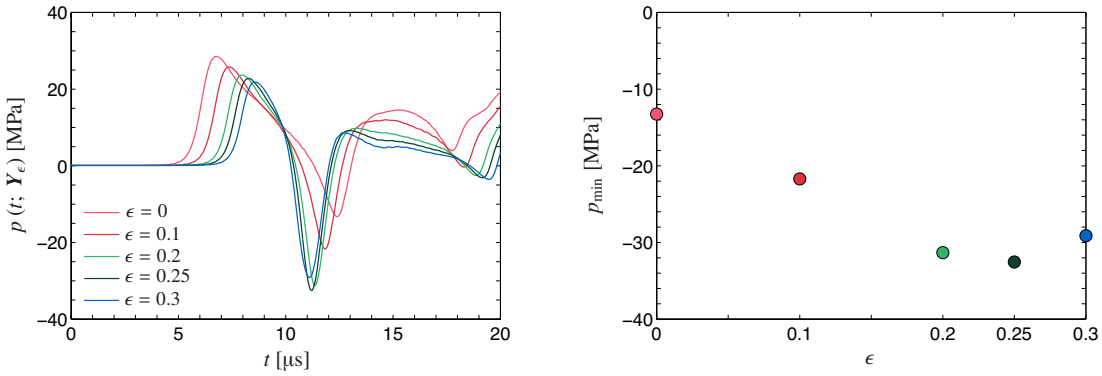

(a) (b)

Fig. 2.7: (a) Pressure evolutions measured at Lagrangian points $\boldsymbol{Y}_\epsilon$. (b) The minimum pressure obtained from the simulations in (a).

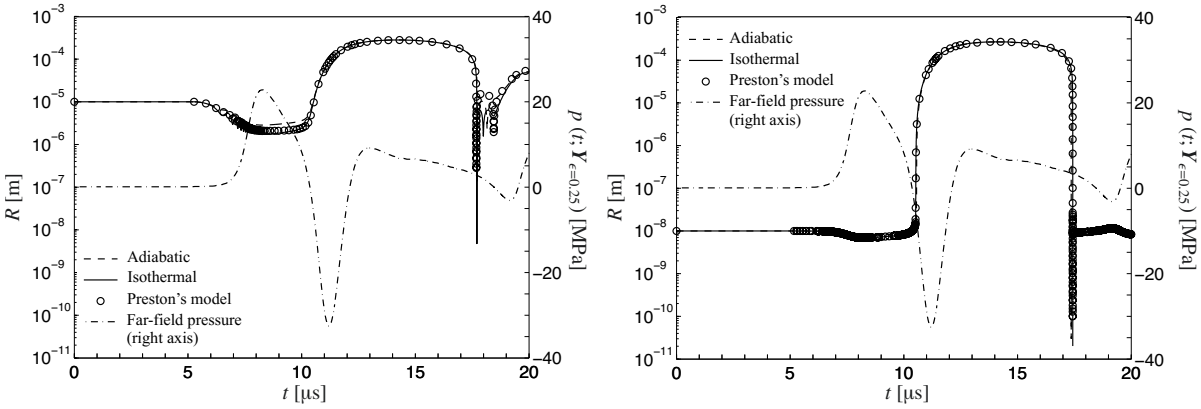

(a) R_0 = 10 μm (b) R_0 = 10 nm

Fig. 2.8: Evolution of the radius of the cavitation bubble nucleated from a gas bubble nucleus whose equilibrium radius R_0 is (a) 10 μm and (b) 10 nm located at $\boldsymbol{Y}_{\epsilon=0.25}$. For reference, the far-field pressure that triggers the bubble dynamics is plotted by dotted lines scaled at the right vertical axis. Simulating the bubble's thermal behavior is according to adiabatic and isothermal relations and the reduced order model of Preston *et al.* (2007) that accounts for diffusive effects at the bubble wall.

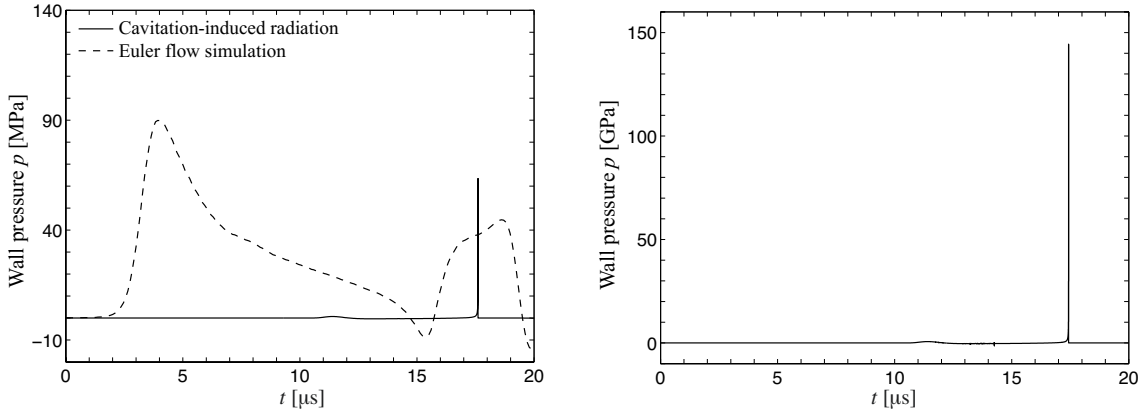

(a) $R_0 = 10$ μm (b) $R_0 = 10$ nm

Fig. 2.9: The pressure radiated from the cavitation bubble nucleated from a gas bubble nucleus whose equilibrium radius R_0 is (a) 10 μm and (b) 10 nm located at $\boldsymbol{Y}_{\epsilon=0.25}$. For reference, the pressure measured at the wall from the Euler flow simulation is also plotted in (a). The bubble's thermal behavior is evaluated by the reduced-order model of Preston *et al.* (2007)

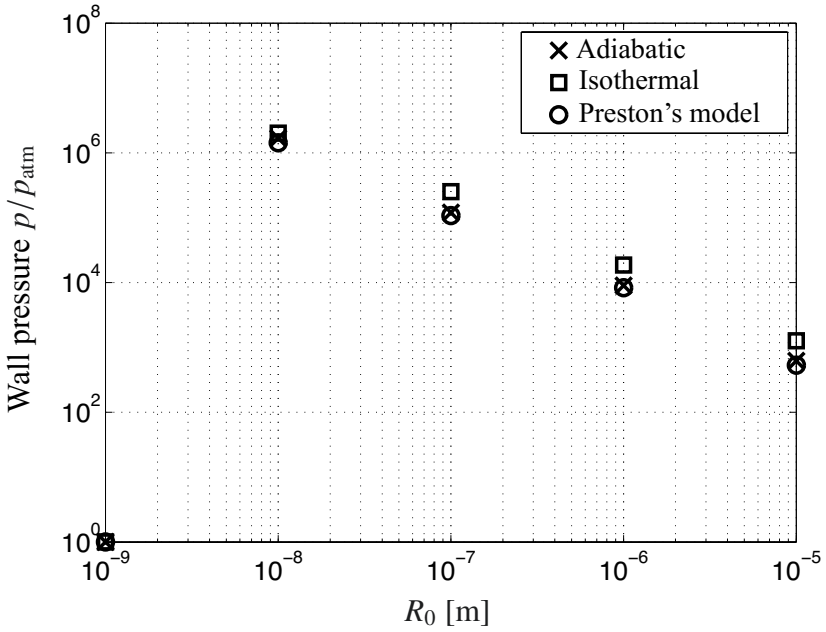

Fig. 2.10: Maximum values in the radiated pressure at the wall as a function of equilibrium nucleus radius R_0. Simulating the bubble's thermal behavior is according to adiabatic and isothermal relations and the reduced-order model of Preston *et al.* (2007).

2.6 Cavitation accompanied by the droplet impact

According to the one-way-coupling method (Section 2.3.2), we showed the possibility of having cavitation due to the wave interaction within the droplet. As a representative example, we consider cavitation bubble nucleation at Lagrangian position $\boldsymbol{Y}_{\epsilon=0.25}$ where the most negative pressure is recorded (see Fig. 2.7). Gas bubble nuclei are assumed to behave either isothermally ($\kappa = 1$) or adiabatically ($\kappa = \gamma$) with their equilibrium size selected at $R_0 = 10$ μm (heterogeneous cavitation) or 10 nm (homogeneous-like cavitation). For comparative purposes, we also examine diffusive effects on bubble dynamics by the reduced-order model of Preston *et al.* (2007). The bubble dynamics corresponding to the far-field pressure at $\mathbf{Y}_{\epsilon=0.25}$ are summarized in Fig. 2.8 (a) for the heterogeneous case ($R_0 = 10$ μm) and (b) for the homogeneous-like case ($R_0 = 10$ nm). It is found that the nuclei exhibit rapid growth to submillimiters, supporting the visible observation of cavitation in the experiment of Field *et al.* (1989) While the collapse dynamics can be controlled by diffusive effects at the bubble wall (Preston *et al.*, 2007), the growth phase is insensitive to the bubble's thermal behavior as confirmed in Fig. 2.8, for the growth rate is simply determined from the inertia of the liquid surrounding the bubble whose pressure is essentially equal to the vapor pressure (Brennen, 2014). Also note that the growth dynamics are rather insensitive to the equilibrium radius of bubble nuclei. Once the nucleus starts to grow, surface tension soon becomes less influential. As a result, the maximum bubble size is expected to be insensitive to the value of equilibrium R_0 (Brennen, 2014; Ceccio & Brennen, 1991). Under this situation, the maximum size is approximated by multiplying the Rayleigh growth velocity (Brennen, 2014) by a period of the tension state and turns out to be 310 μm in this example. This rough estimate leads to reasonable agreement with the simulation results in Fig. 2.8. Meanwhile, it is interesting to note that the rebound after the initial collapse is effectively eliminated in the case of the nanobubble nuclei for which the minimum radius of the collapsing bubble (about 0.1 nm in Fig.

2.8 (b)) is small enough to produce huge damping from viscosity and heat transfer at the bubble wall.

Finally, we examine pressure radiation from dynamics of the nucleated cavitation bubbles in Fig. 2.9 (a) and (b), respectively, for the cases of $R_0 = 10$ μm and 10 nm. The pressure radiation due to the cavitation dynamics is recorded at the wall, $h(t)$ measured from $\mathbf{Y}(t)_{\epsilon=0.25}$, and plotted in this figure. For comparison, the water-hammer pressure at the wall obtained from the Euler flow simulation is also plotted in Fig. 2.9 (a). It follows from the case of $R_0 = 10$ μm that the pressure radiation due to the first collapse ($t \approx 17$ μs) produces a large pressure impulse whose amplitude is comparable to the water hammer. On the contrary, the cavitation bubble collapse for $R_0 = 10$ nm in Fig. 2.9 (b) emits a far larger pressure impulse, but its extreme amplitude would violate the perfect gas law within the collapsing bubble that the Preston's model employs.

In Fig. 2.10, the amplitude of the radiated pressure impulse due to the first collapse is plotted as a function of R_0 (from 1 nm to 10 μm). To see the effect of the bubble's thermal behavior, the results with adiabatic/isothermal bubbles and the Preston's model are presented for each R_0. We first note that cavitation does not occur when $R_0 = 1$ nm, which is below the Blake critical radius and thus stable against the tension within the droplet. More importantly, the pressure radiation from the collapse becomes stronger as the nuclei size decreases. In other words, the cavitation bubble collapse becomes more violent as the ratio of the maximum bubble radius to the equilibrium nucleus radius increases. Even though the pressure amplitude is unreliable because of violating the perfect gas law, this trend gives us an important insight that homogeneous-like cavitation (with smaller bubble nuclei) is expected to produce more violent collapse that gives rise to more erosive impact on target materials. At the end, we should notice from Fig. 2.10 that the results with Preston's model are close to those with adiabatic bubbles, meaning that violent bubble collapse is fast and thus adiabatic even at nanometer scales.

2.7 Summary

In summary, the possibility of cavitation accompanied by high-speed droplet impact against a deformable wall is investigated in one-way coupling manner; the presence of bubble nuclei within the droplet is assumed and the bubble dynamics were determined according to the given pressure variation from the Euler flow simulation. The experiment of Field *et al.* (1989) is reproduced for comparison in which cavitation is observed within the droplet colliding with a solid wall at speed $V_{\mathrm{i}} = 110$ m/s. The current simulation shows good agreement from a viewpoint of acoustic wave propagation within the droplet (see Fig. 2.4 and 2.5): after the collision with the wall, water-hammer shock is propagated within the droplet and its reflection wave (at the distal side of the droplet surface against the wall) focuses at a particular point due to the curvature of the droplet surface. The agreement between the simulated and previously observed focus location of tension wave is excellent (see Fig. 2.6). Given the time history of pressure at Lagrangian markers within the droplet (see Fig. 2.7), one-way-coupling simulation is carried out based on the Rayleigh–Plesset-type calculation (with the equilibrium radius of bubble nuclei varied from submicrons to microns). It suggests the possibility of having cavitation caused by wave interaction within the droplet as shown in Fig. 2.8. More importantly, pressure radiation from the cavitation bubble collapse may overwhelm the initial water-hammer shock; this trend is emphasized for the case of homogeneous-like cavitation that arises from the growth of nanobubble nuclei (see Fig. 2.9 and 2.10). Therefore, such cavitation may be a noteworthy additional erosion factor in the problem of high-speed droplet impact.

Chapter 3

High-speed droplet impact against a dry/wet rigid wall for understanding the mechanism of liquid jet cleaning

3.1 Introduction and outline

In this chapter, we solve compressible Navier–Stokes equations to study both acoustic and hydrodynamic phenomena in high-speed droplet impact problems. We simulate the impact of a spherical droplet (200 μm in diameter) against a dry/wet rigid wall in order to evaluate water-hammer shock loading and wall shear flow after the impact as illustrated in Fig. 3.1. Attached spherical particles of our concern are assumed too small (10 nm in diameter) to disturb the fluid flow, enabling us to evaluate the particle removal in one-way-coupling manner; we judge the removal from a comparison between the particle adhesion and the hydrodynamic force obtained from the droplet impact simulation. Hence, the main contribution of this chapter is to provide comprehensive discussion on the role of high-speed droplet impact in both cleaning and erosion. This chapter is organized as follows. Our model for high-speed droplet impact and particle removal is described in Section 3.2 and the simulation method we use is verified in Section 3.3. In Section 3.4, we perform the droplet impact simulation with varying the impact velocity (30 to 50 m/s) and the water film thickness (up to 200 μm). In particular, we examine the evolution of the

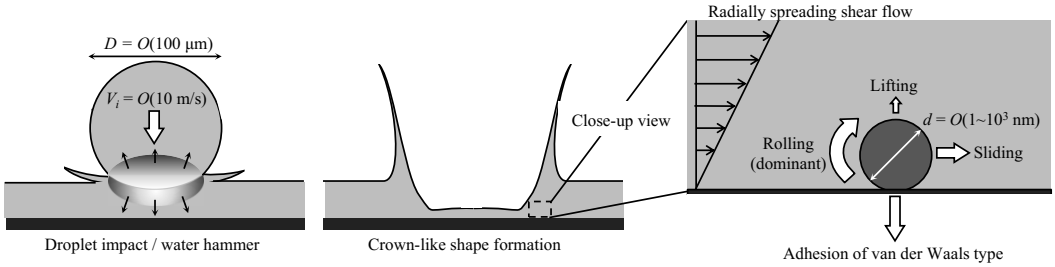

Fig. 3.1: Schematic of high-speed droplet impact against a wet rigid wall that accompanies water-hammer events, side jetting, and crown-like shape formation. In the radially spreading wall shear flow, hydrodynamic force acts on attached particles.

wall shear stress to derive the particle removal criterion in the one-way-coupling method.

3.2 Physical modeling

3.2.1 Problem description

Our study is based on one-way coupling from fluid flow simulation to particle removal evaluation as follows:

1. High-speed droplet impact is simulated, accounting for both compressibility and viscosity, to obtain the evolution of wall shear stress.

2. The simulated wall shear stress can directly be related to the hydrodynamic force acting on attached particles and compared with particle adhesion force of van der Waals type.

The initial configuration of a water droplet (of diameter D) impinging against a rigid wall ($z = 0$) covered with a water film (of thickness l), together with the computational domain, is illustrated in Fig. 3.2; the initial shape of the droplet just before the impact is assumed spherical for simplicity. Even though deformation of the liquid film will be caused by compression waves from the moving droplet (prior to the direct impact) (Mandre *et al.*, 2009), we introduced the idealized initial condition, for the problem to be sim-

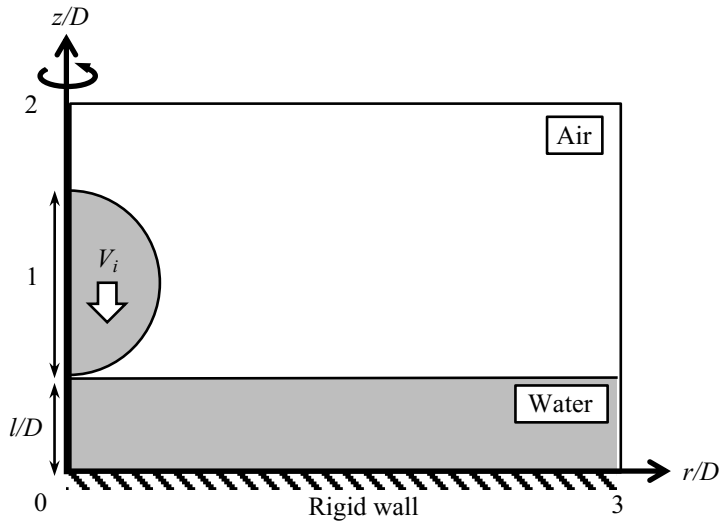

Fig. 3.2: The initial configuration of a spherical water droplet impinging at velocity V_i (at time $t = 0$) towards the wall ($z = 0$) covered with a water film of thickness ($0 \leq l \leq D$). Since the problem is axisymmetric about the z axis, the flow for $r \geq 0$ only is simulated, imposing the reflecting boundary condition (BC) along the z axis of symmetry. The length is normalized by the droplet diameter D.

pler, where the spherical droplet is set into collision against the flat free surface. In this case, the flow becomes axisymmetric so that z denotes the axis of symmetry. Cleaning surfaces are originally dry (before liquid jet cleaning); we may say that the phenomena just after the cleaning process starts are represented by the dry case ($l = 0$). On the contrary, during the cleaning process, the cleaning surface becomes wet; we model it as a rigid wall covered with a water film of uniform thickness l. In both cases, fluids in the computational domain are initially ($t = 0$) set at standsard temperature and pressure (STP; 20°C and 1 atm). Since we are interested in particle removal by liquid shear flow, we do not consider that by capillary force (Sharma *et al.*, 2008; Khodaparast *et al.*, 2017). The droplet is set into motion normal to the wall at three different speeds V_i (30, 40, 50 m/s). As an example, we set the droplet diameter D at 200 μm, which may be a representative value in previous experiments and simulations (Cheng, 1977; Visser *et al.*, 2012, 2015; Haller *et al.*, 2002). The Reynolds number for the droplet is based on the water properties

(see Table 3.1):

$$Re_{\mathrm{D}} = \frac{\rho_{\mathrm{L}} D V_{\mathrm{i}}}{\mu_{\mathrm{L}}}. \tag{3.1}$$

For the cases of $V_{\mathrm{i}} = 30$, 40, and 50 m/s, Re_{D} are calculated as 6000, 8000, and 10000, respectively. The (dimensionless) film thickness, l/D, ranges from 0 to 1.

Spherical particles of very small size are assumed to adhere to the wall ($z = 0$); the particles are assumed too small to disturb fluid flow. In our study, the particle diameter d is set at 10 nm as a representative particle size in silicon wafer cleaning. The particle adhesion is assumed to originate dominantly from van der Waals force. The hydrodynamic force (Section 3.2.4) acting on the particles is calculated given the simulated wall shear flow and compared to the particle adhesion, which allows for deriving the particle removal criterion.

3.2.2 Governing equations for the multi-component fluid flow

To model the flow of our concern, there is a need to consider both compressibility and viscosity of water (and the ambient air). Hence, we solve Navier–Stokes equations for compressible flow consisting of gas and liquid components (with no phase change) in five-equation formulation (Allaire *et al.*, 2002; Perigaud & Saurel, 2005). The system of the five-equation formulation is addressed in Section 2.2.2. Now that the problem is axisymmetric, we solve the equations in two dimensions with source terms that arise from the axisymmetric geometry (Mohseni & Colonius, 2000).

$$
\frac{\partial}{\partial t}\begin{pmatrix} \alpha_{\mathrm{G}}\rho_{\mathrm{G}} \\ \alpha_{\mathrm{L}}\rho_{\mathrm{L}} \\ \rho u_z \\ \rho u_r \\ E \\ \alpha_{\mathrm{L}} \end{pmatrix} + \frac{\partial}{\partial z}\begin{pmatrix} \alpha_{\mathrm{G}}\rho_{\mathrm{G}}u_z \\ \alpha_{\mathrm{L}}\rho_{\mathrm{L}}u_z \\ \rho u_z^2 + p \\ \rho u_r u_z \\ (E+p)u_z \\ \alpha_{\mathrm{L}}u_z \end{pmatrix} + \frac{\partial}{\partial r}\begin{pmatrix} \alpha_{\mathrm{G}}\rho_{\mathrm{G}}u_r \\ \alpha_{\mathrm{L}}\rho_{\mathrm{L}}u_r \\ \rho u_z u_r \\ \rho u_r^2 + p \\ (E+p)\,u_r \\ \alpha_{\mathrm{L}}u_r \end{pmatrix} =
$$

$$
\frac{\partial}{\partial z}\begin{pmatrix} 0 \\ 0 \\ \mathcal{T}_{zz} \\ \mathcal{T}_{zr} \\ u_z\mathcal{T}_{zz} + u_r\mathcal{T}_{zr} \\ 0 \end{pmatrix} + \frac{\partial}{\partial r}\begin{pmatrix} 0 \\ 0 \\ \mathcal{T}_{rz} \\ \mathcal{T}_{rr} \\ u_z\mathcal{T}_{rz} + u_r\mathcal{T}_{rr} \\ 0 \end{pmatrix} - \frac{1}{r}\begin{pmatrix} \alpha_{\mathrm{G}}\rho_{\mathrm{G}}u_r \\ \alpha_{\mathrm{L}}\rho_{\mathrm{L}}u_r \\ \rho u_z u_r - \mathcal{T}_{rz} \\ \rho u_r^2 - \mathcal{T}_{rr} \\ (E+p)\,u_r - (u_z\mathcal{T}_{rz} + u_r\mathcal{T}_{rr}) \\ \alpha_{\mathrm{L}}(u_r - r\nabla\cdot\mathbf{u}) \end{pmatrix}. \quad \begin{matrix} \text{(a)} \\ \text{(b)} \\ \text{(c)} \\ \text{(d)} \\ \text{(e)} \\ \text{(f)} \end{matrix} \tag{3.2}
$$

Here, α_m is the volume fraction of component m where m = G and L stand, respectively, for the gas phase (air) and liquid phase (water), ρ_m is the density of component m, ρ is the mixture density (to be defined by Eq. (3.8)), u_z and u_r are the axial and radial velocity, respectively, $\nabla\cdot\boldsymbol{u}$ is the divergence of the velocity vector field $((\partial u_z/\partial z) + (\partial u_r/\partial r))$, p is thermodynamic pressure, E is total energy (per unit volume), and $\boldsymbol{\tau}$ is the viscous stress tensor whose components are given by

$$
\mathcal{T}_{zz} = \mu\left(\frac{4}{3}\frac{\partial u_z}{\partial z} - \frac{2}{3}\left(\frac{\partial u_r}{\partial r} + \frac{u_r}{r}\right)\right), \tag{3.3}
$$

$$
\mathcal{T}_{rr} = \mu\left(\frac{4}{3}\frac{\partial u_r}{\partial r} - \frac{2}{3}\left(\frac{\partial u_z}{\partial z} + \frac{u_r}{r}\right)\right), \tag{3.4}
$$

$$
\mathcal{T}_{zr} = \mathcal{T}_{rz} = \mu\left(\frac{\partial u_z}{\partial r} + \frac{\partial u_r}{\partial z}\right), \tag{3.5}
$$

where μ is the mixture viscosity (to be defined by Eq. (3.8)). In the above formulation, bulk viscosity is neglected according to Stokes' hypothesis, for our main target is to evaluate wall shear generation associated with the high-speed droplet impact. Thermodynamic pressure, p, is given by the stiffened gas equations of state

$$
\frac{p}{\gamma-1} + \frac{\gamma P_\infty}{\gamma-1} = E - \frac{1}{2}\rho\left(u_z^2 + u_r^2\right), \tag{3.6}
$$

where γ and P_∞ are thermodynamic constants for the mixture and calculated according to the mixture rule (see below). Equation (3.6) can model perfect gases by setting $\gamma = 1.4$ (the ratio of specific heats for air) and $P_\infty = 0$. Table 3.1 summarizes the physical properties of air and water, which are used in the simulation, at STP. With these parameters, the speed of sound in air and water ($c = \sqrt{\gamma(p_0 + P_\infty)/\rho}$ where p_0 is one atmosphere) is calculated, respectively, at 344 m/s and 1500 m/s. Similarly, the speed of sound in the mixture can be calculated according to the mixture rule (see below).

As with Section 2.2.2, mixture quantities for the current physical modeling are summarized as follows:

$$\alpha_\mathrm{G} + \alpha_\mathrm{L} = 1, \tag{3.7}$$

$$\phi = \alpha_\mathrm{G}\phi_\mathrm{G} + \alpha_\mathrm{L}\phi_\mathrm{L}, \tag{3.8}$$

$$\phi = \begin{pmatrix} \rho & \mu & \gamma & P_\infty \end{pmatrix}^\mathrm{T}, \tag{3.9}$$

$$\phi_m = \begin{pmatrix} \rho_m & \mu_m & \gamma_m & P_{\infty,m} \end{pmatrix}^\mathrm{T}, \tag{3.10}$$

where ϕ is a vector composed of respective mixture physical properties in Eq. (3.2) to (3.6) and ϕ_m is a vector composed of respective physical properties of water (m = L) and air (m = G) (see Table 3.1). Here, we note that every mixture quantity including viscous coefficient is defined by arithmetic mean formulation while some numerical schemes employ harmonic mean for higher accuracy (Coward *et al.*, 1997; Patanker, 1991). Indeed the harmonic mean is more accurate than arithmetic mean, but it may violates the robustness of the simulation (Tryggvason *et al.*, 2011). Consequently, arithmetic mean is more favorable for the multicomponent flow, which has large differences of density and viscosity, to prevent the destruction of the computation by numerical instabilities.

Finally, we introduce the assumption of constant thermodynamic properties (μ_m, γ_m, and $P_{\infty,m}$) in our simulation models, even though these are temperature-dependent. Since

Table 3.1: Physical properties of air (ambient) and water (droplet and film) used in the simulation.

	Gas (air, m = G)	Liquid (water, m = L)
μ_m [Pa·s]	1.8×10^{-5}	1.0×10^{-3}
c_m [m/s]	344	1500
ρ_m [kg/m^3]	1.2	1000
γ_m [-]	1.4	6.6
$P_{\infty,m}$ [GPa]	0	0.343

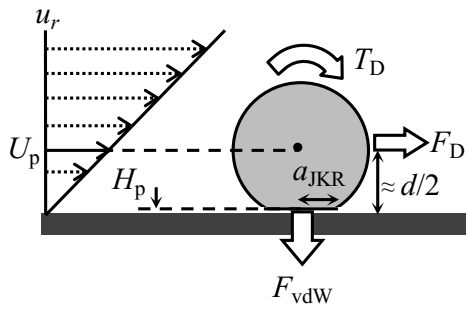

Fig. 3.3: Schematic of the forces and torque acting on a spherical particle attached at a solid surface above which simple shear flow (of water) is created. The contact radius a_JKR is often very small in comparison to the diameter d of spherical particles (i.e., $a_\mathrm{JKR} \ll d$).

wall shear stress calculations are important in this work, we need to consider whether the assumption of the constant properties (especially, water viscosity μ_L) holds. The temperature rise due to the water-hammer shock in our droplet impact problem is very small (less than 1 K) according to the previous study on shock Hugoniot compression (Nagayama *et al.*, 2002). The water temperature can also be increased by viscous dissipation within the wall shear flow after the droplet impact. In Appendix B, we evaluate the effect of the viscous dissipation and conclude that the temperature rise at the wall is at most 0.1 K. Thus, we may say that the assumption of the constant properties is reasonable in our droplet impact simulation.

3.2.3 Partial velocity slip model

To model the spreading of droplets over a dry solid wall, there is a need to permit velocity slip at the wall where the contact line is passing, leading to velocity and stress singularities (Huh & Scriven, 1971; Thompson & Robbins, 1989). While the well-known slip models of Navier (1823) and Maxwell (1890) do not account for velocity components normal to the wall and cannot remove the singularity issue, we adopt that more recently proposed by Thalakkotor & Mohseni (2016) in the present study. In their model, velocity components normal and tangential to the wall are both accounted for and the velocity at the wall is given by

$$u_r|_{z=0} = l_s\left(\frac{\partial u_z}{\partial r} + \frac{\partial u_r}{\partial z}\right). \tag{3.11}$$

The slip length l_s is determined by

$$l_\mathrm{s} = \left(1 - \frac{e_\mathrm{max}}{e_\mathrm{c}}\right)^{-\frac{1}{2}} - 1, \tag{3.12}$$

where e_c is the critical value, and e_max is the principal strain rate of the maximum extension evaluated at the wall ($z = 0$),

$$e_\mathrm{max} = \frac{1}{2}\left(\frac{\partial u_r}{\partial r} + \frac{u_r}{r} + \frac{\partial u_z}{\partial z}\right) + \sqrt{\left(\frac{1}{2}\left(\frac{\partial u_r}{\partial r} + \frac{u_r}{r} - \frac{\partial u_z}{\partial z}\right)\right)^2 + \left(\frac{1}{2}\left(\frac{\partial u_r}{\partial z} + \frac{\partial u_z}{\partial r}\right)\right)^2}. \tag{3.13}$$

In this study, e_c corresponds to the principal strain rate of the maximum extension in the case of droplet impact against a perfect slip-wall, which is thus simulated preliminary. For further details of the slip model, see Thalakkotor & Mohseni (2016).

3.2.4 Criterion for particle removal

Given the velocity profile from the fluid flow computations (Section 3.2.2), one can in principle calculate hydrodynamic force and torque acting on spherical particles attached at the wall, in one-way-coupling fashion, under the assumption that the particles are too small to disturb the base flow. Under the small particle assumption, shear flow around

the particles may be modeled as a linear profile and it enables us to approximate the (near-wall) velocity profile u_r from wall shear stress $\tau_{\mathrm{wall}}(r,t) = \mathcal{T}_{rz}(r,0,t) = \mu(\partial u_z/\partial r + \partial u_r/\partial z)|_{z=0}$:

$$u_r(r,z,t) \approx \frac{z}{\mu}\tau_{\mathrm{wall}}(r,t), \tag{3.14}$$

where the no-slip condition is applied at the wall ($z = 0$). Furthermore, provided that the flow around the particles is creeping, one can analytically obtain the hydrodynamic drag force F_{D} (tangent to the wall) and the torque T_{D} (see Fig. 3.3) from the Stokes' flow formulas (O'Neill, 1968; Busnaina *et al.*, 2002; Burdick *et al.*, 2005; Zoeteweij *et al.*, 2009):

$$F_{\mathrm{D}} = 1.70\left(3\pi\frac{\mu_{\mathrm{L}}^2}{\rho_{\mathrm{L}}}Re_{\mathrm{p}}\right), \tag{3.15}$$

$$T_{\mathrm{D}} = 2.13\left(F_{\mathrm{D}}\frac{d}{2}\right), \tag{3.16}$$

where d is the particle diameter. In the above expression, Re_{p} denotes the particle Reynolds number

$$Re_{\mathrm{p}} = \frac{\rho_{\mathrm{L}}U_{\mathrm{p}}d}{\mu_{\mathrm{L}}}, \tag{3.17}$$

where U_{p} ($=u_r|_{z=d/2}$) is the fluid velocity at the particle center (in the absence of the particle) and is estimated by Eq. (3.14). The particle Reynolds number we encountered in the simulation with particle diameter $d = 10$ nm is at most $Re_{\mathrm{p}} = 0.02$; such a small particle Reynolds number may allow us to validate the one-way-coupling computation of the hydrodynamic force and torque under Stokes' assumption. Thus, the estimation of the hydrodynamic force and torque from Eqs. (3.15) and (3.16) suffices in the sense of one-way-coupling computations.

Since volumetric force such as gravity is negligible for small particles of our target,

the dominant adhesion force is of van der Waals type (Israelachvili, 2011),

$$F_{\mathrm{vdW}} = \frac{A_{\mathrm{H}} d}{12 H_{\mathrm{p}}^2}\left(1 + \frac{2a_{\mathrm{JKR}}^2}{H_{\mathrm{p}} d}\right), \tag{3.18}$$

where A_{H} is the Hamaker constant, H_{p} is the particle-to-surface distance (set at 0.4 nm), a_{JKR} is the contact radius that may be estimated by Johnson-Kendall-Roberts (JKR) theory (Johnson, 1997; Rimai *et al.*, 2000; Israelachvili, 2011) (see Appendix A for the details). In calculating the adhesion force, we consider the case of polystyrene particles attached on a quartz surface, as an example relevant to silicon wafer cleaning in semiconductor industry, according to the previous work of Burdick *et al.* (2005).

In deriving a particle removal criterion, we ignore contributions from volumetric force including inertia, for small particles of our target have large surface areas per unit volume and surface force is believed to be dominating. This means, under the assumption that the rolling mechanism plays a dominant role in particle removal (see Fig. 3.1), that we simply make a comparison between the hydrodynamic torque ($F_{\mathrm{D}}(d/2) + T_{\mathrm{D}}$) and the adhesion-supported torque ($F_{\mathrm{vdW}} a_{\mathrm{JKR}}$). Following the work of Busnaina *et al.* (2002), we introduce the ratio between the two rolling torques:

$$\mathcal{R} = \frac{F_{\mathrm{D}} \frac{d}{2} + T_{\mathrm{D}}}{F_{\mathrm{vdW}} a_{\mathrm{JKR}}}. \tag{3.19}$$

Namely, in this study, particle removal is achieved when $\mathcal{R} > 1$. Substituting Eqs. (3.14) to (3.18) into Eq. (3.19), we can write this relation in terms of the wall shear stress:

$$\mathcal{R} = \frac{5.32(3\pi d)\left(\frac{d}{2}\right)^2 \tau_{\mathrm{wall}}}{\frac{A_{\mathrm{H}} d}{12 H_{\mathrm{p}}^2}\left(1 + \frac{2a_{\mathrm{JKR}}^2}{H_{\mathrm{p}} d}\right) a_{\mathrm{JKR}}}. \tag{3.20}$$

In the one-way-coupling evaluation, the dimensionless number $\mathcal{R}$ is linearly proportional to the wall shear stress. This simple relation agrees with our intuition that particle removal is promoted by larger wall shear stress.

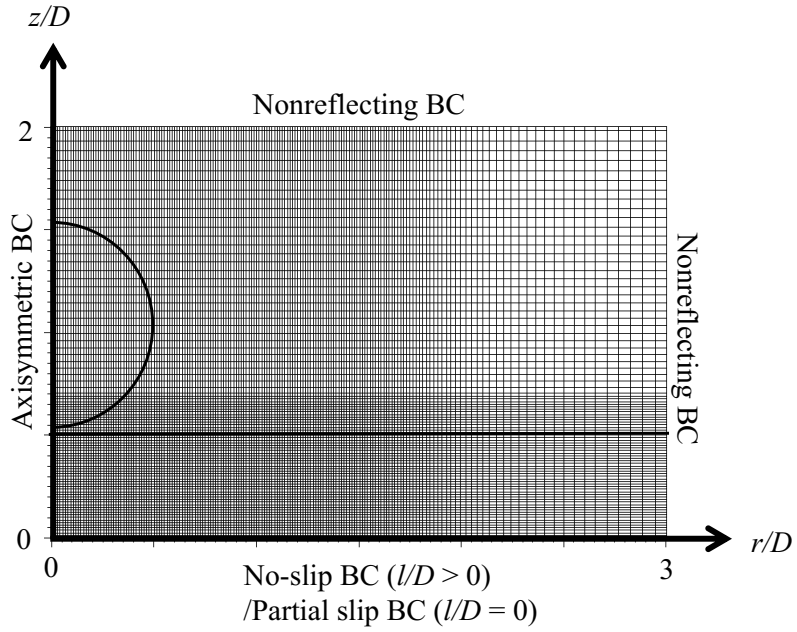

Fig. 3.4: Computational grids (with every 20 grids presented) in which the initial configuration of the water droplet and film location for the case of $l/D = 0.5$ is depicted by thick black lines. The droplet center is initially set at $(z/D, r/D) = ((l/D) + 0.52, 0)$.

3.3 Numerical modeling

3.3.1 Spatial discretization and temporal integration

The numerical method we use is based on the shock-interface capturing scheme proposed by Johnsen & Colonius (2006) and Coralic & Colonius (2014). As with previous Chapter 2.3, the third-order finite-volume WENO scheme is employed for spatial reconstruction, but the numerical flux is calculated by the Harten Lax–van Leer (HLL) approximate Riemann solver (Harten *et al.*, 1983) to adapt the viscous simulation. Though the HLLC approximate Riemann solver is modified from HLL solver for sharp interface capturing, its contribution becomes trivial under the spatial resolution of viscous simulation. To reduce the numerical cost and improve the robustness of the simulation, the HLL approximate Riemann solver is adapted (also according to Beig & Johnsen (2015)). The time integration is handled by a third-order, total variation diminishing Runge–Kutta scheme (Gottlieb & Shu, 1998) with sufficiently small Courant number (< 0.1) (Eq. (2.13)) and diffusion number for viscosity:

$$D_{\mathrm{V}} = \Delta t \max_{i,j}\left(\frac{\mu_{i,j}}{\rho \Delta z_i^2}, \frac{\mu_{i,j}}{\rho \Delta r_j^2}\right), \quad 0 < D_{\mathrm{V}} \leq \frac{1}{2N}. \tag{3.21}$$

This condition allows us to stably compute the viscous flow. We set the (dimensionless) diffusion number below 2.0×10^{-3}.

3.3.2 Computational domain and boundary treatment

The computational grid with the initial configuration of the droplet and film location for the case of $l/D = 0.5$ is presented in Fig. 3.4. Grid stretching across the film is applied in order to resolve the wall shear flow. Here, we show the grid whose resolution is 800 points across the film thickness, $l/D = 0.5$. For the cases of different film thickness, we use the same grid as in Fig. 3.4. The cell Reynolds number of the current resolution, which quantifies the effect of spurious numerical viscosity, is $Re_{\mathrm{cell}} = \rho_{\mathrm{L}} V_{\mathrm{i}} \Delta z / \mu_{\mathrm{L}} = 6$ near the wall for the case of $V_{\mathrm{i}} = 50$ m/s. Thus, the effect of numerical viscosity is sufficiently

small in contrast to the physical viscosity(Vreugdenhil, 1982; Thompson *et al.*, 1985).

Along the z axis of symmetry, we apply the reflecting boundary conditions (BCs) where the cell center is located at the origin ($r = 0$) in finite-volume fashion and the singularity is removed by integration over the origin (Johnsen, 2007). Along the wall whose surface is represented by the cell center, we apply the velocity slip model that is introduced in Section 3.2.3. The velocity gradient normal to the wall, which is necessary for evaluation of the wall shear stress τ_{wall} is calculated by a third-order one-sided difference. At the other boundaries, we apply nonreflecting BCs of Thompson type (Thompson, 1987).

3.3.3 Verification: Stokes' first problem

We numerically solve Stoke's first problem in Cartesian coordinates (x, y) in order to see whether boundary layer flow over the no-slip wall can be resolved by our model. In this case, we omit the geometric source terms from the Navier-Stokes equations for single-phase flow (Eqs. (3.2-a) to (3.2-e)). The wall surface is aligned with the x axis ($y = 0$) and the uniform velocity $u = U = 50$ m/s of the water ($\alpha_{\text{L}} = 1$) in the x direction is initially ($t = 0$) imposed above the wall; the corresponding Mach number is $M = U/c_{\text{L}} = 1/30 < 1$ (subsonic). The computational grid is based on the Cartesian coordinates and its spacing $(\Delta x, \Delta y)$ is uniform ($\Delta x = \Delta y$ for all grid points) but with Courant number fixed at 0.3. Convergence analysis is performed with varying the grid size, for the purpose of selecting the grid resolution used in the droplet impact simulation.

Figure 3.5(a) shows the (dimensional) near-wall velocity profile ($0 \leq y \leq 1$ μm) at $t = 2.6$ μs, which is a representative time in the following droplet simulation. From the analytical solution with self-similarity (denoted by the solid line), the boundary layer thickness (at which the velocity is 99% of the free stream) is $\delta_{99\%} = 6$ μm, which is much larger than the contaminant particles' size of our target. As a result, the (near-wall) velocity profile is effectively linear. The numerical solutions with varying grid size Δy are

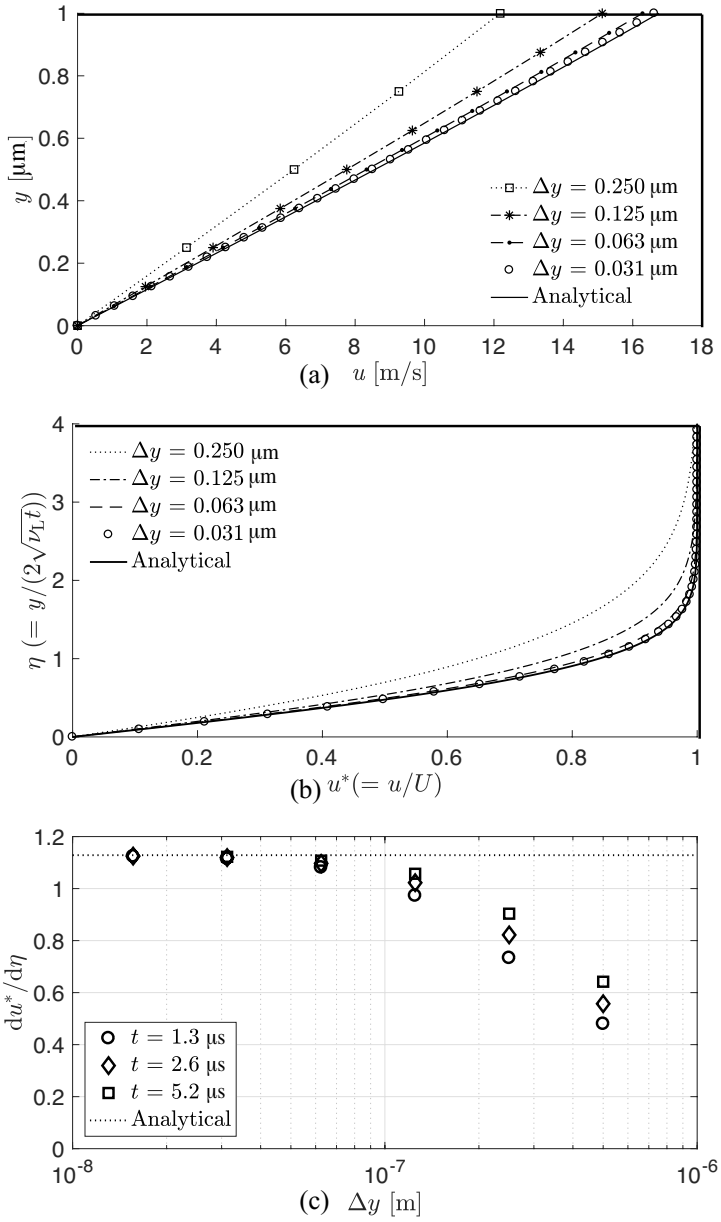

Fig. 3.5: (a) Computations of (dimensional) near-wall velocity profiles with varying the grid spacing Δy at $t = 2.67$ μs in Stoke's first problem. The free stream velocity U is set at 50 m/s; the corresponding Mach number is $M = 1/30$. (b) The nondimensional velocity profiles (at $t = 2.67$ μs) with varying the grid spacing Δy. Since the problem is self-similar, the y coordinate is normalized by boundary layer thickness $2\sqrt{\nu_L t}$ where ν_L is the kinematic viscosity of the liquid. (c) Convergence analysis of the computed velocity gradient at different dimensional times. The analytical value is indicated by the dotted line.

compared to the analytical solution, visually showing that the simulation result converges to the analytical one as the grid size decreases. Since the problem is self-similar, the velocity profile $u^* = u/U$ can be expressed in terms of single coordinate $\eta = y/(2\sqrt{\nu_L t})$ where $\nu_L = \mu_L/\rho_L$ is the kinematic viscosity of the liquid. In Fig. 3.5(b), the velocity profile across the boundary layer thickness at $t = 2.6$ μs is displayed as a function of the normalized coordinate η. This shows that the velocity profile in the boundary layer flow can be captured, provided that the grid is sufficiently fine.

Given the simulated velocity profile in boundary layer flows, our ultimate goal is to evaluate velocity gradients at the wall (and the wall shear stress) for the particle removal judgement (see section 3.2.4). In Fig. 3.5(c), computations of the (normalized) velocity gradient at different representative times in the droplet simulation are plotted as a function of grid size Δy. We note that the solution convergence is the worst for the case of the earliest time at which the boundary layer thickness is the thinnest and the grid resolution is relatively coarse. However, provided that the grid is sufficiently fine, the solution convergence is reasonable even at the earliest time. In the droplet simulation, we choose the near-wall grid resolution at $\Delta z = 0.125$ μm which is obtained by grid stretching as explained in Section 3.3.2.

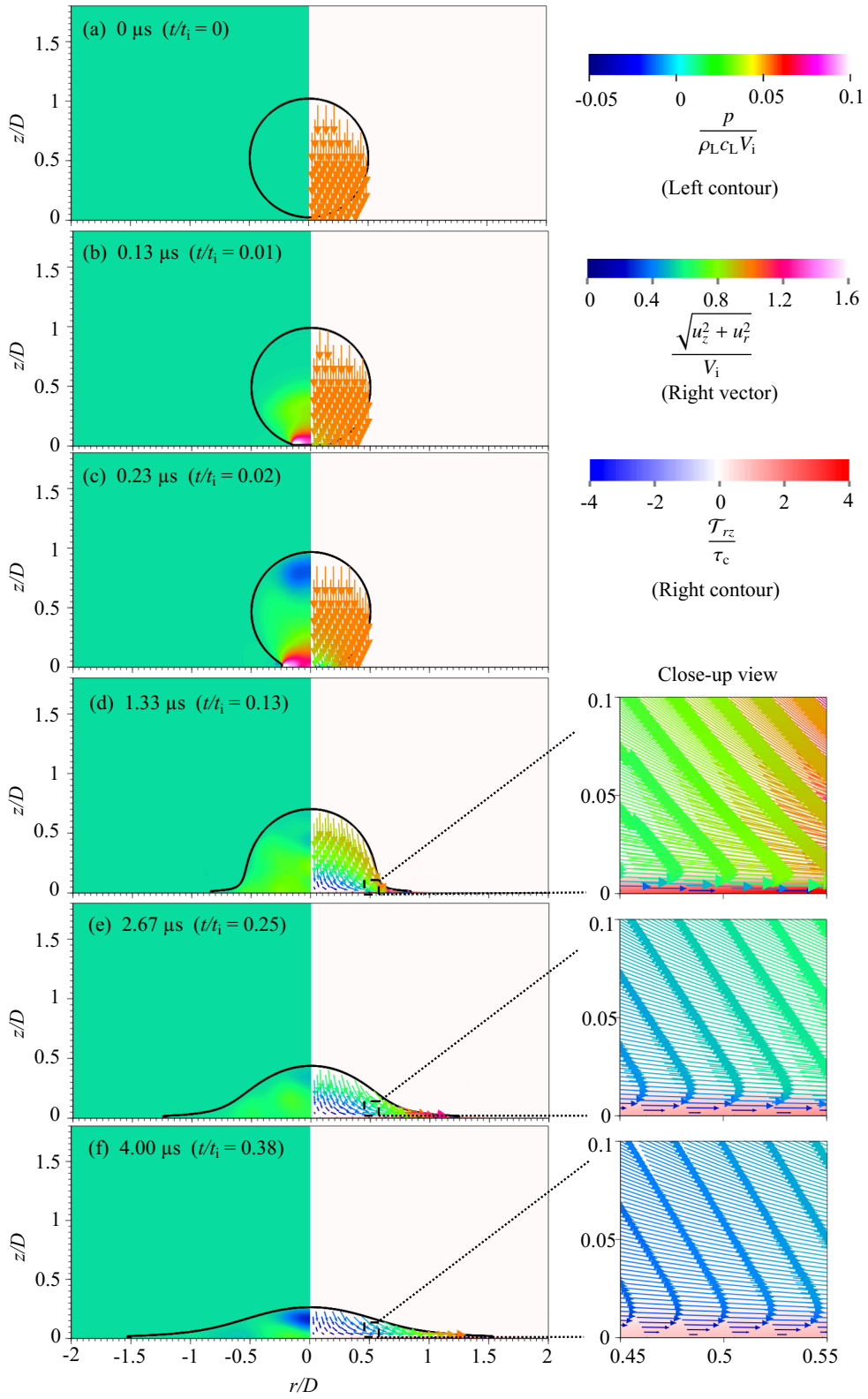

Fig. 3.6: Snapshots of the droplet impact simulation at representative times (a) to (f) for the case of (V_i, l/D) = (50 m/s, 0), plotting the distributions of the pressure (left contour), the liquid velocity (right vector) and the shear stress Eq. (3.5) (right contour) with characteristic wall shear stress (τ_c = 12.5 kPa). The nominal positions of air-water interfaces (α = 0.5) is depicted as black lines. Close-up views of the velocity and shear stress near the wall are presented to show the shear flow development.

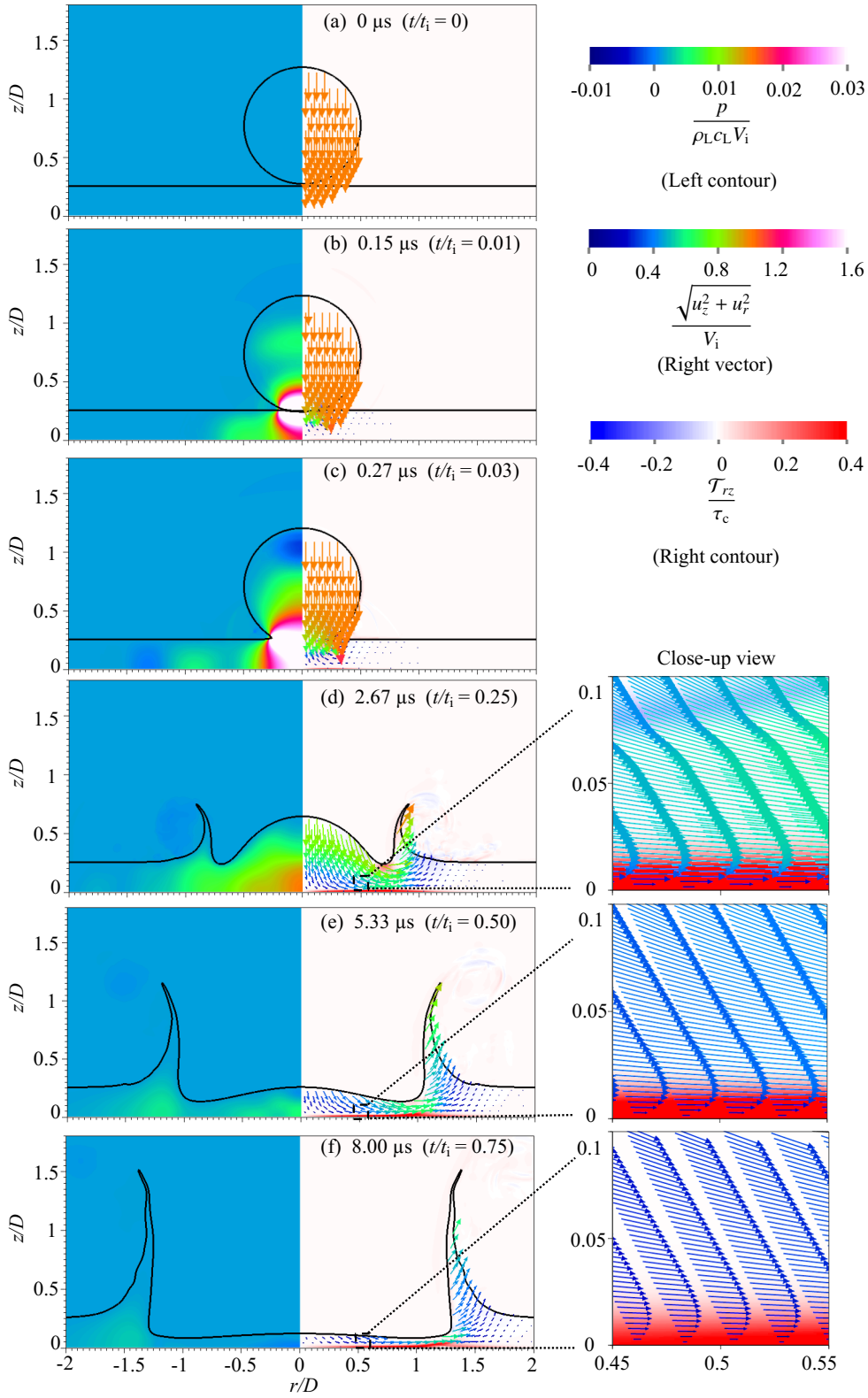

Fig. 3.7: As Fig. 3.6, but with (V_i, l/D) = (50 m/s, 0.25).

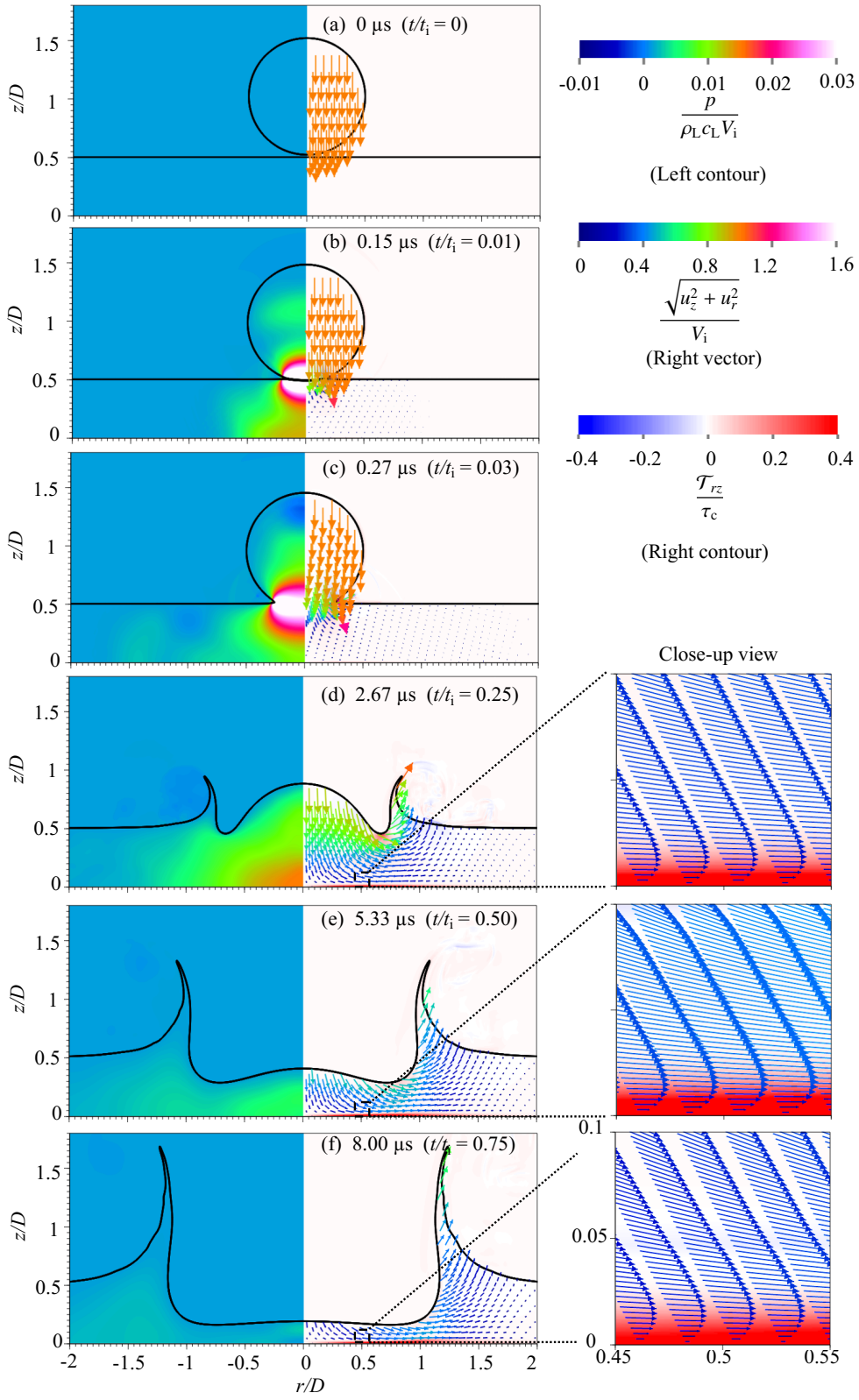

Fig. 3.8: As Fig. 3.6, but with (V_i, l/D) = (50 m/s, 0.5).

3.4 High-speed droplet impact against a dry/wet wall

First of all, we present the big picture of the high-speed droplet impact simulations for the dry ($l = 0$) and wet ($l > 0$) cases. From Figs. 3.6 to 3.8, we plot the evolution of the pressure, velocity, and shear stress fields at representative times for the case of $l/D = 0$, 0.25, 0.5, respectively, with the impact velocity fixed at $V_\mathrm{i} = 50$ m/s. In these figures, frame (a) corresponds to the respective initial conditions. We note that the simulated water-hammer pressure (at the instant of the droplet impact against the wall) records a higher value than the upper limit of the pressure contour in Fig. 3.6. In this plot, we intentionally tune the upper pressure limit in order to clearly visualize pressure fluctuations within the droplet after the impact, for the initial pressure rise just after the impact is too large. In Section 3.5.1, we examine the acoustic phenomena including water-hammer shock loading more carefully. The hydrodynamic events including side jetting and wall shear flow generation are plotted in frames (d) to (f) and are to be examined in Sections 3.6.1 and 3.6.2. The magnitude of the velocity vector is normalized by the initial impact velocity V_i and the pressure is normalized by the water hammer pressure $\rho_\mathrm{L} c_\mathrm{L} V_\mathrm{i}$. The time is normalized by characteristic droplet impact time t_i (to be introduced in Section 3.6.1). The shear stress is normalized by characteristic shear stress τ_c based on representative boundary layer thickness (see section 3.6.2). Results for the case of the other impact velocity ($V_\mathrm{i} = 30$ and 40 m/s) will be discussed in parametric studies in Section 3.6.2.

3.5 Acoustic stage of the impact dynamics

3.5.1 Water-hammer shock loading

We first examine the impact-induced water hammer phenomenon that appears much faster than the subsequent hydrodynamic events. Just after the frame (a) in Figs. 3.6 to 3.8, the droplet collides with the solid wall and the liquid film interface, respectively, for the dry case ($l = 0$) and wet case ($l > 0$). This collision generates a water-hammer shock

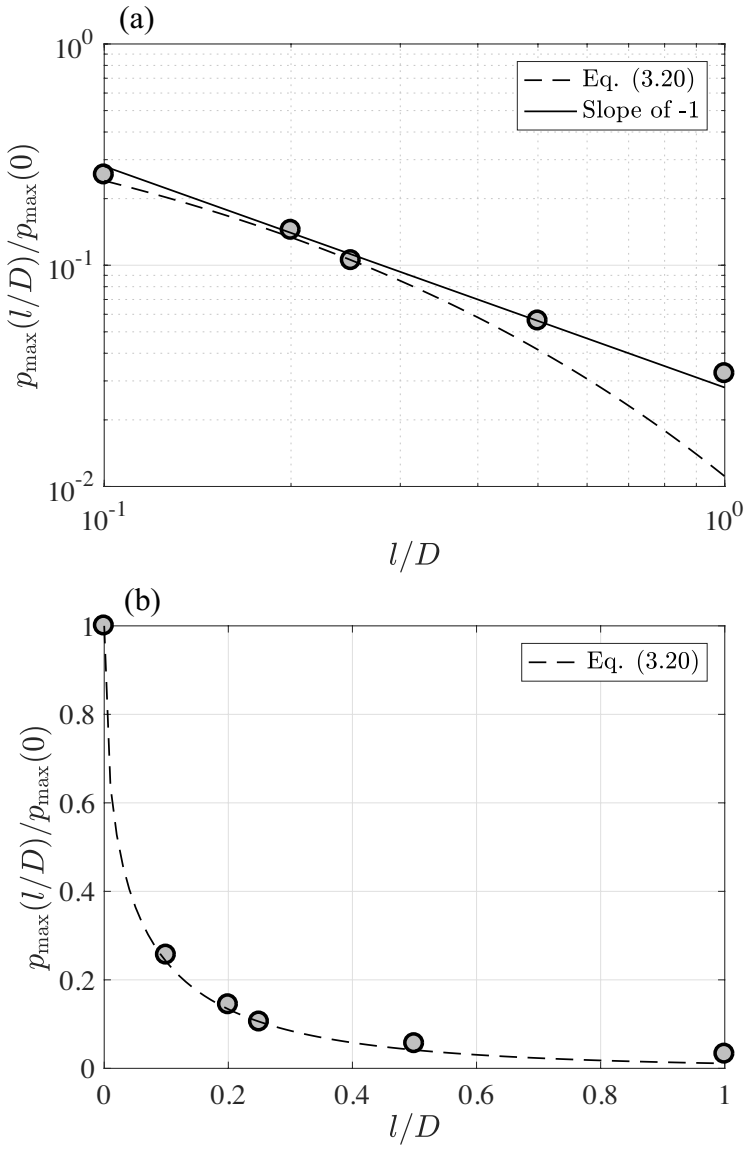

Fig. 3.9: (a) Logarithmic plot of the maximum wall pressure as a function of $l/D > 0$ for V_i = 50 m/s. (b) Linear plot of the maximum wall pressure as a function of $l/D \geq 0$. The vertical axis in both (a) and (b) is normalized by the maximum wall pressure in the dry case $p_{\max}(0)$ = 22 MPa.

(Thompson, 1972). In the frame (b), the water-hammer shock is reflected at the solid wall, giving rise to a high pressure loading on the wall. In the frame (c), the shock propagates towards the distal side of the droplet interface and reflects as an expansion wave, leading to the formation of negative pressure inside the droplet, due to the acoustic impedance mismatch between air and water, as observed in Chapter 2. The acoustic wave generated by the impact keeps reflecting at the droplet interface and being trapped within the droplet.

To clarify the role of the liquid film to damp the impact-induced shock loading on the wall, the maximum pressure at the wall $(r, z) = (0, 0)$ that arises from the initial shock loading for the case of $V_\mathrm{i} = 50$ m/s is defined by $p_\mathrm{max}(l/D) \equiv \max(p(0, 0, t; l/D))$ (over $t/t_\mathrm{i} \in [0, 1]$) and plotted as a function of the film thickness; see logarithmic and linear plots in Fig. 3.9 (a) and (b), respectively. The maximum pressure is normalized by that in the dry wall ($p_\mathrm{max}(0) = 22$ MPa). According to the work by Tatekura *et al.* (2018), calculation of the water-hammer peak pressure that appears at the point contact of spherical droplet impact requires extremely high spatial/temporal resolutions. In this study, we do not intend to resolve the water-hammer event with finer computational grids; rather, we explore a trend in the decay rate of the maximum wall pressure as a function of the liquid film thickness.

Figure 3.9(a) plots the maximum wall pressure for the wet case ($l > 0$) only and shows that the maximum pressure decays as (l/D). In other words, the shock is generated initially by the point-like contact between the droplet and the liquid film and tends to propagate spherically, leading to the decay rate of (l/D) as predicted from the (far-field) linear acoustic theory (Thompson, 1972). When it comes to plotting the maximum wall pressure in the dry case ($l = 0$) in addition to the wet case ($l > 0$), the fitting to the linear acoustic theory for the far field is no longer valid, for the maximum wall pressure in the dry case results from the direct contact between the droplet and the wall and thus consists

of the near-field contributions. To model the functional dependence of the maximum wall pressure on the film thickness ($l \geq 0$), one may use the empirical formula proposed in the previous studies (Sasaki *et al.*, 2016; Fujisawa *et al.*, 2018):

$$\xi = \exp\left(-a\left(\frac{l}{D}\right)^b\right), \tag{3.22}$$

where a and b are fitting parameters. In this particular example, the simulation results for both the dry and wet cases are found to be well fitted to Eq. (3.22) with $a = 4.5$ and $b = 0.5$.

In the context of jet cleaning, a liquid film initially covered at cleaning surfaces will play an essential role in reducing the possibility of erosion due to the impact-induced water-hammer shock loading. However, as will be shown in the following section, the liquid film has an adverse effect when it comes to enhancing cleaning performance.

3.6 Hydrodynamic stage of the impact dynamics

3.6.1 Side jetting

We next examine the hydrodynamic phenomena after the acoustic events; see frames (d) to (f) of Figs. 3.6 to 3.8 where the formation of side jetting (of the water) can be confirmed. In the dry case, the side jet travels along the wall as also seen in Fig. 2.4 and previous studies (Lesser, 1981; Field *et al.*, 1989). On the contrary, in the wet case, the jet direction turns away from the wall; the upward jet eventually forms a crown-like shape, accompanying the thinning of the liquid film inside the crown. It follows from a comparison between Figs. 3.7 and 3.8 that the crown bottom with the thinned liquid film tends to be augmented as the initial film thickness decreases.

In the dry case, one can introduce the following time scale t_i to characterize (low-speed) droplet impact dynamics in the hydrodynamic stage (Pasandideh-Fard *et al.*, 1998):

$$t_\mathrm{i} = \frac{8D}{3V_\mathrm{i}}. \tag{3.23}$$

Approximately at time $t = t_\mathrm{i}$ after droplet impact against dry walls, the droplet spreading over the wall is expected to have its maximal extent. After that ($t > t_\mathrm{i}$), surface tension will come into play and the deformed droplet starts to bounce. Now that we are interested in the early-time impact events, we confine the overall simulation time up to $t = t_\mathrm{i}$; the time scale is normalized by the characteristic time t_i in Eq. (3.23). For reference, the values of t_i is summarized in Table 3.2.

3.6.2 Shear flow formation

While the impinging droplet forms the side jetting flow, a thin shear layer appears in the radially spreading flow above the wall as seen in frame (d) to (f) of Figs. 3.6 to 3.8 and their close-up views just above the wall at $r/D \in [0.45, 0.55]$. Judging from the close-up view of the flow field (around $z/D = 0$, $r/D = 0.5$), the shear layer develops immediately and its time evolution is very small within our observation scope.

To investigate the shear flow in details, we plot the evolution of near-wall radial velocity at $r/D = 0.5$ for the case of $V_\mathrm{i} = 50$ m/s in Fig. 3.10 (a). In these plots, we numerically define boundary layer thickness $\delta = z_k$ such that the minimum index $k \in \mathbb{Z}^+$ for the z-direction grid points with $z_0 = 0$ (the wall surface) satisfies $u_r(z_k) \leq 0.99 u_r(z_{k-1})$. The computed boundary layer thickness δ is overlaid on the radial velocity profiles in Fig. 3.10 (a), showing that the velocity gradient gets less steep as time progresses. The temporal evolution of δ at different radial locations (where strong wall shear stress appears) is plotted in Fig. 3.10 (b). With the Reynolds number Re_D (Eq. (3.1)), we introduce the characteristic boundary layer thickness in droplet impact problems for the case of dry walls (Pasandideh-Fard *et al.*, 1996):

$$\delta_\mathrm{c} = \frac{2D}{\sqrt{Re_\mathrm{D}}}. \tag{3.24}$$

to normalize the z coordinate in these plots. The values of δ_c in our study are summarized in Table 3.2. It turns out that the boundary layer thickness δ measured near the impact

Table 3.2: Values of characteristic impact time t_i (Eq. (3.23)), boundary layer thickness δ_c (Eq. (3.24)) and wall shear stress τ_c (Eq. (3.25)) corresponding to different impact velocities V_i and Reynolds numbers Re_D.

V_i [m/s]	Re_D	t_i [μs]	δ_c [μm]	τ_c [kPa]
30	6000	17.8	5.16	5.81
40	8000	13.3	4.47	8.94
50	10000	10.6	4.00	12.5

point tends to approach the characteristic value δ_c, in the range of film thickness of our target, in our simulation time at which surface tension does not play an important role. We may say that the strong wall shear stress, which is essential for particle removal, will appear in the early stage of the hydrodynamic event. With the characteristic boundary layer thickness δ_c, we can introduce the characteristic wall shear stress:

$$\tau_c = \mu_L \frac{V_i}{\delta_c}, \tag{3.25}$$

whose values in our study are documented in Table 3.2.

Next, we plot the spatiotemporal evolution of the wall shear stress $\tau_{wall}(r, t; l/D)$ for $V_i = 50$ m/s in the *r*-*t* diagram (see Fig. 3.11). We can clearly see (from the contour levels) that the presence of the liquid film at the wall has a significant impact on the wall shear stress and pressure generation. In the dry case ($l/D = 0$), very large wall shear stress $O(10\tau_c)$ appears just after the passage of the moving contact line (immediately after the impact), but its magnitude decays as time progresses. The water-hammer shock wave is generated just after the impact and the wave reflections within the deformed droplet are repeated; the pressure amplitude decays in both space and time. On the contrary, under the existence of the liquid film ($l/D > 0$), the peak values of the wall shear stress and pressure are both suppressed significantly. It is obvious that the suppression effect is emphasized by having the thicker film. In all the cases, the peak values of the wall shear stress appear in our simulation up to the characteristic time t_i (Eq. (3.23)), as inferred from Fig. 3.11 where the steepest velocity gradients near the impact point appear soon after the impact.

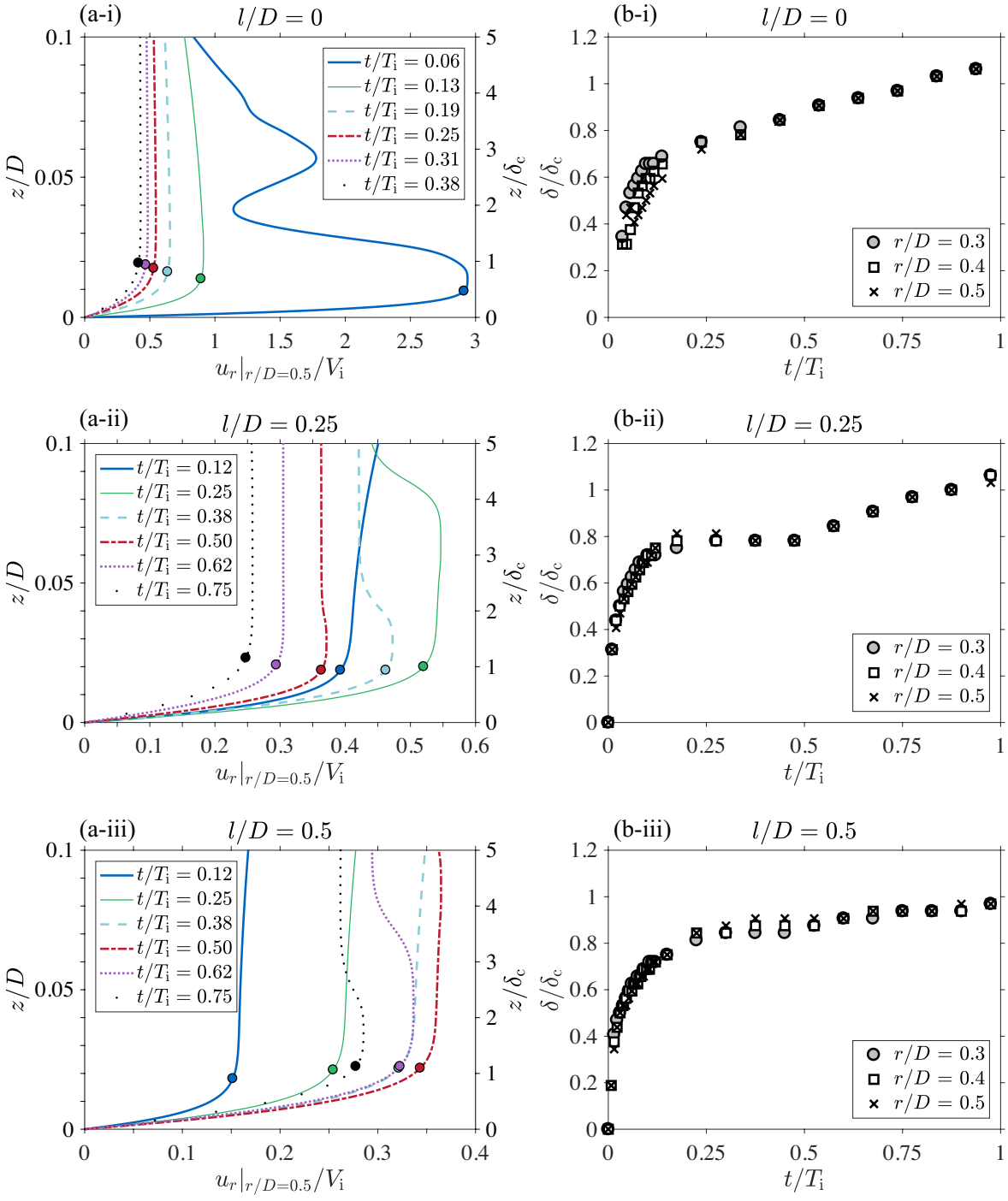

Fig. 3.10: (a) Temporal evolution of the near-wall radial velocity profiles at $r/D = 0.5$. Circle markers correspond to the computed boundary layer thickness δ. The z coordinates in the left-hand and right-hand sides are normalized by initial droplet diameter D and characteristic boundary layer thickness δ_c, respectively. (b) Temporal evolution of the boundary layer thickness δ at different radial positions near the impact point. The results for three different film thickness are presented: (i) $l/D = 0$, (ii) $l/D = 0.25$, and (iii) $l/D = 0.5$.

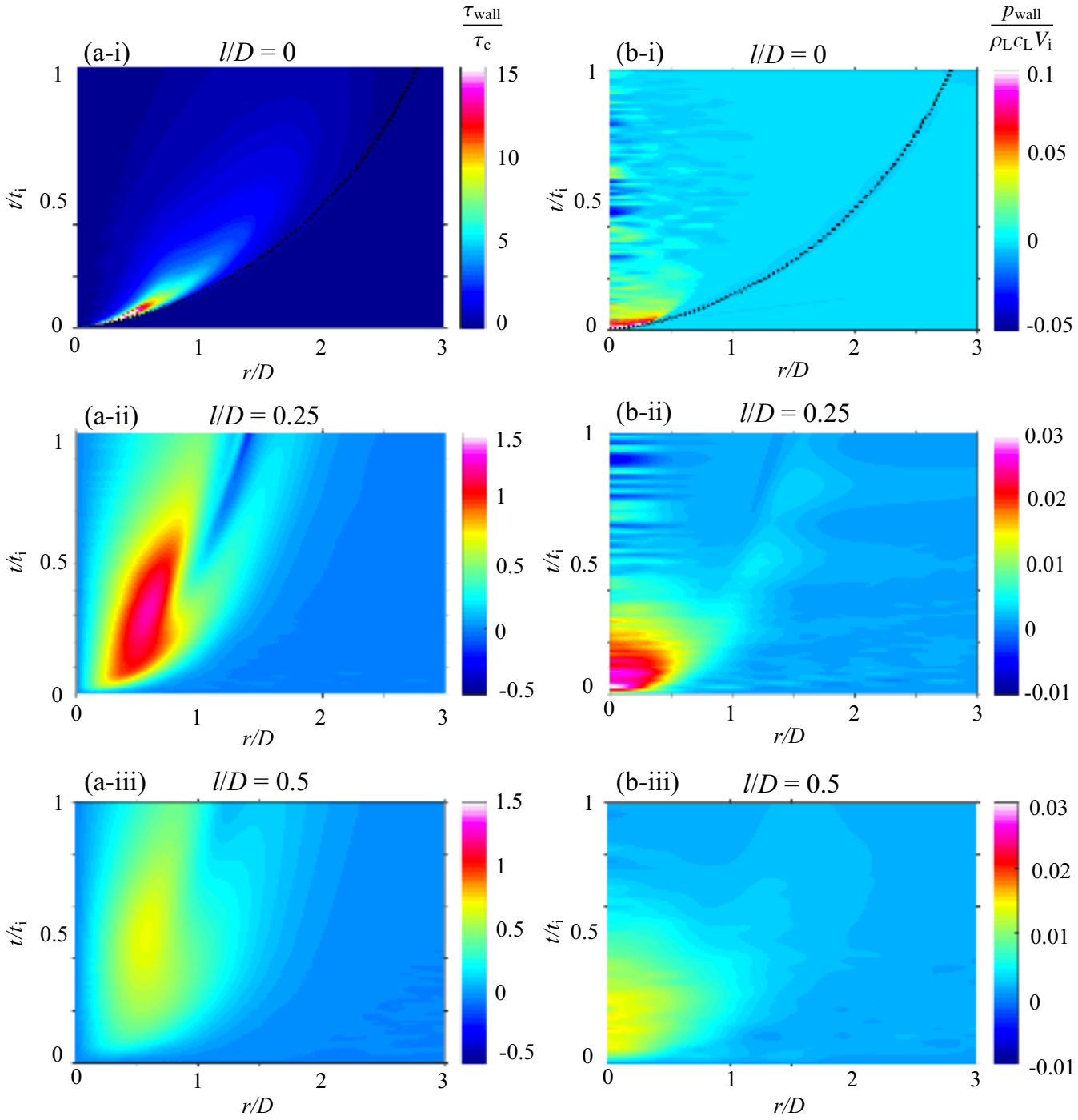

Fig. 3.11: Spatiotemporal evolution of (a) the wall shear stress $\tau_{\mathrm{wall}}(r,t)$ and (b) the wall pressure $p(r,0,t)$ for $V_{\mathrm{i}} = 50$ m/s. The results for three different film thickness are presented: (i) $l/D = 0$, (ii) $l/D = 0.25$, and (iii) $l/D = 0.5$. For the dry case (i), the (nominal) position of the moving contact line at the wall is defined by the threshold $\alpha_{\mathrm{G}} = \alpha_{\mathrm{L}} = 0.5$ and depicted by dotted lines.

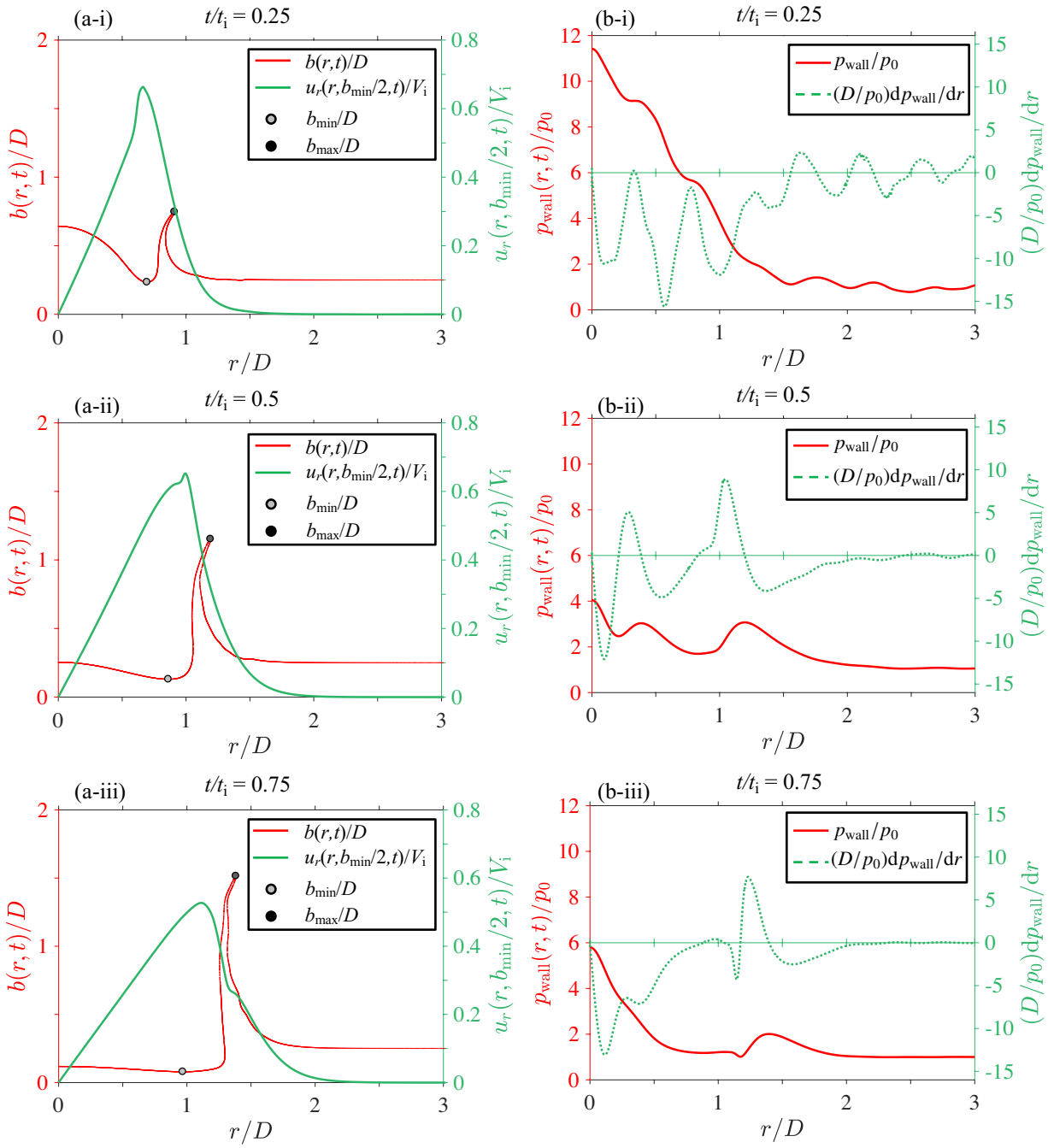

Fig. 3.12: (a) The (nominal) air-water interface profiles $b(r,t)$ defined by $\alpha_G = \alpha_L = 0.5$ (the left vertical axis) and the radial velocity distributions $u_r(r, b_{min}(t)/2, t)$ (the right vertical axis). The maximum and minimum breadths (in the z direction) of the interface are denoted by $b_{max}(t)$ and $b_{min}(t)$, respectively. (b) Distributions of the wall pressure p_{wall} (the left vertical axis) and the pressure gradient $(D/p_0)dp_{wall}/dr$ (the right vertical axis). Results are shown at representative times (i) to (iii) for the case of $(V_i, l/D) = (50\ \text{m/s}, 0.25)$.

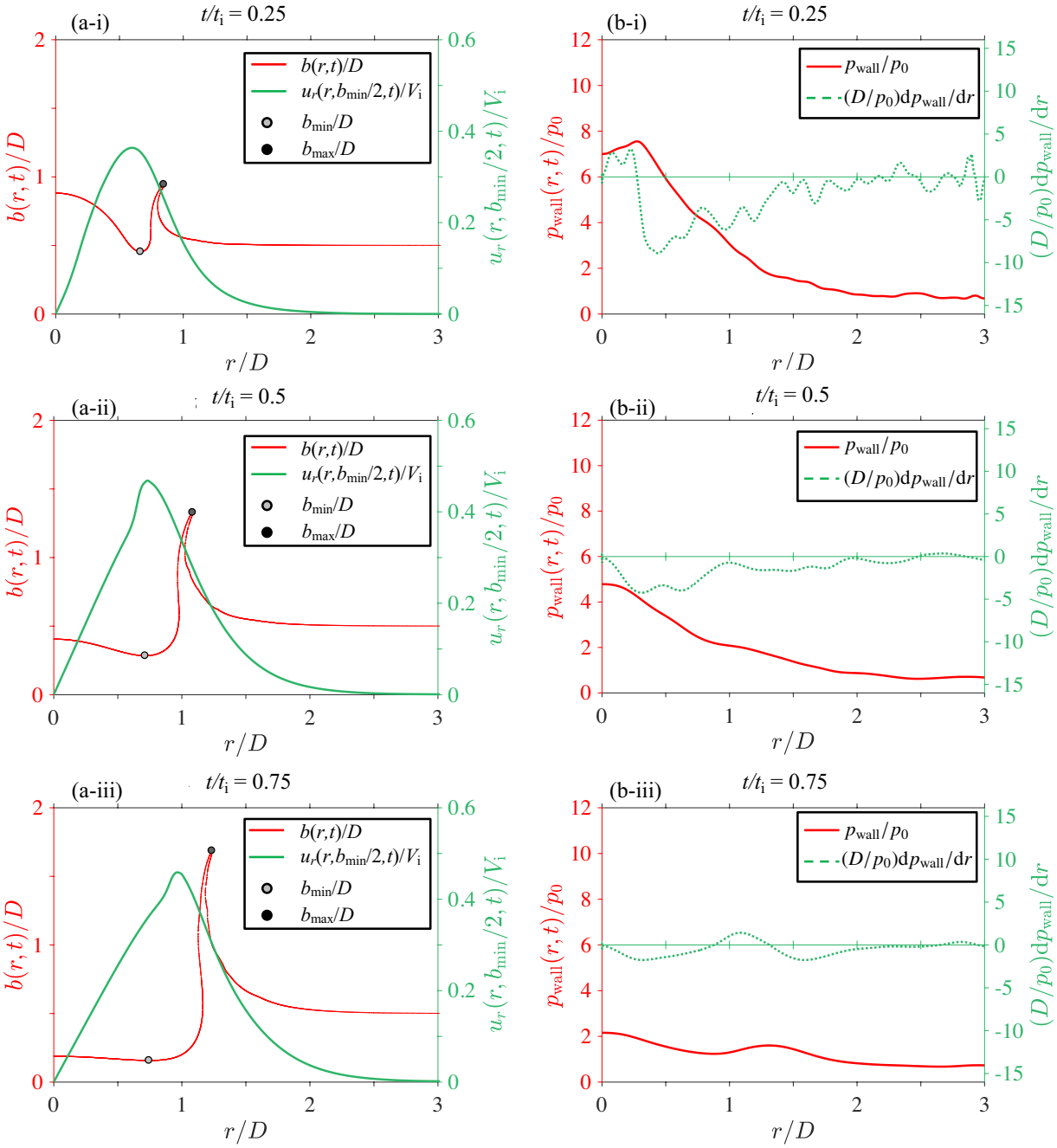

Fig. 3.13: As Fig. 3.12, but with (V_i, l/D) = (50 m/s, 0.5).

Even though it is obvious, we note that the wall shear stress vanishes exactly at the impact point ($r = 0$) about which the flow is axisymmetric; particle removal at $r = 0$ is never achieved by wall shear flow.

We take a more careful look at Fig. 3.11(a-ii) where the strong wall shear stress appears locally in time ($t/t_\mathrm{i} \approx 0.25$) and space ($r/D \approx 0.5$). Such local appearance of the strong wall shear stress corresponds to the hydrodynamic phenomenon that the liquid film is thinned by the droplet impact, thereby accelerating the radial flow of the film (away from the origin). It is of interest to note that negative wall shear stress appears subsequently ($t/t_\mathrm{i} > 0.5$) around $1 < r/D < 1.5$. This means that flow separation ($\tau_\mathrm{wall}(r,t) \leq 0$) occurs at the specific spot. On the other hand, such flow separation does not occur in the dry case ($l/D = 0$) and another wet case ($l/D = 0.5$). To explore the flow separation mechanism, we investigate the relation between the radial velocity and the pressure profiles in the deformed liquid film for the cases of $l/D = 0.25$ and $l/D = 0.5$, respectively, in Figs. 3.12 and 3.13. In Figs. 3.12(a) and 3.13(a), we plot the (nominal) positions of the air-water interface ($\alpha_\mathrm{G} = \alpha_\mathrm{L} = 0.5$) at different representative times. In addition, we plot the radial velocity distributions $u_r(r, b_\mathrm{min}(t)/2, t)$, as a representative velocity inside the deformed liquid film, where b_min denotes the minimum breadth (in the z direction) of the deformed interface defined at each instant. As a result of the emphasized flow deceleration in the thinner liquid film case ($l/D = 0.25$), a remarkable adverse pressure gradient (> 0) arises after the through ($1 < r/D < 1.2$) at $t/t_\mathrm{i} = 0.5$ as in Fig. 3.13(b-ii) and thus gives rise to flow separation and the negative wall shear stress generation as in Fig. 3.12(a-ii). Whether the film flow in the (positive) radial direction is accelerated or decelerated can be explained by volume conservation of the (effectively incompressible) liquid flow as seen in Figs. 3.12(a) and 3.13(a). The flow may be treated as that through a converging-diverging nozzle; it reaches the maximal velocity at the throat (with b_min) and is decelerated in the diverging area (after the throat passage). The flow deceleration

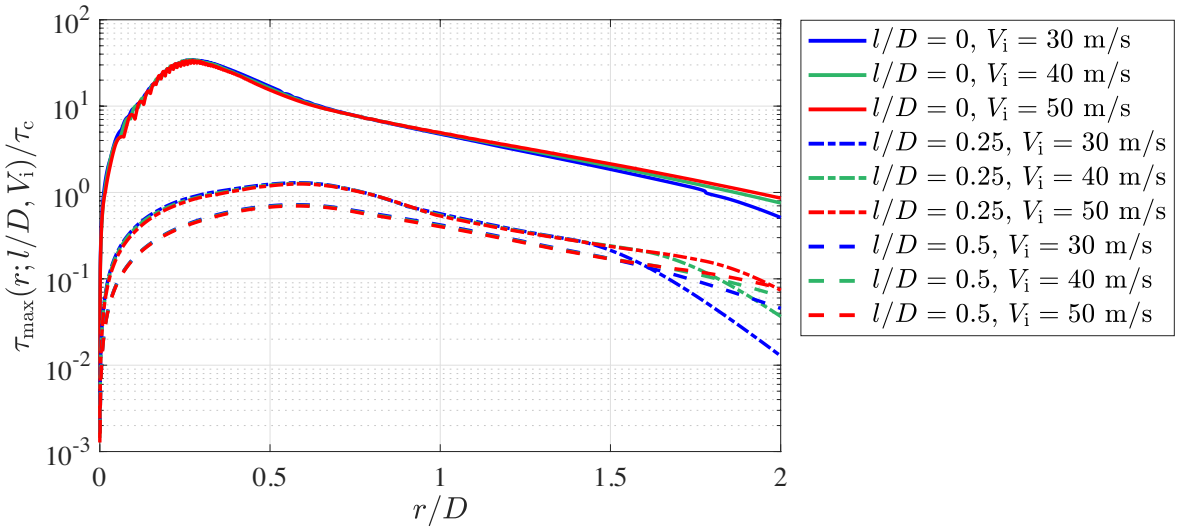

Fig. 3.14: Distributions of the maximum wall shear stress encountered at each radial position, Eq. (3.26), for different film thickness l/D and droplet impact velocity V_i.

is augmented by having the thinner liquid film ($l/D = 0.25$) with which the extent of the flow divergence is emphasized with the larger value of $b_{\max}/b_{\min}$. On the contrary, in the dry case ($l/D = 0$), the breadth (from the wall) of the deformed droplet is monotonically decreasing in the radial direction (as seen in frames (d) to (f) of Fig. 3.6), implying that strong flow deceleration does not occur and flow separation with negative wall shear stress is thus not observed in Fig. 3.11(a-i). Additionally, note that pressure fluctuation at $t/t_\mathrm{i} = 0.25$ is came from the reflection waves of the water-hammer shock as mentioned in Section 3.5.1 and this effect is found to be less important for the flow separation, for the adverse pressure gradient is relatively small compared with the latter time frames.

The maximum wall shear stress encountered at each radial position is defined by

$$\tau_{\max}(r; l/D, V_\mathrm{i}) = \max_{t/t_\mathrm{i} \in [0,1]} (\tau_{\mathrm{wall}}(r, t; l/D, V_\mathrm{i})), \tag{3.26}$$

and its distribution is plotted as a function of distance r for $V_\mathrm{i} = 30,\ 40,\ 50$ m/s and $l/D = 0,\ 0.25,\ 0.5$, respectively, in Fig. 3.14. It turns out that distributions of the maximum

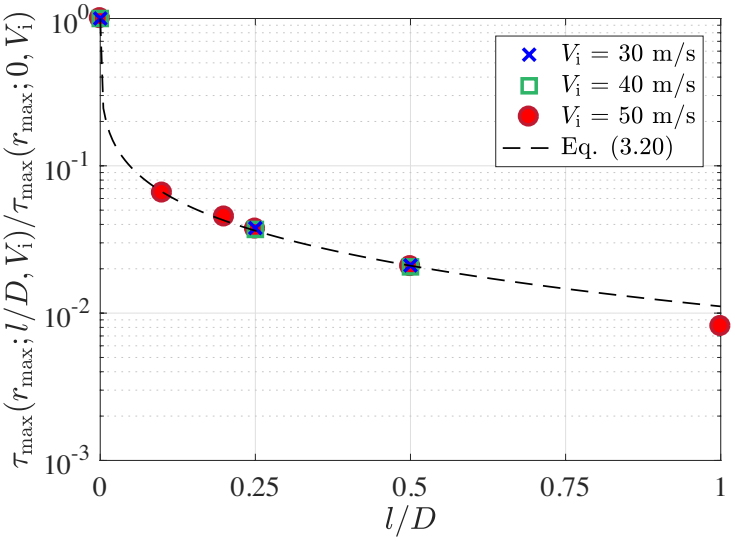

Fig. 3.15: The maximum wall shear stress defined over both time and space as a function of film thickness l/D. Results for different impact velocity V_i are plotted. The vertical axis is normalized by the maximum wall shear stress in the dry case, $\tau_{\max}(r_{\max}; 0, V_\mathrm{i}) = 199$ kPa, 308 kPa, and 402 kPa, respectively, for $V_\mathrm{i} = 30$ m/s, 40 m/s, and 50 m/s. The simulation data are fitted to Eq. (3.22) with $a = 4.5$ and $b = 0.22$.

shear stress (Eq. (3.26)) for each value of the liquid film thickness l/D are very similar, under normalization by the characteristic shear stress τ_c (Eq. (3.25); see its value in Table 3.2), between the different impact velocities V_i of our concern. For each distribution of the maximum wall shear stress $\tau_{\max}(r)$, we can find one peak position $r_{\max}$ at which the value $\tau_{\max}(r_{\max})$ is maximal. The peak position $r_{\max}$ is found to be shifted away from the impact point ($r = 0$) under the existence of the liquid film at the wall. Since the peak wall shear stress $\tau_{\max}(r_{\max}; l/D, V_\mathrm{i})$ found in Fig. 3.14 can be interpreted as an important quantity in the sense of particle removal, we plot it with varying the values of l/D and V_i in Fig. 3.15. For the case of $V_\mathrm{i} = 50$ m/s, we perform the simulations with $l/D = 0.1$, 0.2 and 1 (in addition to $l/D = 0$, 0.25 and 0.5) and plot the results in this figure. Now that the peak wall shear stress is normalized by that for the case of $l/D = 0$, its value is indistinguishable between the different values of V_i of our concern. Obviously, the peak

wall shear stress is suppressed by having the thicker liquid film, implying that the particle removal performance will be lowered under the existence of the film. The suppression rate may be modeled by Eq. (3.22) as in the case of the water-hammer pressure in Fig. 3.9(b); the fitting result with $a = 4.5$ and $b = 0.22$ shows reasonable agreement with the simulation data.

3.7 Particle removal judgement

Given the fluid flow computation, we finally discuss, with the one-way-coupling manner (Section 3.2.4), the removal of spherical polystyrene particles attached at the wall of a quartz surface with their diameter d set at 10 nm. In Fig. 3.16, the spatiotemporal evolution of the dimensionless parameter $\mathcal{R}$ that represents the ratio of hydrodynamic torque to adhesion-supported torque (see Eq. (3.20)) is plotted for different film thickness l/D and impact velocity V_i. We judge particle removal when $\mathcal{R} > 1$ under which the hydrodynamic torque acting on the attached particles defeat that supported by the adhesion force of van der Waals type. In these plots, the threshold value ($\mathcal{R} = 1$) is depicted by solid lines. Obviously, wall shear stress is never generated at the impact point ($r = 0$) about which flow is symmetric, so that particles sitting at $r = 0$ are never removed by the hydrodynamic effects ($\mathcal{R} = 0$); the threshold line ($\mathcal{R} = 1$) never intersects the origin $(r, t) = (0, 0)$. Once the spot of concern is swept with the threshold line, the particles are considered to be removed. Note that for the case of $V_\mathrm{i} = 30$ m/s (the lowest impact velocity) and $l/D = 0.5$, the value of $\mathcal{R}$ is smaller than unity in the entire space; we cannot obtain any particle removal in this case. Neglecting reattachment of the removed particles, we can define the particle removal area A (of annular shape) by

$$A = \pi \left(R_\mathrm{max}^2 - R_\mathrm{min}^2 \right), \tag{3.27}$$

where R_min and R_max stand for the minimum and maximum radial positions of the threshold lines ($\mathcal{R} = 1$), respectively (see Fig. 3.16). In Fig. 3.17, we plot the computed values

of A for different film thickness l/D and impact velocity V_i. It is obvious that the cleaning performance becomes maximal (with the largest A) in the dry case $l/D = 0$ and lower (with smaller A) as the film thickness increases. As expected, the lower impact velocity also gives rise to the lower cleaning performance. So far, we have numerically examined the acoustics and hydrodynamics of high-speed droplet impact against dry/wet rigid walls and then evaluated the removal of small particles attached at the wall surface in the one-way coupling manner. In the context of droplet-impact-based cleaning, we can confirm, from these simulations, a trade-off relation between the cleaning performance enhancement and the erosion reduction. With the higher impact velocity and the thinner liquid film, the cleaning performance will be higher but the erosion will be more likely to occur. Technically, there is a need to explore the optimal cleaning conditions at which the cleaning is more efficient but less erosive.

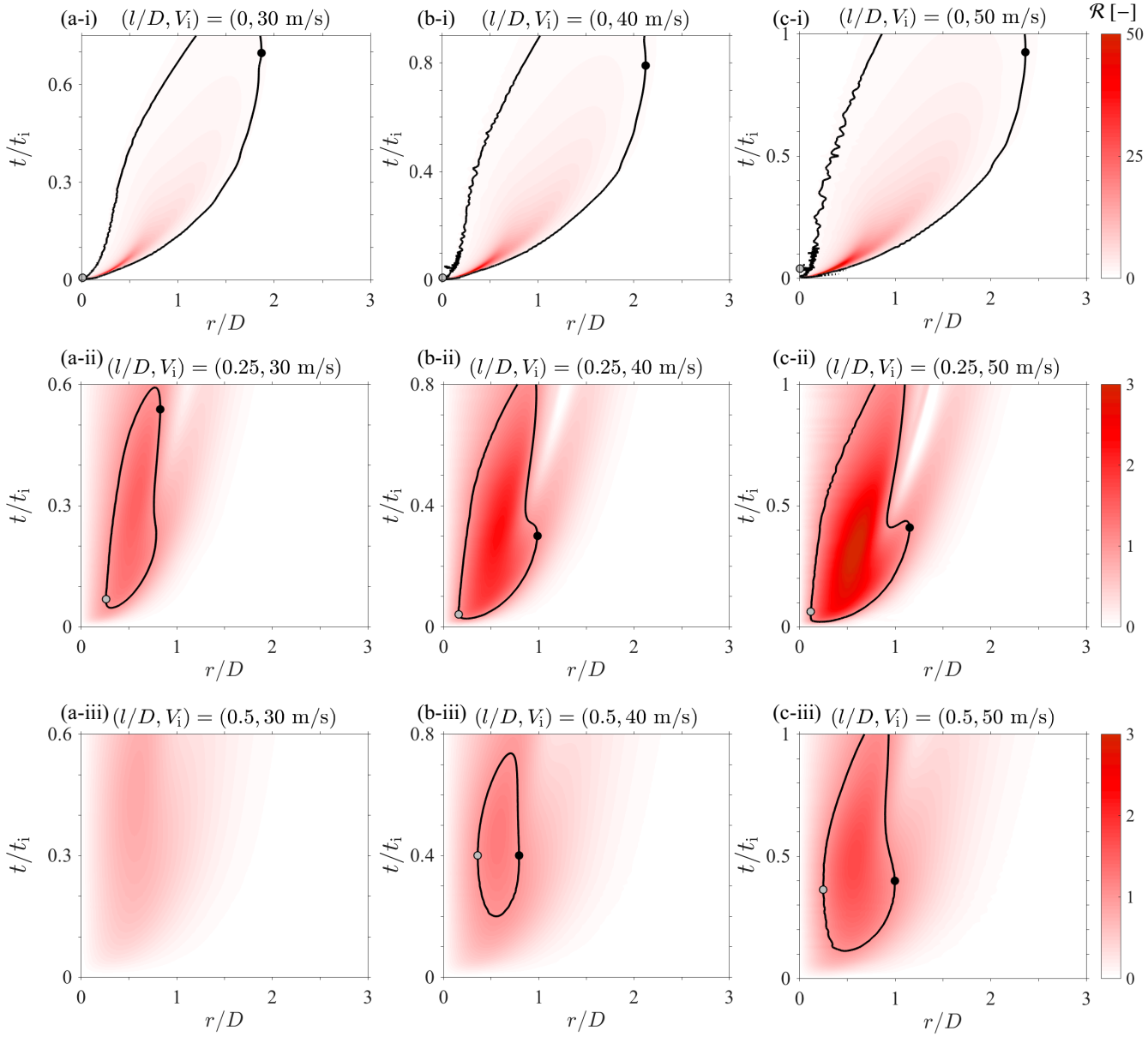

Fig. 3.16: Spatiotemporal evolution of dimensionless parameter $\mathcal{R}$, Eq. (3.20), to judge particle removal for droplet impact velocity at (a) $V_\mathrm{i} = 30$ m/s, (b) 40 m/s, and (c) 50 m/s, particle diameter fixed at $d = 10$ nm and for different film thickness (i) $l/D = 0$, (ii) $l/D = 0.25$, and (iii) $l/D = 0.5$. The threshold value ($\mathcal{R} = 1$) is depicted by solid lines; $\mathcal{R} > 1$ means particle removal. Gray and black dots depict the position and time of R_min and R_max, respectively.

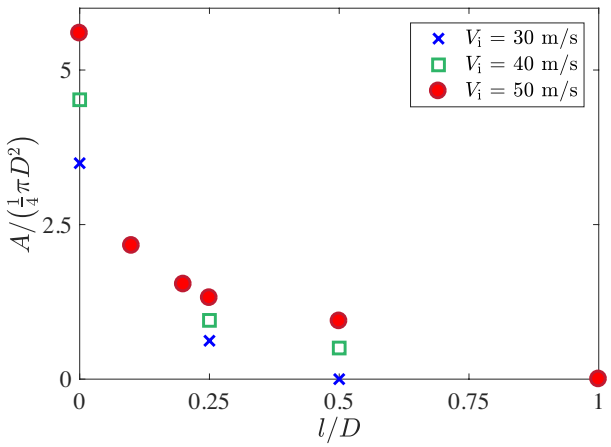

Fig. 3.17: The particle removal area A, calculated according to Eq. (3.27) and the results in Fig. 3.16, with varying film thickness l/D and droplet impact velocity V_i.

3.8 Summary

In summary, high-speed droplet impact against dry/wet rigid walls was simulated and discussed it in the context of particle removal. We reproduced high-speed impact of a spherical water droplet (200 μm in diameter) with varying the impact velocity (up to 50 m/s) and the thickness of a water film at the wall surface (up to the droplet diameter), based on the compressible Navier–Stokes equations. Note that the impacting droplet is assumed to behave axisymmetric. First, the acoustic phenomena in the droplet-impact problem was quantified. The maximum wall pressure beneath the droplet center is found to be attenuated by having the thicker liquid film and its decay rate can be fitted empirically by an exponential function (see Fig. 3.9). Next, we quantified the wall shear flow generation after the acoustic events (see Fig. 3.10). In the dry wall case, the side jet forms in the lateral direction to the wall surface (see Fig. 3.6) and very large wall shear stress appears just after the passage of the moving contact line (see Fig. 3.11). On the contrary, in the wet wall cases, the jet results in the formation of a crown-shape free surface (see Fig. 3.7

and 3.8). The wall shear stress is damped significantly under the presence of the liquid film; flow separation can be caused by flow deceleration in the crown-shape liquid film, depending on the film thickness (relative to the droplet diameter as shown in Figs. 3.12 and 3.13). Finally, we considered the case of very small polystyrene particles (10 nm in diameter) attached at the wall of a quartz surface and evaluated the particle removal from a balance of the adhesive force (of van der Waals type) and the hydrodynamic force (under the Stokes' approximation) as described in Eq. 3.20. Results are summarized in Fig. 3.16. As expected, the particle removal area is augmented by having larger impact velocity and thinner films. We may say that the present simulation approach is helpful when it comes to exploring the optimal cleaning conditions at which the performance of cleaning by the wall shear flow is maximal while the erosion caused by the water-hammer shock loading is minimal.

Chapter 4

Wall shear flow generated by bubbles collapsing near a rigid wall

4.1 Introduction and outline

In this chapter, we perform the three dimensional, compressible Navier–Stokes simulation of the spherical bubble collapse near a flat rigid wall to clarify the wall shear flow formation. To examine the fundamental characteristics, we simulate the so-called Rayleigh collapse of air bubble (100 μm in radius at equilibrium state) near the wall, whose driver is considered as sudden pressure increase (around 20 to 100 times larger than one atmosphere) at surroundings of the bubble (Rayleigh, 1917). That is, we only focus on the stage of the bubble collapse, which can dominantly play a role in cleaning, for simplicity while the bubble growth may not involve the high-speed flow generation near the wall. This simple problem is reasonable to compute with sufficient resolutions and helpful to understand the detailed dynamics of the microjet formation in the nonspherical collapse. Here, we carry out the parametric studies about the standoff distance from the wall to the bubble center. Finally, we discuss the cases of collapsing bubble pair and examine the effect of bubble-bubble interactions in wall shear flow formation by changing the distance between two bubbles. That is, the bubble dynamics of our concern includes three dimensional behavior. To discuss both the single bubble collapse and two bubbles collapse with the same numerical framework and resolutions, we perform three dimensional

Table 4.1: Simulated cases of parametric studies for driving pressures Δp, standoff distances h and inter-bubble distances d. Single bubble collapse is noted as $d = \infty$, and $2.2 \leq d < \infty$ means collapse of a pair of the same-sized bubbles

Δp [MPa]	h/R_0	d/R_0
2	1.01	∞
2	1.1	∞
2	1.2	∞
2	1.3	∞
5	1.01	∞
5	1.1	∞
5	1.2	∞
5	1.3	∞
10	1.01	∞
10	1.1	∞
10	1.2	∞
10	1.3	∞
5	1.1	2.2
5	1.1	2.3
5	1.1	2.4
5	1.1	2.5
5	1.1	3.0
5	1.1	4.0
5	1.1	8.0

simulations in every case.

This chapter is organized as follows. Physical model and problem setup are described in Section 4.2 and the simulation method we use is verified in Section 4.3. In Section 4.4, we first show the simulation of single bubble collapse near a rigid wall with varying the driving pressure (2 to 10 MPa) and the bubble to wall distance (101 to 130 μm). Finally, the collapse of two bubbles near a rigid wall with varying the inter-bubble distance is simulated in Section 4.5 and it reports the remarkable wall shear stress decaying due to the bubble-bubble interaction.

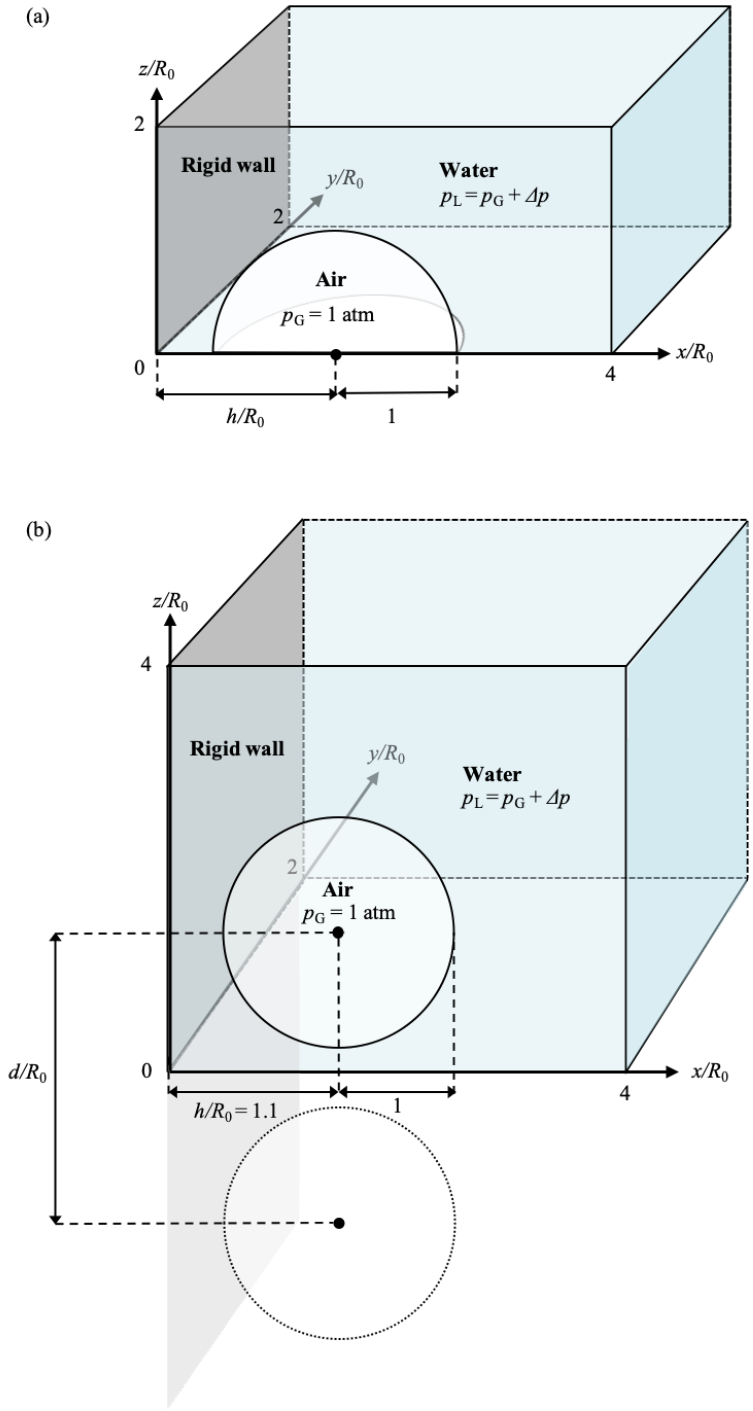

Fig. 4.1: The initial configuration and computational domain of (a) a single spherical air bubble in water and (b) a bubble pair. The (no-slip) rigid wall is set at the y-z plane ($x = 0$) and the bubble centers at standoff h along the x axis. The standoff distance h, the inter-bubble distance d and the pressure increase Δp are computational parameters. Since the problem is axisymmetric about the x axis, the flow in one quadrant of the y-z plane ($y \geq 0$ and $z \geq 0$) is simulated. The length is normalized by the initial radius of the bubble, R_0.

Table 4.2: Physical properties of water (ambient) and air (bubble) at 300 K used in the simulation (Del Grosso & Mader, 1972; Le Métayer & Saurel, 2016).

	Liquid (water, m = L)	Gas (air, m = G)
μ_m [Pa·s]	8.53×10^{-4}	1.85×10^{-5}
c_m [m/s]	1500	344
ρ_m [kg/m^3]	1000	1.18
γ_m [-]	1.09	1.40
$P_{\infty,m}$ [Pa]	3.43×10^8	0
b_m [kg/m^3]	6.61×10^{-4}	0
q_m [J/kg]	-1.17×10^6	2.08×10^6
$C_{\mathrm{v},m}$ [J/(kgK)]	3610	955
κ_m [W/(mK)]	6.15×10^{-1}	2.61×10^{-2}

Table 4.3: Values of characteristic velocity U, the characteristic water-hammer pressure p_{wh}, Rayleigh collapse time t_{c} (Eq. (4.4)), microjet-based Reynolds numbers (Eq. (4.1)) corresponding to different driving pressures Δp for a bubble (100 μm in radius) in water.

Δp [MPa]	$U(=\sqrt{\Delta p/\rho_{\mathrm{L}}})$ [m/s]	$p_{\mathrm{wh}}(=\rho_{\mathrm{L}} c_{\mathrm{L}} U)$ [MPa]	t_{c} [μs]	Re_{jet}
2	45	67.5	2.05	1048
5	71	106.5	1.29	1658
10	100	150.0	0.92	2344

4.2 Physical modeling

4.2.1 Problem description

The initial configuration of a air bubble (of radius R_0) located at distance h from a flat rigid wall ($x = 0$) in semi-infinite compressed water at pressure p_{L} and temperature $T_0 = 300$ K, together with the computational domain, is illustrated in Fig. 4.1(a). The bubble pressure is initially at $p_{\mathrm{G}} = 1$ atm and the bubble collapse is driven by uniform pressure increase $\Delta p = p_{\mathrm{L}} - p_{\mathrm{G}}$ in the surrounding liquid at $t = 0$. The initial (maximum) bubble radius is set at 100 μm for every cases, whose size corresponds to the resonant radius under 28 kHz-sonication when the effect of the wall is considered (Strasberg, 1953). This low-frequency ultrasound matters in degrease cleaning where the drastic cavitation bubble collapse may

become a key factor in the cleaning. When the inertial bubble collapse is so violent, vapor (condensible gas) in the bubble is known to behave like a non-condensible gas (Fujikawa & Akamatsu, 1980; Kobayashi *et al.*, 2018). Thus, the bubble contents is modeled as air (non-condensible, ideal gas) for simplicity, while the actual cavitation bubble is filled with a dissolved gas (air) and vapor. Likewise, mass transfer and vaporization are neglected in the short time scale of our concern. Since we are interested in wall shear flow formation in liquid phase and inertial effect is dominant in the time scale of our concern, we do not consider capillary force (to be demonstrated in the end of the section). On the other hand, heat transfer is taken into account because the collapsing bubble occurs great temperature increasing by the shock emission and the gas compression within the bubble (Beig *et al.*, 2018). Due to the symmetry of the problem, computational domain is reduced for a quarter of a bubble. To be accurate, this problem may suffice axisymmetric assumption, but our single bubble simulation is conducted in three dimensional domain to compare with the result of the two bubbles collapse simulation in the same resolution. As illustrated in Fig. 4.1(b), we then simulate the Rayleigh collapse including the effect of the bubble-bubble interaction. In reality, the cavitation generally involves cloud formation as seen in the work of Hansson *et al.* (1982). For instance, in the ultrasonic cleaning, numerous cavitation bubbles are randomly nucleated forming a cluster and come into play in the cleaning (Yamashita & Ando, 2019 in press). Here, our study focuses the interaction between two bubbles located horizontally to the wall at distance h. Both bubbles have the same radius R_0 because the adjacent bubbles in cloud bubbles are usually similar in size. The inter-bubble distance is denoted by d, which roughly represents the void fraction of the bubble cloud. In this problem setup, because of the plane symmetry at $y = 0$ and $z = 0$, we only simulate a half of bubble and the another bubble is treated as a mirrored bubble. The physical properties of air bubble and surrounding water are set as with the case of single bubble. To qualitatively evaluate the near-wall bubble dynamics and the

wall shear flow formation, we perform parametric studies by changing three parameters:

- Driving pressure Δp
- Standoff distance h
- Inter-bubble distance d

Simulated cases are listed in Table 4.1 and the detailed explanations are as follows.

First, we set at three different driving pressure ($\Delta p = 2, 5, 10$ MPa) as representative examples (Beig *et al.*, 2018). The purpose of this study is to compare the simulated microjet velocity with previous experiments, which is one of the most essential observables for wall shear flow formation. In previous works, researchers have reported that the microjet velocity is scaled by $\sqrt{\Delta p/\rho_{\mathrm{L}}}$ for submillimeter- or millimeter-sized bubbles because these bubbles dominantly collapse in an inertial fashion (Supponen *et al.*, 2016; Beig, 2018). Thereby, the microjet characteristics are only determined by the standoff distance in the case of the near-wall collapse.

The standoff distance h/R_0 ranges from 1.01 to 1.3 which is so close that the microjet can directly impinges the wall. Here, a surface-attached bubble is beyond our scope because the cleaning target is usually hydrophilic in wafer cleaning (e.g., quartz, glass or silicon). Then, we only focus on the wall shear formation through the first collapse and until the secondary collapse because of the scarce experimental knowledge for the latter stage of the collapse in context of the radial spreading flow formation. Since the collapsing bubble often re-expands and collapses again, with forming pancake-like flattened shape or involving fragmentation (Yang *et al.*, 2013; Reuter *et al.*, 2017*b*; Zeng *et al.*, 2018), it is challenging to provide physically reliable simulation results about these phenomena.

The inter-bubble distance d/R_0 ranges from 2.2 to 8 and the standoff distance h/R_0 is then fixed at 1.1. It is known that cavitation bubbles mainly nucleate near the wall due

to the presence of the cavitation sites. Furthermore, the pressure oscillation amplitude is emphasized by the interaction with the wall. Accordingly, the dynamics of the near-wall bubble pair is of great concern to understand the effect of bubble-bubble interactions in the wall shear flow formation.

The Reynolds number for this problem is based on the microjet characteristics:

$$Re_{\mathrm{jet}} = \frac{2\rho_{\mathrm{L}} U \overline{R_{\mathrm{jet}}}}{\mu_{\mathrm{L}}}, \tag{4.1}$$

$$U = \sqrt{\frac{\Delta p}{\rho_{\mathrm{L}}}}, \tag{4.2}$$

$$\overline{R_{\mathrm{jet}}} \approx \frac{R_0}{10}, \tag{4.3}$$

where ρ_{L} and μ_{L} are water density and shear viscosity (see Table 4.2), U is the characteristic velocity and $\overline{R_{\mathrm{jet}}}$ is an approximately averaged microjet radius suggested in the previous work (Ohl *et al.*, 2006*b*). On the other hand, the Weber number $We = 2\rho_{\mathrm{L}}\overline{R_{\mathrm{jet}}}U^2/S$, where S is the surface tension (72 mN/m for water at 300 K), is calculated as 281 at minimum in our parameter space. Thus, the effect of surface tension is not important for the microjet and the wall shear flow formation. The time is normalized by the Rayleigh collapse time (Brennen, 2014).

$$t_{\mathrm{c}} = 0.915\frac{R_0}{U}. \tag{4.4}$$

We note that Eq. (4.4) is inviscid formulation because the time of inertial bubble collapse is barely affected by the liquid viscosity. For the submillimeter-sized bubble of our concern, viscous effects may locally appear near the wall during the event of the bubble collapse. These values of Re_{jet} and t_{c} for the three different Δp are summarized in Table 4.3.

4.2.2 Governing equations for the multi-component fluid flow

To model the flow of our concern, there is a need to consider all compressibility, viscosity and heat conduction of surrounding water (and the inner air). Hence, we solve Navier–Stokes equations for compressible flow consisting of gas and liquid components (with no phase change) in five-equation formulation (Allaire *et al.*, 2002; Perigaud & Saurel, 2005; Murrone & Guillard, 2005) under interfacial pressure and temperature preservation (Beig & Johnsen, 2015). Here, mass conservation (Eqs. (4.5-a) and (4.5-b)) is treated for liquid and gas components separately, while momentum and energy conservation (Eqs. (4.5-c) and (4.5-d)) is formulated for the mixture. The numerically diffused interfaces are represented by void fraction and advected by Eq. (4.5-e).

$$\frac{\partial}{\partial t}\begin{pmatrix} \alpha_{\mathrm{G}}\rho_{\mathrm{G}} \\ \alpha_{\mathrm{L}}\rho_{\mathrm{L}} \\ \rho u_i \\ E \\ \alpha_{\mathrm{L}} \end{pmatrix} + \frac{\partial}{\partial x_j}\begin{pmatrix} \alpha_{\mathrm{G}}\rho_{\mathrm{G}}u_j \\ \alpha_{\mathrm{L}}\rho_{\mathrm{L}}u_j \\ \rho u_i u_j + p\delta_{ij} \\ u_j(E+p) \\ \alpha_{\mathrm{L}}u_j \end{pmatrix} = \frac{\partial}{\partial x_j}\begin{pmatrix} 0 \\ 0 \\ \mathcal{T}_{ij} \\ u_i\mathcal{T}_{ij} - Q_j \\ 0 \end{pmatrix} + \begin{pmatrix} 0 \\ 0 \\ 0 \\ 0 \\ \Gamma\frac{\partial u_j}{\partial x_j} \end{pmatrix}. \quad \begin{matrix} \text{(a)} \\ \text{(b)} \\ \text{(c)} \\ \text{(d)} \\ \text{(e)} \end{matrix} \tag{4.5}$$

Here, α_m is the volume fraction of component m where m = G and L stand, respectively, for the gas phase (air) and liquid phase (water), ρ_m is the density of component m, ρ is the mixture density (to be defined by Eq. (4.11)), indicators i and j denote x-, y-, z-directions, hence, u_i and u_j are three dimensional velocity components (u, v, w), p is thermodynamic pressure, δ_{ij} is the identity tensor, E is total energy (per unit volume), $\mathcal{T}_{ij}$ is the viscous stress tensor (Eq. (4.6)), Q_j is the heat flux calculated by Fourier's law (Eq. (4.7)) and $\Gamma\partial u_j/\partial x_j$ (Eq. (4.8)) is a dilatation-dependent source term that represents the mixture compressibility (Miller & G., 1996; Tiwari *et al.*, 2013; Beig & Johnsen, 2015).

$$\mathcal{T}_{ij} = \mu\left(\frac{\partial u_i}{\partial x_j} + \frac{\partial u_j}{\partial x_i} - \frac{2}{3}\frac{\partial u_k}{\partial x_k}\delta_{ij}\right), \tag{4.6}$$

$$Q_j = -\kappa\frac{\partial T}{\partial x_j}, \tag{4.7}$$

$$\Gamma = \frac{\alpha_{\mathrm{L}}\rho_{\mathrm{G}}c_{\mathrm{G}}^2}{\alpha_{\mathrm{L}}\rho_{\mathrm{G}}c_{\mathrm{G}}^2 + \alpha_{\mathrm{G}}\rho_{\mathrm{L}}c_{\mathrm{L}}^2}, \tag{4.8}$$

where μ is the mixture viscosity (to be defined by Eq. (4.11)), κ is the mixture heat conductivity (to be defined by Eq. (4.11)) and c_m is the speed of sound in component m. In the formulation of viscous stress tensor (Eq. (4.6)), bulk viscosity is neglected according to Stokes' hypothesis, for our main target is to evaluate wall shear generation associated with the bubble collapse. The dilatational source term described in Eqs. (4.5-e) and (4.8) is classically neglected because it is not important for weak compressible fluid and it may violate the robustness of the simulation (Beig & Johnsen, 2015). However, it is known that this source term crucially comes into play in the case of compressible multicomponent flow including drastic volume changes like bubble oscillation (the contribution of this term is also confirmed in Section 4.3.3) (Tiwari *et al.*, 2013; Beig & Johnsen, 2015).

Thermodynamic pressure p and temperature T are given by the Noble-Able stiffened gas (NASG) equations of state (Le Métayer & Saurel, 2016):

$$E - \frac{1}{2}\rho u_i u_i - \rho q = \frac{p(1-\rho b)}{\gamma - 1} + \frac{\gamma P_\infty (1-\rho b)}{\gamma - 1} = \rho C_{\mathrm{v}} T + P_\infty (1-\rho b), \tag{4.9}$$

where γ, P_∞, q, b and C_{v} are thermodynamic properties for the mixture formulation and these values we use are listed in Table 4.2. In comparison to the original stiffened gas equation of state, the NASG equation of state is obeyed by both liquid and gas for wide ranges of temperature (Le Métayer & Saurel, 2016). Here, we should note that our simulation still neglect the temperature dependence in these thermodynamic properties including shear viscosity μ because our great interest is liquid flow field near a rigid wall where the temperature rise is assumed to be relatively small in comparison to the vicinity of the bubble surface. According to a previous simulation of Beig *et al.* (2018), which investigates the temperature increase during the bubble collapse near a wall, the bubble collapse accompanies a great temperature increase (up to $O(100\ \mathrm{K}) + T_0$, instantaneously) at gas phase within the bubble. However, it is also demonstrated that the collapsing bubble

hardly increases the surrounding water temperature. In addition, the Prandtl number for water is calculated as $Pr = \mu_{\mathrm{L}} C_{\mathrm{v,L}} / \kappa_{\mathrm{L}} = 5$ from Table 4.2. That is, heat transfer from the inner bubble to the surrounding water is not fully achieved during the short time scale of the wall shear flow formation after the microjet impingement. Therefore, the assumption of constant thermodynamic properties is reasonable when we investigate the wall shear flow formation in water.

As with Section 2.2.2, mixture quantities for the current physical modeling are summarized as follows:

$$\alpha_{\mathrm{G}} + \alpha_{\mathrm{L}} = 1, \tag{4.10}$$

$$\phi = \alpha_{\mathrm{G}} \phi_{\mathrm{G}} + \alpha_{\mathrm{L}} \phi_{\mathrm{L}}, \tag{4.11}$$

$$\phi = \begin{pmatrix} \rho & \mu & \kappa & \gamma & P_\infty & q & b & C_{\mathrm{v}} \end{pmatrix}^{\mathrm{T}}, \tag{4.12}$$

$$\phi_m = \begin{pmatrix} \rho_m & \mu_m & \kappa_m & \gamma_m & P_{\infty,m} & q_m & b_m & C_{\mathrm{v},m} \end{pmatrix}^{\mathrm{T}}, \tag{4.13}$$

where ϕ is a vector composed of respective mixture physical properties in Eq. (4.5) to (4.9) and ϕ_m is a vector composed of respective physical properties of water (m = L) and air (m = G) (see Table 4.2).

4.3 Numerical modeling

4.3.1 Spatial discretization and temporal integration

The numerical method we use is based on the solution-adaptive, shock-interface capturing method proposed by Beig & Johnsen (2015), which can automatically adjust optimum scheme for computation of numerical fluxes and thereby achieves both high-resolution computation and reduction of simulation time. For spatial discretization, a fifth-order finite-volume WENO scheme with the HLL approximate Riemann solver (Harten *et al.*, 1983) is adopted only for discontinuous regions (i.e., material interface and shock front). On the other hand, the fourth-order central differencing scheme is adopted for smooth regions. The detection of discontinuities is carried out by calculating a discontinuity sensor function at all computational cells (Henry de Frahan *et al.*, 2015). The time integration is handled by a third-order, total variation diminishing Runge–Kutta scheme (Gottlieb & Shu, 1998) with sufficiently small Courant number (< 0.2) (Eq. (2.13)) and diffusion numbers for viscosity D_{V} and temperature D_{T},

$$D_{\mathrm{V}} = \Delta t \max_{i,j,k} \left(\frac{\mu_{i,j,k}}{\rho \Delta x_i^2}, \frac{\mu_{i,j,k}}{\rho \Delta y_j^2}, \frac{\mu_{i,j,k}}{\rho \Delta z_k^2} \right) < 5.6 \times 10^{-2}, \tag{4.14}$$

$$D_{\mathrm{T}} = \Delta t \max_{i,j,k} \left(\frac{\kappa_{i,j,k}}{\rho C_{\mathrm{v}} \Delta x_i^2}, \frac{\kappa_{i,j,k}}{\rho C_{\mathrm{v}} \Delta y_j^2}, \frac{\kappa_{i,j,k}}{\rho C_{\mathrm{v}} \Delta z_k^2} \right) < 1.1 \times 10^{-2}. \tag{4.15}$$

Finally, we note that the current numerical implementation for viscous flow problem is preliminary verified by solving Stokes' first problem as demonstrated in Section 3.3.3. Furthermore, the validity of the solution-adaptive, high-resolution scheme for multicomponent flow is demonstrated by single spherical bubble collapse simulation in free field in Section 4.3.3.

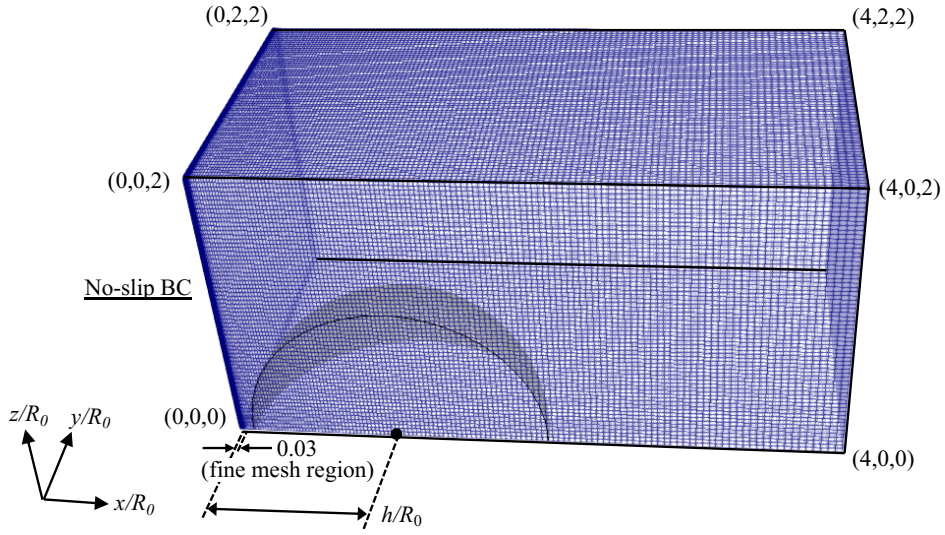

Fig. 4.2: Computational grids in which initial configuration of the single bubble near a rigid wall for the case of $h/R_0 = 1.1$ is depicted by isosurface of $\alpha_L = \alpha_G = 0.5$. No-slip boundary conditions (BCs) are applied on y-z plane ($x = 0$) as a rigid wall. Reflecting BCs are applied on x-z plane ($y = 0$) and x-y plane ($z = 0$) because of the symmetry of the problem, while non-reflecting BCs are applied on the other planes. Refined computational grids are distributed near the wall in $0 \leq x/R_0 \leq 0.03$.

4.3.2 Computational domain

The computational grid with the initial configuration of the single bubble location for the case of $h/R_0 = 1.1$ is presented in Fig. 4.2. Grid stretching across near the rigid surface ($x = 0$) is applied in order to correctly resolve the wall shear flow, while the both grids in y- and z-directions are uniform. Here, we show the grid whose resolution is 250 points in $0 \leq x/R_0 \leq 0.03$. The cell Reynolds number of this resolution, which quantifies the effect of spurious numerical viscosity, is $Re_{\mathrm{cell}} = \rho_{\mathrm{L}} U \Delta x/\mu_{\mathrm{L}} = 1.2$ near the wall for the case of $\Delta p = 5$ MPa. Therefore, it is sufficient to resolve near-wall viscous flows correctly (Vreugdenhil, 1982; Thompson *et al.*, 1985). On the other hand, in the bulk region ($x/R_0 > 0.03$), 64 grid points are uniformly distributed. For the cases of different bubble-wall distance and the cases of two bubbles, we use the same grid resolution as illustrated in Fig. 4.2.

Due to the symmetry of the problem as mentioned in Section 4.2.1, we apply the reflecting boundary conditions (BCs) along both planes of $y = 0$ and $z = 0$. A rigid wall at $x = 0$ is treated as no-slip BCs. Since we only consider the cases that bubble is initially detached, any slip models are not needed to physically regularize the velocity and stress singularities at viscous boundary layer as discussed in Chapter 3. For evaluation of the wall shear stress,

$$\boldsymbol{\tau}_{\mathrm{wall}} = \begin{pmatrix} \tau_y(y, z, t; h/R_0, \Delta p) \\ \tau_z(y, z, t; h/R_0, \Delta p) \end{pmatrix} = \begin{pmatrix} \mathcal{T}_{xy}(0, y, z, t; h/R_0, \Delta p) \\ \mathcal{T}_{xz}(0, y, z, t; h/R_0, \Delta p) \end{pmatrix}, \tag{4.16}$$

respective velocity gradients in Eq. (4.6) is calculated by a third-order one-sided difference. At the rest of far-field boundaries, we apply nonreflecting BCs of Thompson type (Thompson, 1987).

4.3.3 Verification: Rayleigh collapse in free field

To see whether the current numerical model can resolve the multicomponent flow, we numerically solve the collapse of an air bubble in infinite water driven by sudden pressure

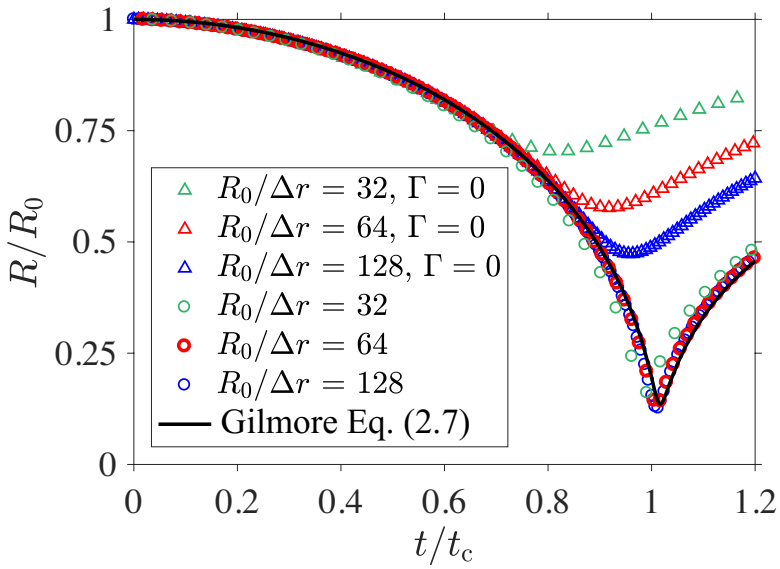

Fig. 4.3: Temporal evolution of volume equivalent radius of a spherically collapsing bubble in water (Δp = 5 MPa). The triangle markers and the circle markers correspond to the simulation results with and without the assumption of $\Gamma = 0$ in Eq. (4.5-e) for three different grid resolutions. The black solid line depicts of the analytical solution of the Gilmore type.

rise, known as Rayleigh collapse (Rayleigh, 1917). To be consistent with our main simulation, physical properties are set at the same as listed in Table 4.2. Accordingly, initial bubble radius is set at $R_0 = 100$ μm and the driving pressure is set at $\Delta p = 5$ MPa, for instance. As mentioned in Section 4.2.2, we also compare two different advection equations for volume fraction: one includes the dilatational source term $\Gamma \partial u_j / \partial x_j$ (seen in Eqs. (4.5-e) and (4.8)) and another does not. For numerical setup, we use the three dimensional, uniform Cartesian coordinates and simulate with three different grid resolutions: 32, 64 and 128 grid points per initial bubble radius R_0.

Figure 4.3 shows the simulation results of the time evolution of the volume-equivalent bubble radius:

$$\frac{R}{R_0} = \left(\frac{V}{V_0} \right)^{\frac{1}{3}}, \quad V(t) = \iiint \alpha_{\mathrm{G}}(x, y, z, t) \mathrm{d}x\mathrm{d}y\mathrm{d}z, \tag{4.17}$$

where V is the bubble volume. The time is normalized by the Rayleigh collapse time t_{c} Eq. (4.4). The simulation results are compared with the solution of the Gilmore Eqs. (2.7), which can consider the liquid compressibility (Gilmore, 1952). The inner gas of the bubble is then assumed to be adiabatic. Here, we find good agreement between the analytical solution and the results including the source term, while the other results leads serious damping without the source term. Moreover, the grid convergence is fairly assured in the case of 64 grid points per R_0, which is used in our main simulation of the nonspherical bubble collapse for the bulk region.

4.4 Collapse of a single bubble near a rigid wall

First, big picture of the simulation results for single bubble collapse near a rigid wall is presented in Fig. 4.4. The temporal snapshot of the velocity magnitude, wall shear stress and pressure distributions on the rigid wall (plane of $x = 0$) and wall-normal middle plane of the bubble (plane of $y = 0$) are presented for the case of $(h/R_0, \Delta p) = (1.1, 5$ MPa) as

a representative. The frame (a) corresponds to the initial condition of this problem. The frame (b) shows the process of bubble shrinking driven by the pressure gap Δp between the air bubble and surrounding water. As illustrated by vectors in velocity and wall shear stress plot, the bubble shrinking gives rise to the focusing of the liquid flow on the bubble center. Then, the presence of the wall plays a key role for the nonspherical bubble collapse because it violates the spherical symmetry of the flow around the bubble in contrast to the case of the Rayleigh collapse in free field (introduced in Section 4.3). Since the presence of the wall corresponds to the displacement of the flow, the liquid velocity at the distal side of the wall relatively increases. Finally, this local acceleration of the flow results in formation of the reentrant, microjet as shown in the frame (c).

The normalized jet velocity is increasing over the characteristic velocity of the spherical collapse U (Eq. (4.2)). This result is consistent with previous studies (Supponen *et al.*, 2016; Beig, 2018). The quantitative agreement is confirmed in Section 4.4.1.

The evolution of wall shear stress, τ_{wall} (Eq. (4.16)), shows that generation of wall shear flow falls into two stages: shock emission of the bubble collapse and the microjet impact. The maximum wall shear stress is obviously seen in the stage of the jet impact. As deduced in Section 4.2.1, the flow becomes axisymmetric and the x-axis corresponds to the axis of symmetry (i.e., $\tau_y(y, 0, t) \approx \tau_z(0, z, t)$). To understand the formation of wall shear flow of our great interest, near-wall velocity profiles is first presented in Section 4.4.2. After the investigation of the boundary layer development, the mechanism of wall shear stress development over time and space is demonstrated in Section 4.4.3. On the other hand, the wall shear stress is normalized by a characteristic value τ_{c}, which is also explained in the same section.

The simulated pressure rising is also reasonable because its evolution reaches the same order of the water-hammer pressure defined by the characteristic velocity $p_{\mathrm{wh}} = \rho_{\mathrm{L}} c_{\mathrm{L}} U$. Since the wall pressure evolution is fully discussed in previous experiments and simula-

tions for understanding the surface erosion and for biomedical applications (Johnsen & Colonius, 2006; Coralic & Colonius, 2014; Tiwari *et al.*, 2015; Chahine & Hsiao, 2015), detailed discussion of the wall pressure is beyond the our scope.

4.4.1 Speed of the microjet

The microjet speed of the collapsing bubble is an important parameter to understand the subsequent wall shear flow formations. Moreover, it is usually discussed in experimental studies because of the straightforwardness in its measurement. Here, we quantify the maximum jet speed as a function of standoff distance h/R_0. The maximum speed is defined as the maximum value at a point over time where it suffices $\alpha_\mathrm{L} = \alpha_\mathrm{G} = 0.5$ on x-axis:

$$u_\mathrm{jet} = \max_{t/t_\mathrm{c}} |u(x_i, 0, 0, t)|\,, \quad \text{where } \alpha_\mathrm{L}(x_i, 0, 0, t) = \alpha_\mathrm{G}(x_i, 0, 0, t) = 0.5. \tag{4.18}$$

Simulation results are compared with previous experimental data of the laser-induced cavitation bubble collapse near a rigid/free surface (Philipp & Lauterborn, 1998; Brujan *et al.*, 2002; Supponen *et al.*, 2016). Supponen *et al.* (2016) reports that the jet speed is scaled by U and that only depends on the standoff distance for the case of bubble collapse near a rigid wall. This scaling law may be obvious because the nonspherical bubble collapse is only caused by geometric conditions like the presence of the wall or free surface.

Simulation results with previous experimental data are summarized in Fig. 4.5. The difference of the driving pressure is found to be scaled by the characteristic speed U. In comparison to the experimental data, the simulated jet speed takes the same order values and the similar trend is seen in its dependency on the standoff distance: the further standoff distance gives rise to the higher microjet speed. Regarding the fact that numerical results slightly overtakes the experimental data, we note that our problem description (Rayleigh collapse) is not exactly the same phenomena as the laser-induced bubble collapse. While

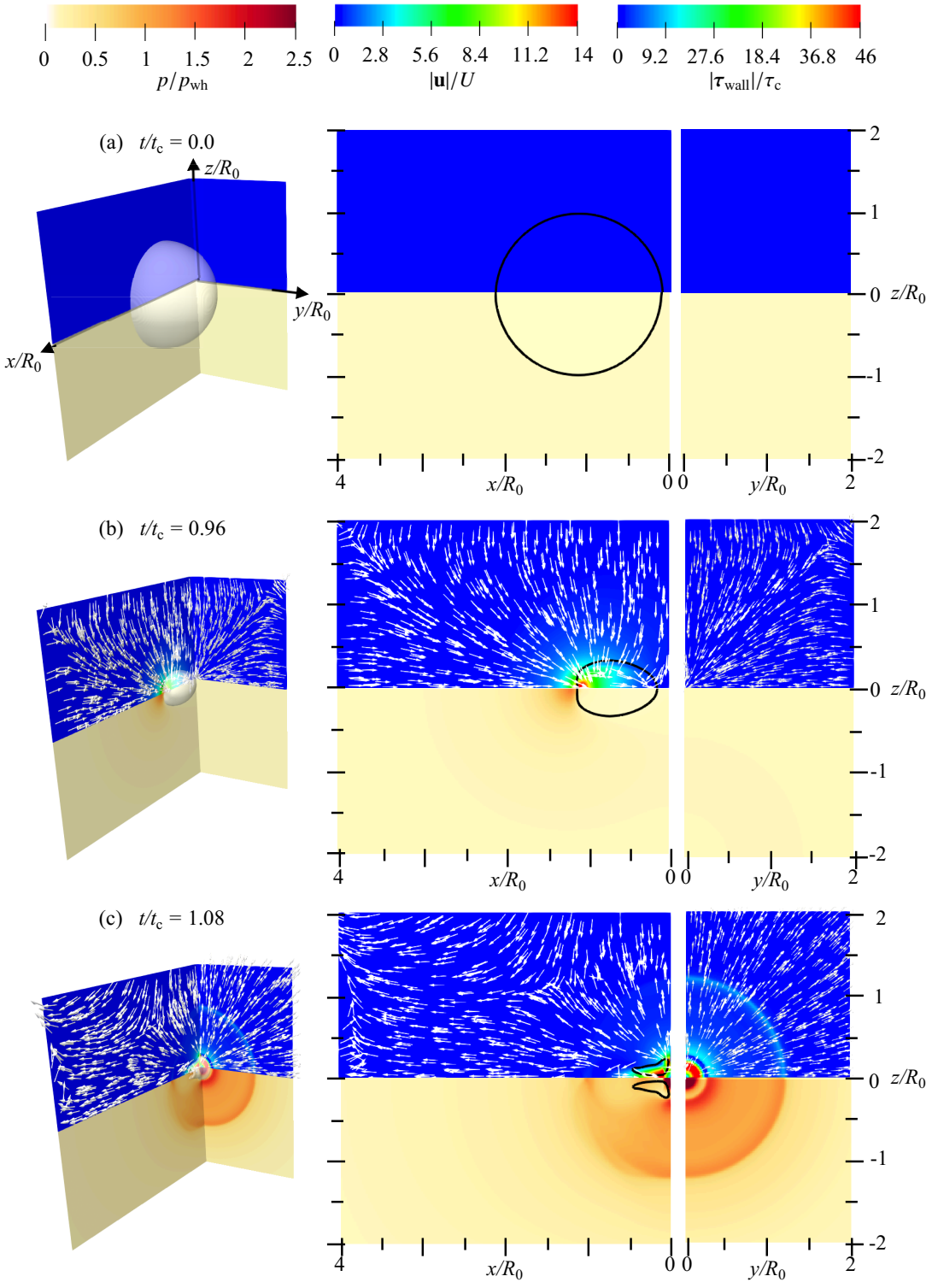

Fig. 4.4: Snapshots of the bubble collapse near a rigid wall at representative times (a) to (c) for the case of $(h/R_0, \Delta p)$ = (1.1, 5 MPa), plotting the distributions of the velocity magnitude with vector (upper middle plane), the wall shear stress magnitude with vector (upper wall plane) the pressure (lower middle plane and wall plane). The nominal positions of air-water interfaces (α_L = α_G = 0.5) is depicted as black lines in middle plane and white surface in the three-dimensional view listed left.

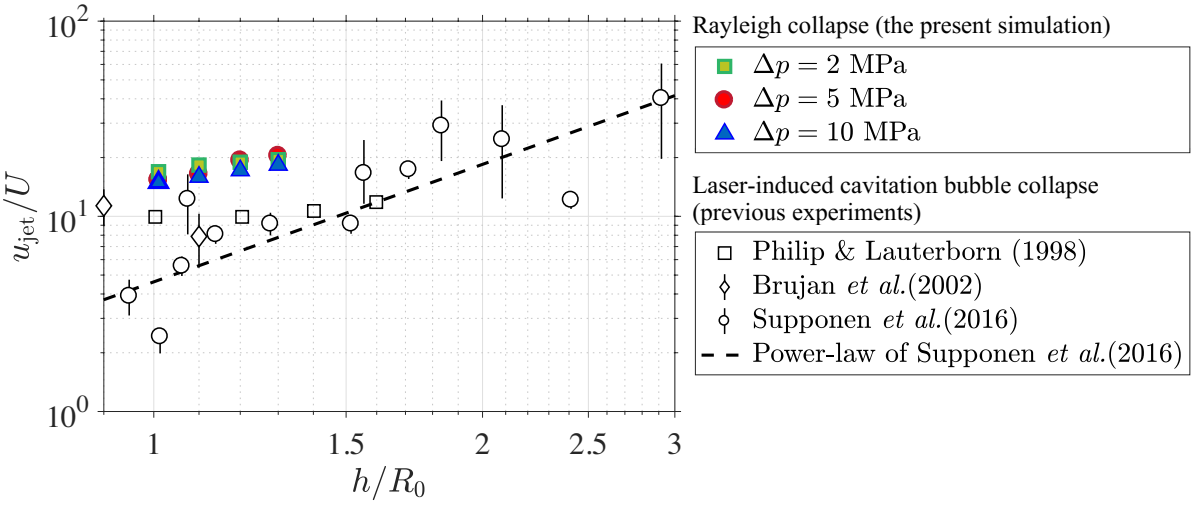

Fig. 4.5: Maximum microjet velocity of the collapsing bubbles, Eq. (4.18), as a function of the standoff distance h/R_0. Results for different driving pressure Δp are plotted. Black markers depict previous experimental measurement of the maximum jet velocity of the laser-induced bubbles by Philipp & Lauterborn (1998); Brujan *et al.* (2002); Supponen *et al.* (2016). Dashed black line depicts the power law fitting, $4.6(h/R_0)^2$, proposed by Supponen *et al.* (2016).

the far-field pressure in the actual experiment of the laser cavitation is atmospheric, the Rayleigh collapse problem assumes high pressure rise in infinite surrounding water. That is, inertial forces that drives bubble collapse becomes larger than the experiment. Furthermore, experiments may underestimates the maximum velocity due to the limited frames per second and pixel resolutions of high-speed cameras.

4.4.2 Shear flow formation

To investigate the shear flow in details, we plot the near-wall horizontal velocity w at several times in Fig. 4.6. Results are shown for $\Delta p = 5$ MPa and four different standoff distances ($h/R_0 = 1.01$, 1.1, 1.2 and 1.3). The shear flow is probed at two positions ($z/R_0 = 0.05$ and 0.33), respectively. Here, boundary layer development is observed in every cases. These results also indicates the grid resolution is sufficient enough for the boundary layer, for the boundary layer is resolved by tens of grid points. While the

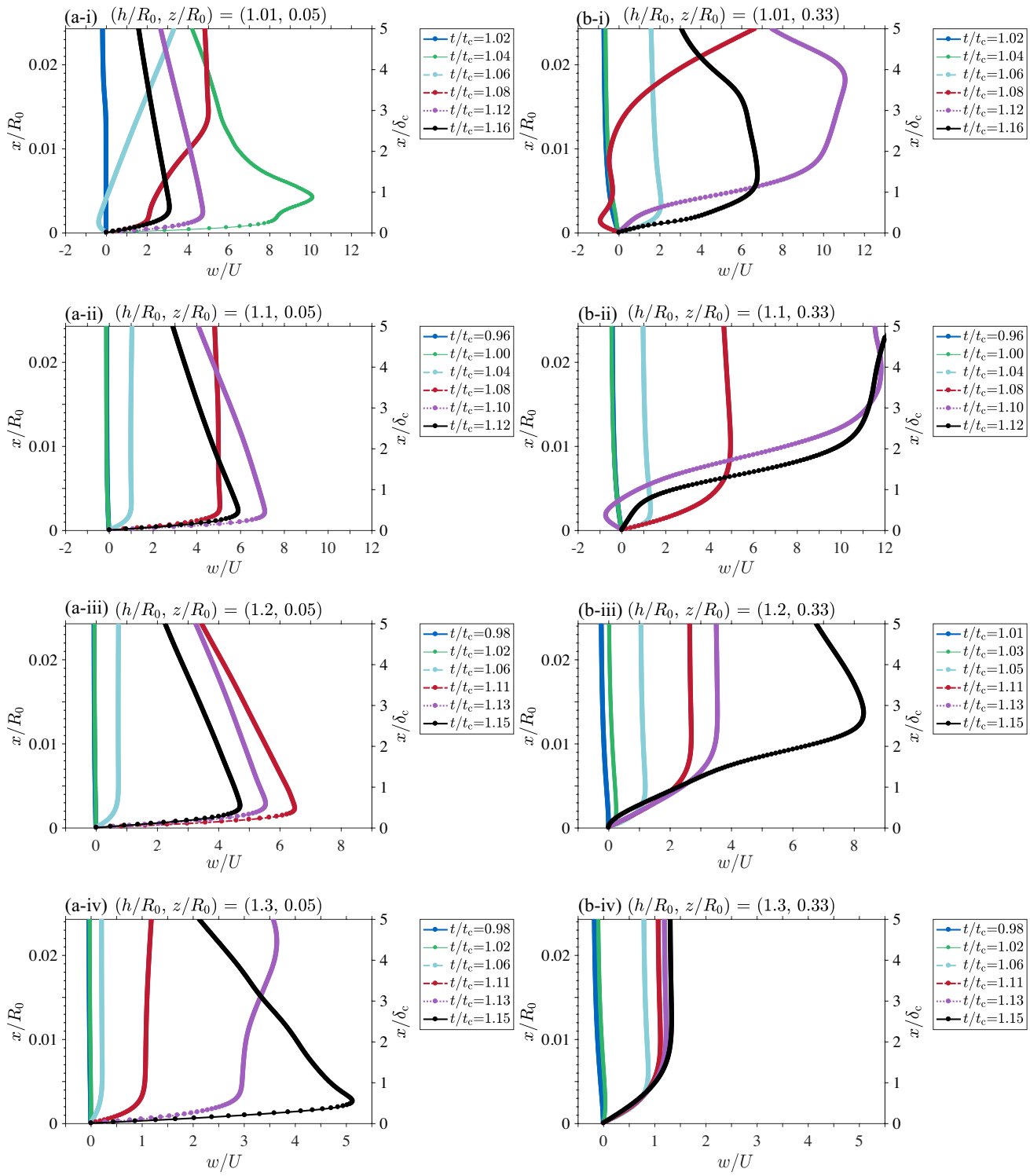

Fig. 4.6: Temporal evolution of the near-wall z-velocity profiles at (a) $z/R_0 = 0.05$ and (b) $z/R_0 = 0.33$. The x coordinates in the left-hand and right-hand sides are normalized by initial bubble radius R_0 and characteristic boundary layer thickness δ_c, respectively. The results for four different standoff distance are presented: (i) $h/R_0 = 1.01$, (ii) $h/R_0 = 1.1$, (iii) $h/R_0 = 1.2$, (iv) $h/R_0 = 1.3$.

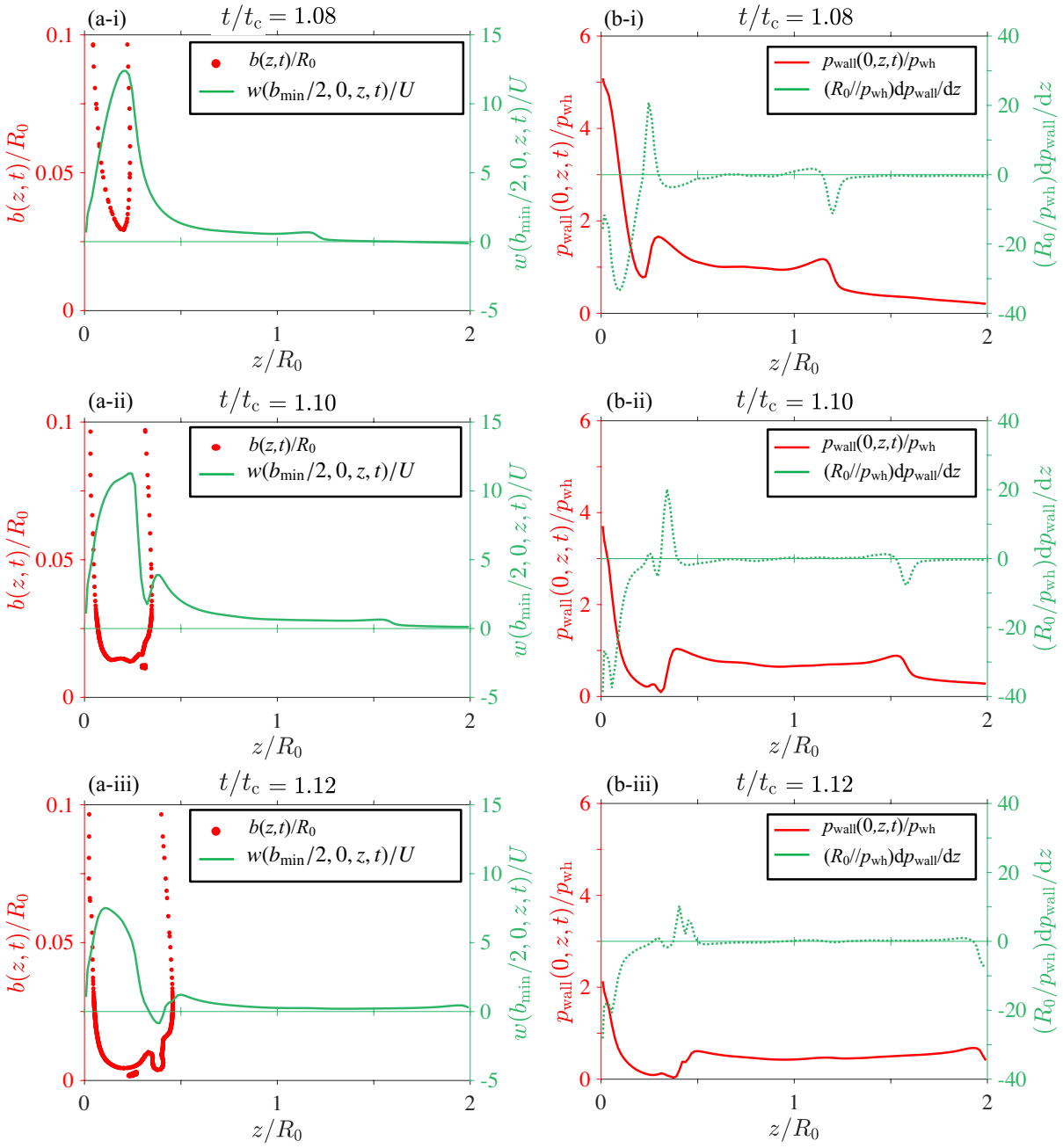

Fig. 4.7: (a) The (nominal) air-water interface profiles on the plane of $y = 0$, $b(z,t)$, defined by $\alpha_G = \alpha_L = 0.5$ (the left vertical axis) and the z-velocity distributions $w(b_{min}/2, 0, z, t)$ (the right vertical axis). (b) Distributions of the wall pressure $p_{wall}(0,z,t)$ (the left vertical axis) and the pressure gradient dp_{wall}/dz (the right vertical axis). The pressure is normalized by the water hammer pressure, $p_{wh} = \rho_L c_L U$ (see Table 4.3). Results are shown at representative times (i) to (iii) for the case of $(h/R_0, \Delta p) = (1.1, 5\ \text{MPa})$.

vertical axis of wall-normal distance is normalized by initial bubble radius on left-hand side, the right-hand side is normalized by the characteristic boundary layer thickness as with Section 3.6.2:

$$\delta_{\mathrm{c}} = \frac{2\overline{R_{\mathrm{jet}}}}{\sqrt{Re_{\mathrm{jet}}}}. \tag{4.19}$$

The values of δ_{c} for several Re_{jet} is listed in Table 4.4.

First, as seen in velocity profiles near the bubble center ($z/R_0 = 0.05$), temporal evolution of the boundary layer development is clearly observed in the latter times. On the other hand, the fluid is found to be almost static before the timing of the bubble collapse (plotted as blue and green solid line in Fig. 4.6). As with the study of the droplet impact, the boundary layer thickness measured near the bubble center tends to approach the characteristic value δ_{c}. It is interesting that the shear flow velocity outside the boundary layer tends to decrease as the standoff distance becomes further, on the contrary to the trend of the maximum jet speed (see previous Section 4.4.1). However, it is obvious because the microjet speed is damped during the travel to the wall. That is, this velocity damping can overwhelm the effect of the velocity increasing due to taking a longer standoff distance. Focusing on the temporal evolutions of the velocity outside the boundary layer, it takes a peak value at a particular time and then starts to decelerate. Namely, it is important to investigate the wall shear flow formation in short period after the jet impact, which is similar to the study of the droplet impact. Judging from these features of the wall shear flow, the microjet impact of the collapsing bubble may have the similar features to the droplet impact in terms of the wall shear flow formation. In this sense, the standoff distance of the bubble plays a similar role with the water film thickness in the study of droplet impact against a wet wall.

Second, at the further probe point ($z/R_0 = 0.33$), it is obvious the boundary layer becomes thicker for respective cases. More importantly, the shear flow is found to be separated for cases (b-i) and (b-ii) in Fig. 4.6. On the other hand, such flow separation

Table 4.4: Values of characteristic boundary layer thickness δ_c (Eq. (4.19)) and wall shear stress τ_c (Eq. (4.20)) corresponding to different driving pressures Δp for a bubble (100 μm in radius) in water.

Re_{jet}	δ_c [μm]	τ_c [kPa]
1048	0.62	62
1658	0.50	123
2344	0.41	206

does not occur in cases of longer standoff distance ((b-iii) and (b-iv)). One possible scenario can be explained by the relation between the near-wall velocity and the pressure profiles on the wall according to the discussion in Section 3.6.2. Figure 4.7 (a) shows the (nominal) air-water interface positions ($\alpha_G = \alpha_L = 0.5$), which illustrates the breadth between the bubble interface and the wall, at several times for the case of (h/R_0, Δp) = (1.1, 5 MPa) as a representative. In this figure, we overlay the horizontal near-wall velocity to the wall $w(b_{min}/2, 0, z, t)$, as a representative velocity between the bubble interface and the wall, where b_{min} denotes the minimum breadth (in the x direction) from the wall to the bubble interface. Accordingly, the flow is dramatically decelerated through the bubble location, while the flow is accelerated below the bubble. As a result of the flow deceleration, a remarkable adverse pressure gradient (> 0) arises around $z/R_0 = 0.4$ at respective time frames in Fig. 4.7 (b). This flow deceleration may be related to the volume conservation of the (effectively incompressible) liquid flow: namely, the near-wall flow passage consisted by the air-water interface may have a similar feature with the converging-diverging nozzle. That is, the flow reaches the maximal velocity at the throat (with b_{min}) and is decelerated in the diverging area (after the throat passage). The flow deceleration is augmented by taking the shorter standoff distance (e.g., $h/R_0 < 1.1$ from our study). Therefore, from a viewpoint of flow separation, we find the analogy between the droplet impact and the bubble collapse.

4.4.3 Wall shear stress evolution

The evolution of the wall shear flow is assessed here quantitatively by plotting the wall shear stress. According to the same manner in Section 3.6.2, the wall shear stress is normalized by the characteristic wall shear stress:

$$\tau_{\mathrm{c}} = \mu_{\mathrm{L}} \frac{U}{\delta_{\mathrm{c}}}. \tag{4.20}$$

The value of τ_{c} for several Re_{jet} is listed in Table 4.4. In Fig. 4.8, we plot the spatiotemporal evolution of the wall shear stress on z-axis $\tau_z(0, z, t)$ for $\Delta p = 5$ MPa and four different standoff distances h. As common features for four cases, streak of the wall shear stress appeared due to the shock emission from the collapsing bubble. Subsequently, the strong wall shear flow is generated near the bubble center due to the miro-jet impingement. It is obvious that the wall shear stress becomes stronger as the bubble locates with shorter standoff distance. On the other hand, the shock-induced shear stress appears earlier by taking the further standoff distance. That is, the collapse time is found to be reduced in this case as well as the jet speed increases shown in Fig. 4.5. Moreover, the flow separation is only found in the cases of relatively short h.

As with Eq. (3.26), the maximum wall shear stress encountered at each position on z-axis ($x = y = 0$) is defined by

$$\tau_{\max}(z; h/R_0, \Delta p) = \max_{t/t_{\mathrm{c}}} \left(\tau_z(0, z, t; h/R_0, \Delta p) \right), \tag{4.21}$$

and its distribution is plotted as a function of the distance z for $\Delta p = 2$, 5, 10 MPa and $h/R_0 = 1.1$, respectively in Fig. 4.9. In comparison to the droplet impact, bubble collapse is more highly compressible phenomenon such that it accompanies the shock emission. As observed the shock-induced wall shear flow, effects of compressibility is no longer trivial for the fluid flow. Therefore, the Reynolds number-based scaling cannot fully characterize the flow of our concern. Nevertheless, Fig. 4.9 is still instructive to

show two features of this result. First, the dominant factor of the shear flow formation is found to be different depending on the distance z: while the jet-induced shear stress is dominant near the bubble center ($z/R_0 < 0.3$), shock-induced shear stress is dominant away from the center ($z/R_0 > 0.3$). Second, focusing on the jet-induced shear flow at $0.1 < z/R_0 < 0.3$, the spatial attenuation rate of the $\tau_{\max}$ fairly agrees with the functional dependence of the Glauert's solution on the wall distance ($\tau_{\max} \propto z^{-2.75}$) (Glauert, 1956). Hence, the simulated maximum wall shear stress distribution on the wall have a similar trend with the experiment of Dijkink & Ohl (2008).

Lastly, to comprehensively evaluate effects of the standoff distance on the wall shear stress evolution, the peak value of $\tau_{\max}(z)$ are found for respective cases (denoted as $\tau_{\max}(z_{\max})$) and summarized in Fig. 4.10 as a function of the standoff distance h. Accordingly, the Δp-dependence on wall shear stress is found to be relatively small. More importantly, the $\tau_{\max}(z_{\max})$ declines logarithmically with increasing of h. This attenuation is found to be modeled by a power law fitting of $\tau_{\text{fit}} = 85.6(h/R_0)^{-6}$. This power law is much steeper than previous scalings for other observables proposed by Supponen *et al.* (2016) (power law modeling of jet speed, impact time, bubble volume and bubble displacement are carried out as a function of anisotropy parameter, which corresponds to the length of the standoff distance for the case of bubble collapse near a surface).

4.5 Collapse of a bubble pair near a rigid wall

Finally, the effects of bubble-bubble interaction is evaluated in terms of wall shear flow formation. The big pictures of the collapse of a bubble pair near a rigid wall are presented for the cases of two different distance between bubble pair $d/R_0 = 2.5$ and 8 in Figs. 4.11 and 4.12. The frame (a) in Figs. 4.11 and 4.12 corresponds to the initial condition of this problem. The frame (b) in Fig. 4.11 shows the process of bubble shrinking, and we note that the direction of the microjet formation is tilted towards the midpoint of two bubbles.

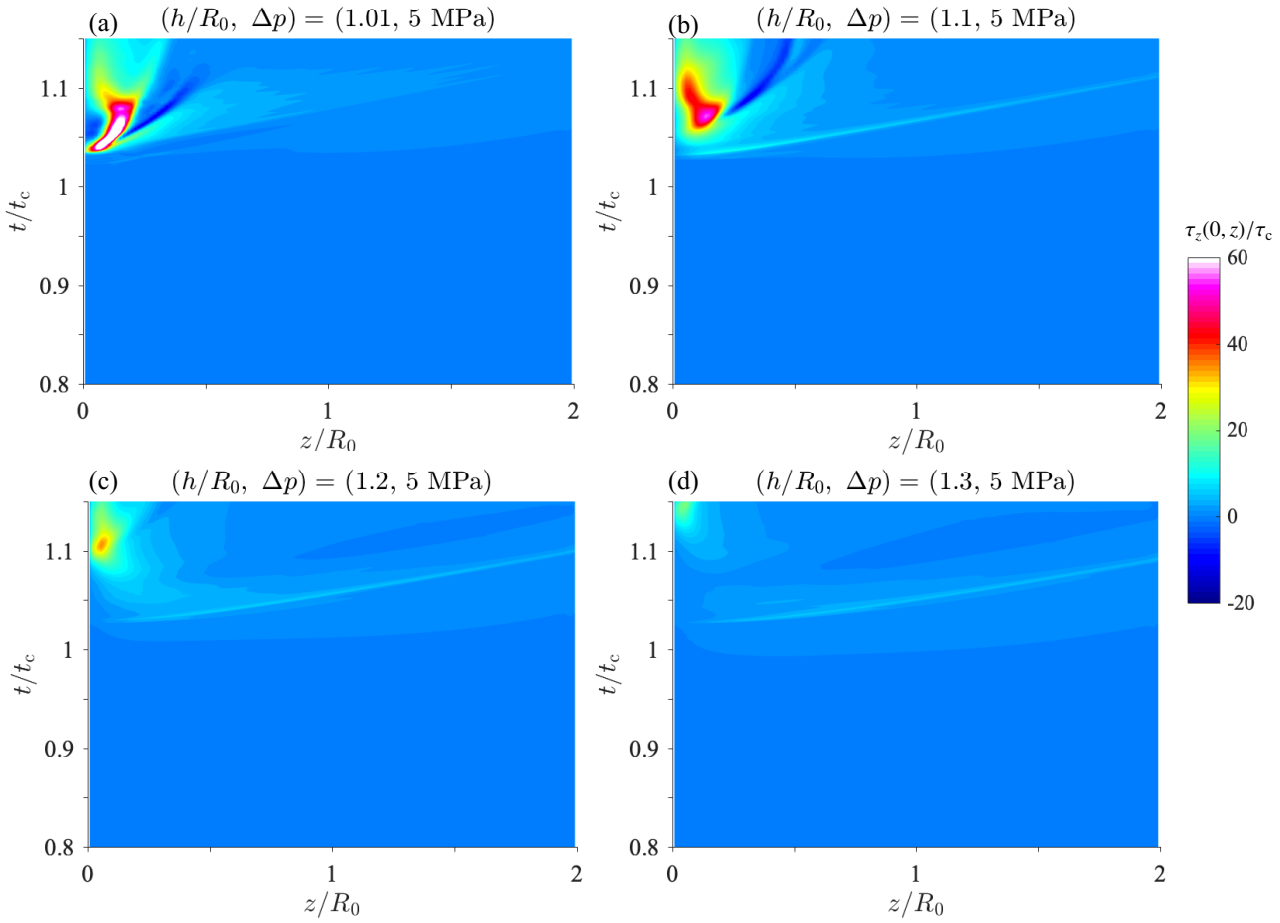

Fig. 4.8: Spatiotemporal evolution of the wall shear stress on z-axis ($x = y = 0$) for cases of $\Delta p = 5$ MPa. The results for four different standoff distance are presented: (a) $h/R_0 = 1.01$, (b) $h/R_0 = 1.1$, (c) $h/R_0 = 1.2$, (d) $h/R_0 = 1.3$.

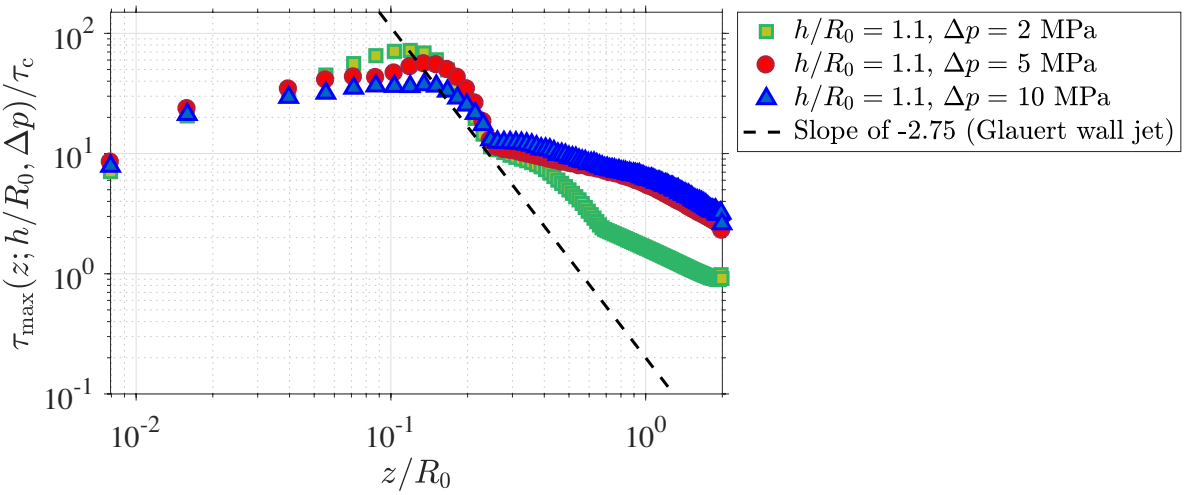

Fig. 4.9: Distributions of the maximum wall shear stress encountered at each z-position on $x = y = 0$, Eq. (4.21), for $h/R_0 = 1.1$ and different driving pressure Δp.

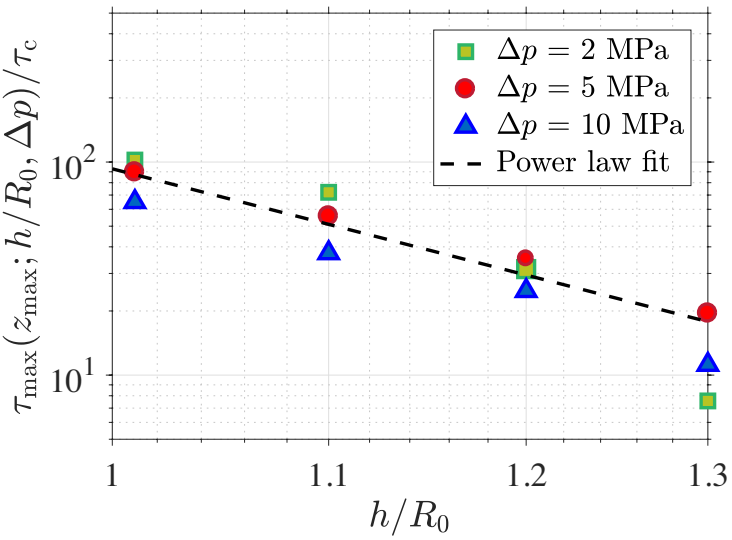

Fig. 4.10: The maximum wall shear stress defined over both time and space as a function of the standoff distance h/R_0. Results for different driving pressure Δp are plotted. The vertical axis is normalized by the characteristic wall shear stress τ_c (Eq. (4.20)) (see Table 4.4). The simulation data are fitted by a power law of $85.6(h/R_0)^{-6}$.

This behavior is also observed in the experiment of the collapse of a surface-attached bubble pair by Yamashita & Ando (2019 in press). Since the nonspherical bubble collapse is occurred only by the geometric conditions like the presence of the wall, the presence of the neighbor bubble also affects the microjet formation. Besides the jet direction, the resulting wall shear stress is entirely suppressed. One possible scenario may be related to the effect of the flow stagnation at the midpoint of two bubbles, for the jet impinges each other at the midpoint. The frame (c) in Fig. 4.11 illustrates that the velocity magnitude at the midpoint is still zero, though the bubble has already formed the microjet. On the other hand, the result in Fig. 4.12 is more similar to the case of single bubble. Distributions of the wall shear stress and wall pressure looks more point-symmetric than the result in Fig. 4.11. Here, we first assess the effects of the bubble-bubble interaction in terms of the jet angle and the jet velocity in Section 4.5.1. Thereafter, wall shear flow evolution and the suppression effects are evaluated in Section 4.5.2.

4.5.1 Velocity and angle of the microjet

To quantify the the effect of bubble-bubble interaction in terms of the bubble morphologies, the velocity magnitude and the jet angle are evaluated for the case of $(h/R_0, \Delta p) =$ (1.1, 5 MPa), by changing the inter-bubble distance d/R_0 from 2.2 to 8.0. The jet angle θ is examined by the velocity vector component, $\theta = \tan^{-1}\left(w_{\mathrm{jet}}/u_{\mathrm{jet}}\right)$, at the point of the jet tip (found by Eq. (4.18)) on the middle plane of two bubbles (plane of $y = 0$). Since the jet angle is slightly time dependent, we choose the timing for the angle definition just before the microjet piercing in the distal side of the bubble surface. Figure 4.13 illustrates the velocity magnitude, bubble surface ($\alpha_{\mathrm{L}} = \alpha_{\mathrm{L}} = 0.5$) and the jet directions at the representative times. Here, we found the jet speed increases and the angle approaches to zero as the distance increases. These results are summarized in Fig. 4.14 as a function of the distance d. To compare with the single bubble case, the jet speed is normalized by u_{jet}

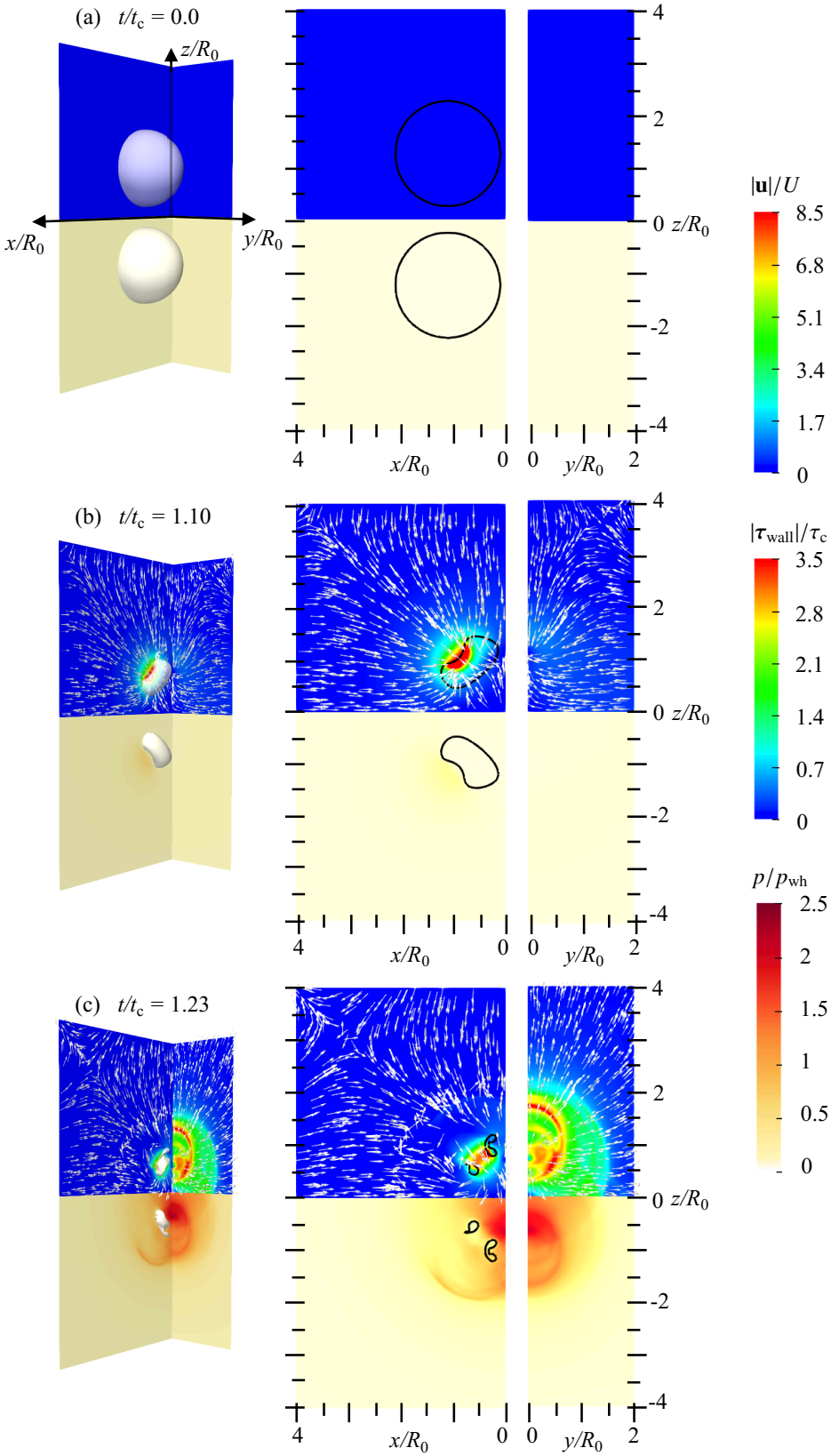

Fig. 4.11: Snapshots of the collapse of two bubbles near a rigid wall at representative times (a) to (c) for the case of $(d/R_0, h/R_0, \Delta p)$ = (2.5, 1.1, 5 MPa), plotting the distributions of the velocity magnitude with vector (upper middle plane), the wall shear stress magnitude with vector (upper wall plane) the pressure (lower middle plane and wall plane). The nominal positions of air-water interfaces ($\alpha_L = \alpha_G = 0.5$) is depicted as black lines in middle plane and white surface in the three-dimensional view listed left.

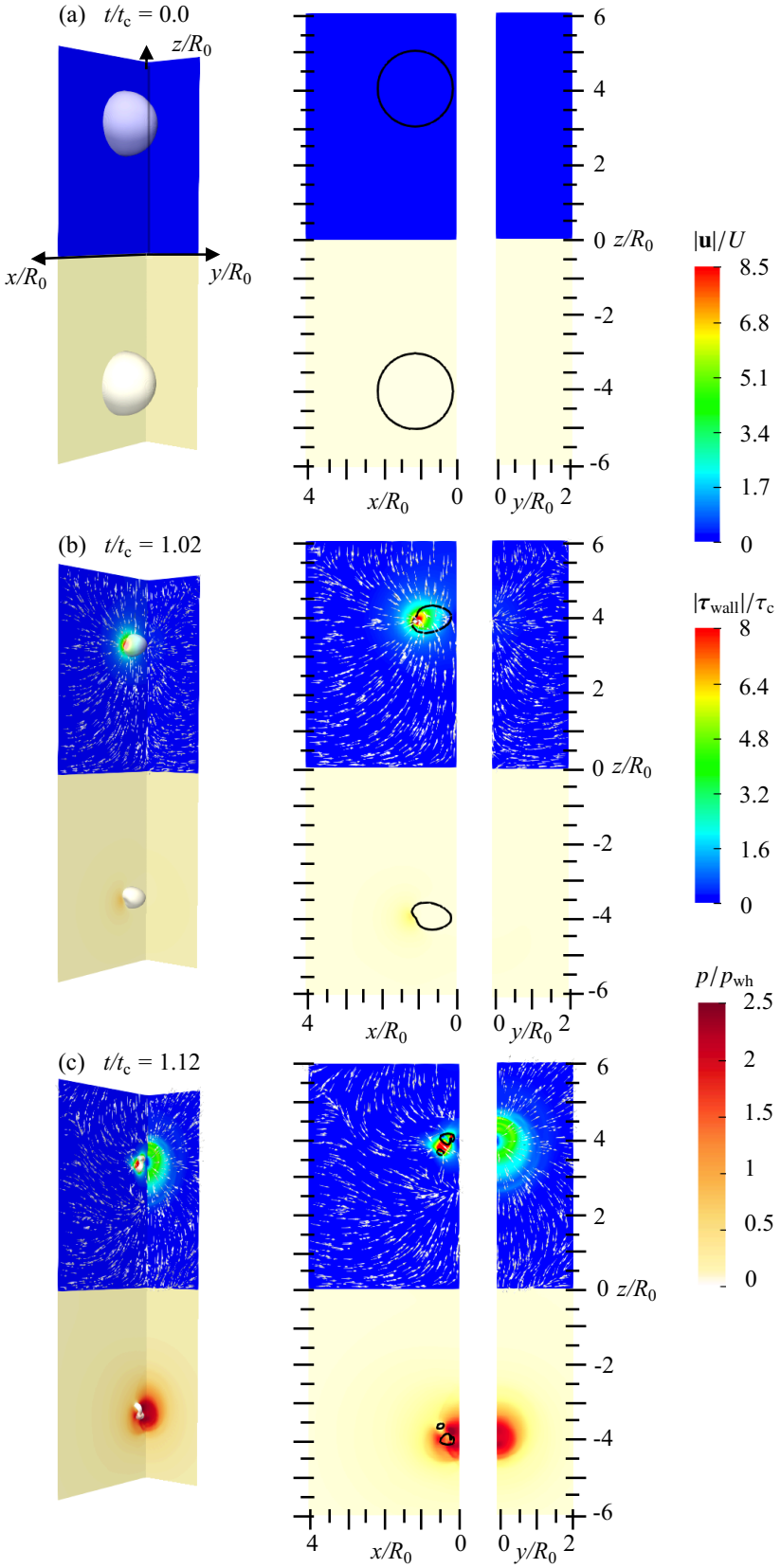

Fig. 4.12: As Fig. 4.11, but with $(d/R_0, h/R_0, \Delta p)$ = (8.0, 1.1, 5 MPa).

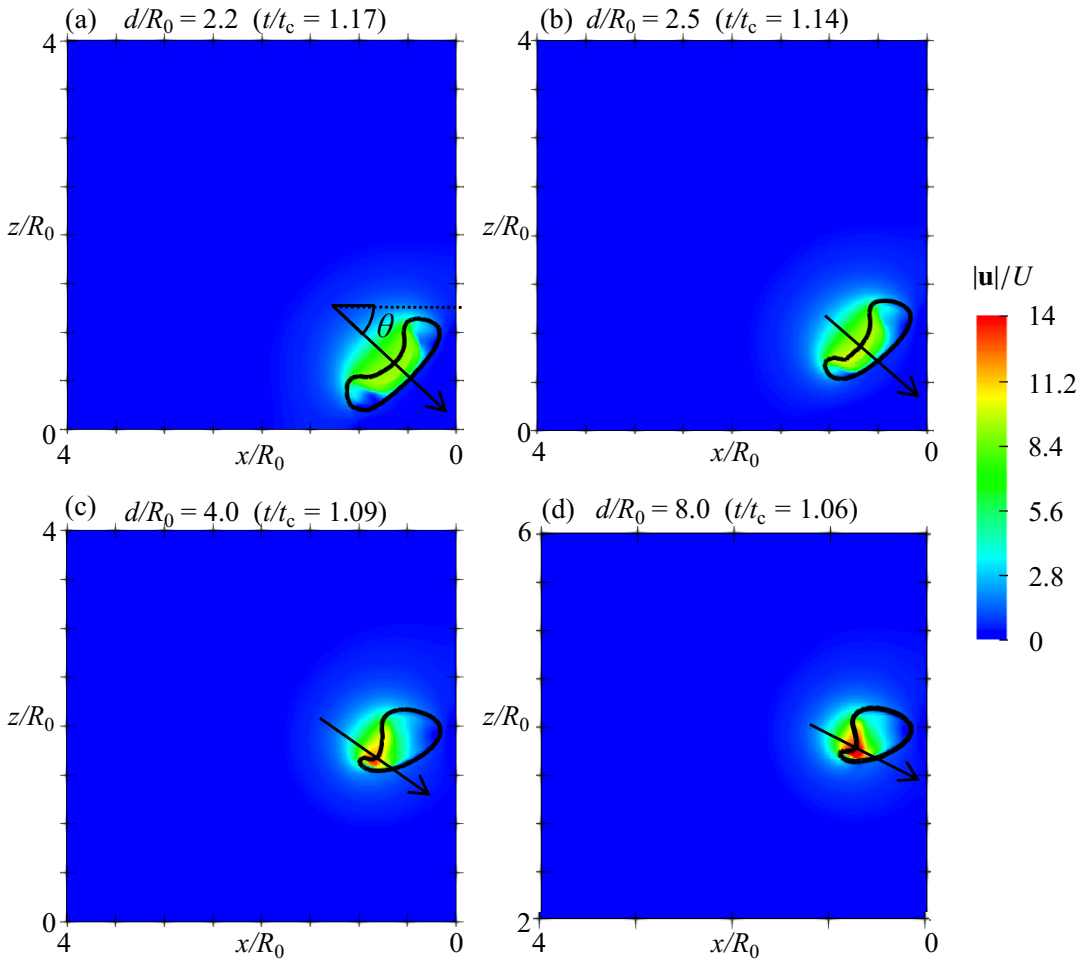

Fig. 4.13: Snapshots of the velocity magnitude and the jet angle measured before the microjet pierces the distal side of the bubble surface. Results for four different distance between bubble pair are presented: (a) $d/R_0 = 2.2$, (b) $d/R_0 = 2.5$, (c) $d/R_0 = 4.0$, (d) $d/R_0 = 8.0$.

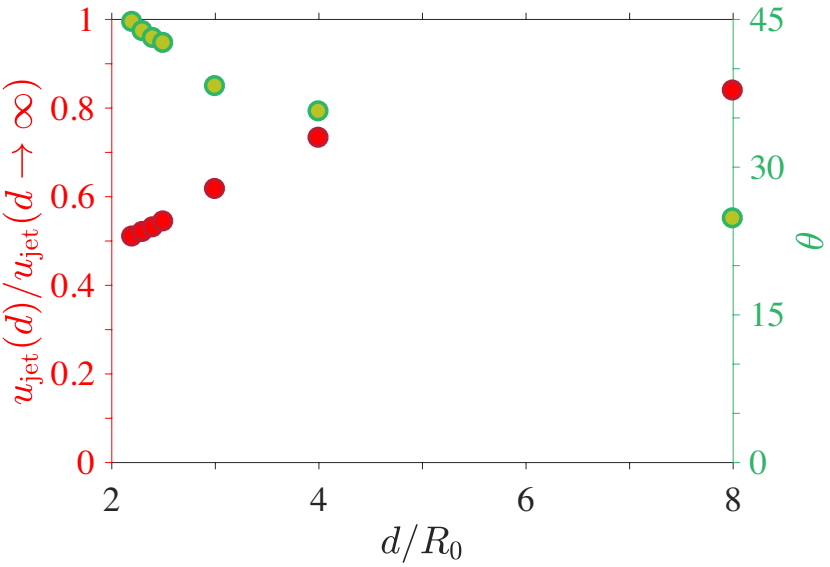

Fig. 4.14: Maximum microjet velocity of the collapsing bubbles, Eq. (4.18), for left vertical axis and the jet angle for right vertical axis are both presented as a function of the distance between bubble pair d/R_0, respectively. Results are shown for $(h/R_0, \Delta p)$ = (1.1, 5 MPa). The left vertical axis is normalized by the maximum microjet velocity in the single bubble case, $u_{\mathrm{jet}}(d \to \infty)$ = 1226 m/s.

for $(h/R_0, \Delta p)$ = (1.1, 5 MPa). We found both the jet speed and the angle approaches to the single bubble case asymptotically as the distance d increases. That is, the effect of the bubble-bubble interaction exponentially increases for the closer inter-bubble distances d.

4.5.2 Wall shear stress evolution

Finally, the flow suppression effect due to the bubble-bubble interaction is quantified from a viewpoint of wall shear stress generation. We first present Fig. 4.15, plotting the spatiotemporal evolution of the absolute wall shear stress on z-axis $|\tau_z(0, z, t)|$ for four different distances d. For the case of closer distance d in Fig. 4.15(a) and (b), the remarkable suppression of wall shear stress is observed. In both configurations, as mentioned in Fig. 4.11(c), the microjet may not directly impact the wall due to the effect of the stagnation between two bubbles. On the other hand, for the case of longer distance d in Fig. 4.15(c) and (d), the spatiotemporal distributions appear more similarly to the single bub-

ble case (see Fig. 4.8): namely, shock-induced wall shear flow is first generated and the jet-impact-induced strong wall shear stress is generated subsequently. If the jet impacts perpendicularly to the wall, wall shear flow is expected to spread both $\pm z$-directions due to the symmetry. In this sense, asymmetry of the wall shear flow formation, around the location of the jet impact $z_\mathrm{i}/R_0 \approx 1.3$, is found in Fig. 4.15(c), while the flow formation becomes more symmetric around $z_\mathrm{i}/R_0 \approx 3.3$ in Fig. 4.15(d). Since weaker wall shear stress appeared near the midpoint of two bubbles in Fig. 4.15(c), it is consistent with the effect of the flow stagnation near the midpoint. We also note that the location of the jet impact z_i becomes closer to the midpoint than the initial bubble location (e.g., $z/R_0 = 2.0$ for $d/R_0 = 4.0$).

To investigate the asymmetric wall shear flow formation, we plot the the spatiotemporal evolution of the absolute wall shear stress on y-axis $|\tau_y(y, z, t)|$ at $z = z_\mathrm{i}$ in Fig. 4.16. In Fig. 4.16(a) and (b), shock-induced shear stress is only observed because of the non-impact. On the other hand, the distributions in Fig. 4.16(c) and (d) depict both the shock- and jet-induced shear stress with the distribution on z-axis.

Finally, the global maximum wall shear stress $\tau_\mathrm{max}(z_\mathrm{max}; d)$ (defined as with Eq. (4.21)) is plotted as a function of the inter-bubble distance d in Fig. 4.17. To compare with the single bubble case, the wall shear stress is normalized by the $\tau_\mathrm{max}(z_\mathrm{max})$ for $(h/R_0, \Delta p) =$ (1.1, 5 MPa). According to Fig. 4.17, we therefore find out that the wall shear flow formation is exponentially attenuated by closing the inter-bubble distance. In reality, this result is consistent with experimental researchs of ultrasonic cleaning; Yamashita *et al.* (2018) and Yamashita & Ando (2019 in press) reported that a highly dense bubble cluster plays a role to reduce the PRE of the ultrasonic cleaning. Hence, our numerical study provides a possible scenario to fully understand the mechanism of bubble-dynamics-based physical cleaning and it may support to describe an optimum cleaning configuration for the high-PRE.

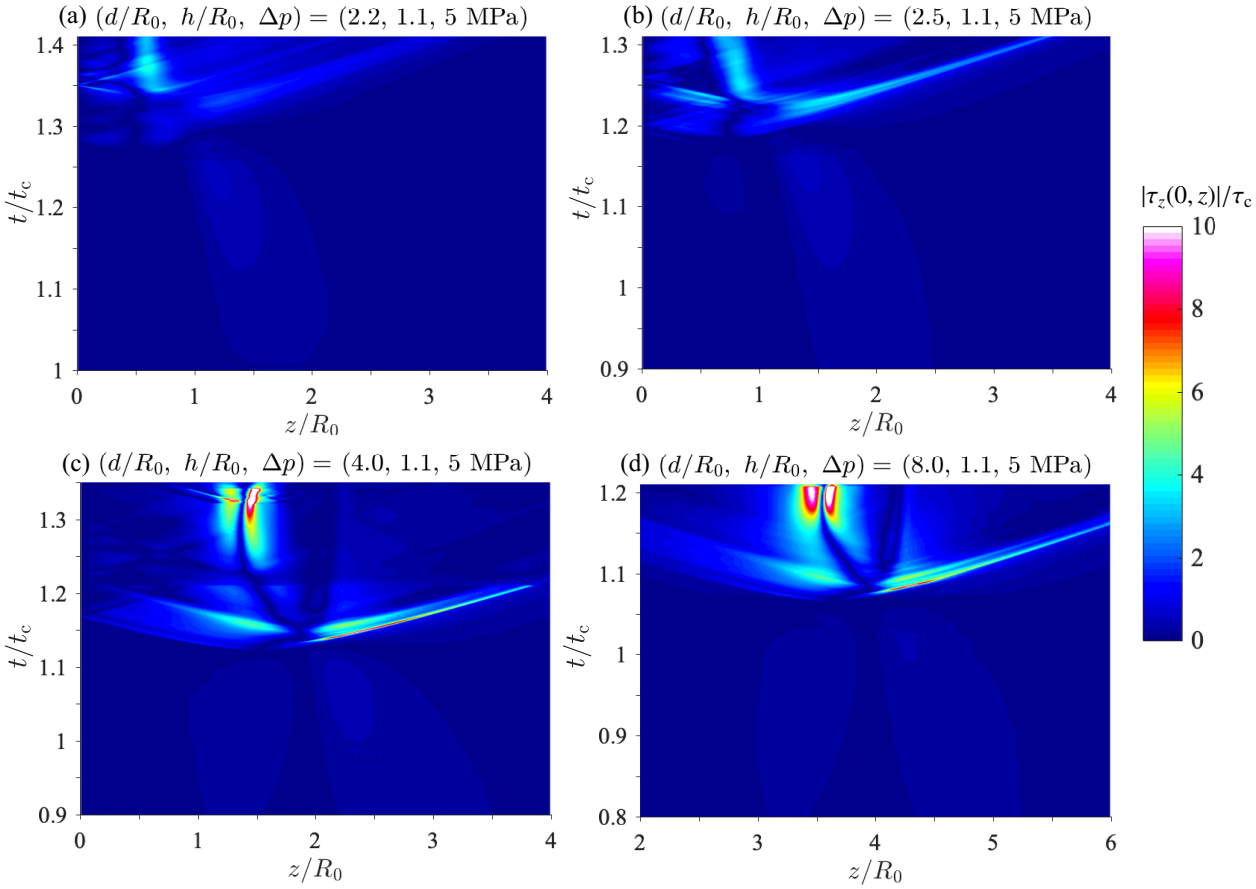

Fig. 4.15: Spatiotemporal evolution of the absolute wall shear stress on z-axis for cases of (h/R_0, Δp) = (1.1, 5 MPa). The probe location in $x-$ and y-direction is fixed at origin. The results for four different distance between bubble pair are presented: (a) $d/R_0 = 2.2$, (b) $d/R_0 = 2.5$, (c) $d/R_0 = 4.0$, (d) $d/R_0 = 8.0$.

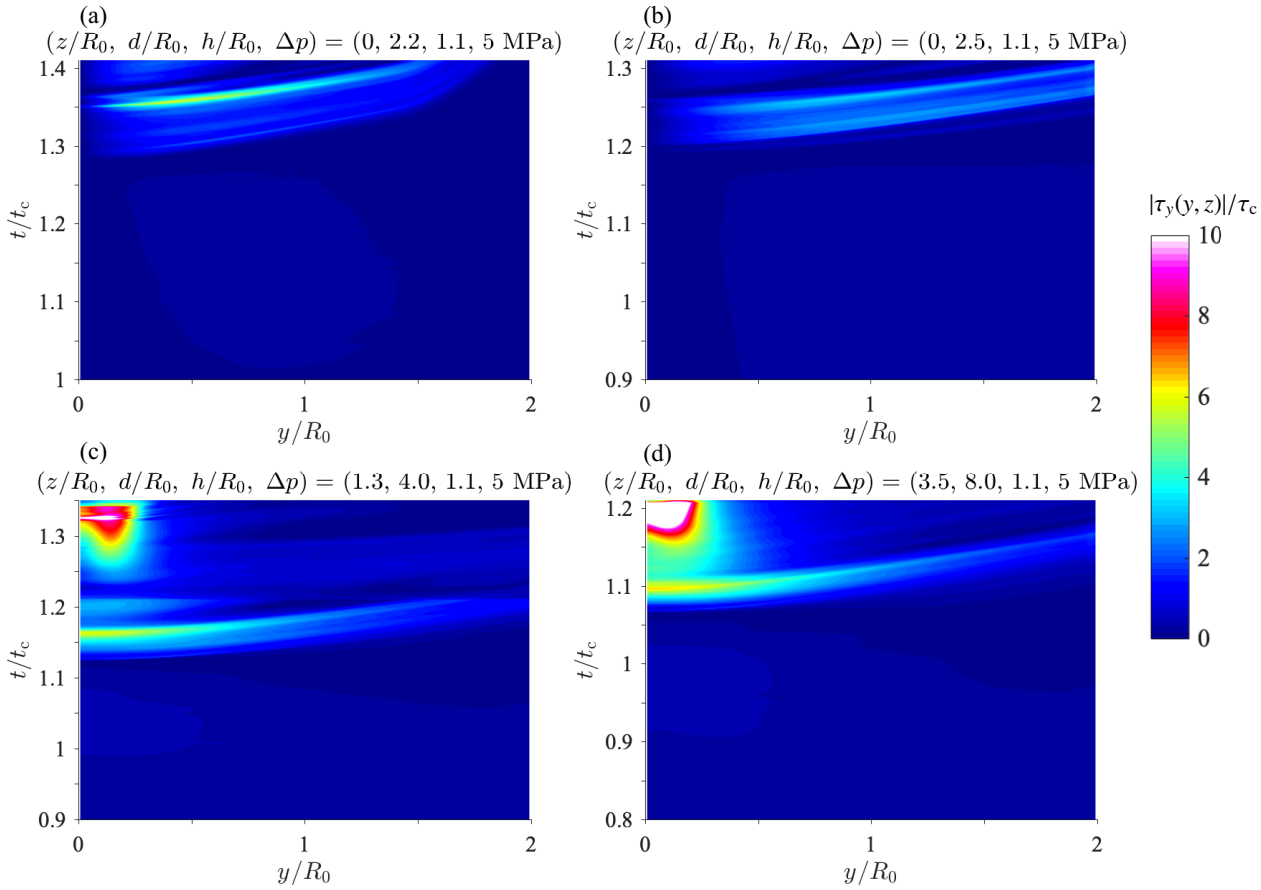

Fig. 4.16: Spatiotemporal evolution of the absolute wall shear stress on y-axis for cases of (h/R_0, Δp) = (1.1, 5 MPa). The probe location in z-direction is the position of microjet impingement, while the x-location is fixed at origin. The presented results are the same as with Fig. 4.15 (a) to (d).

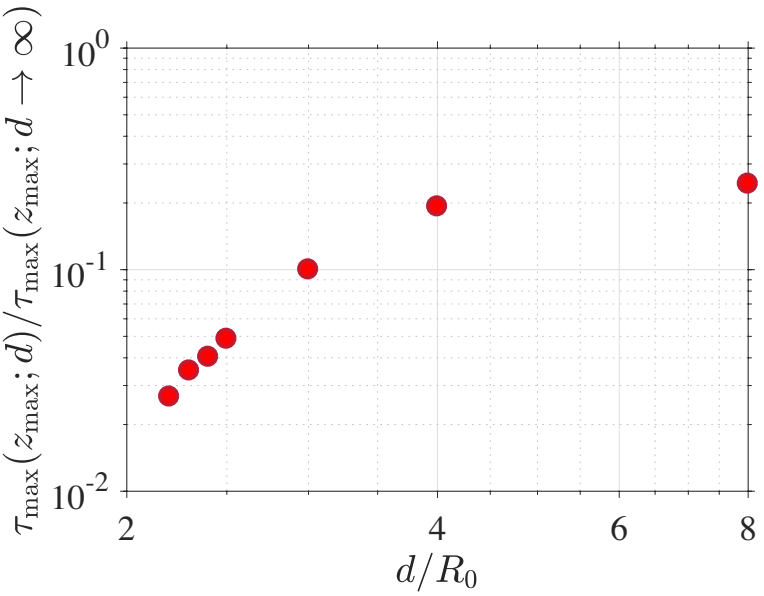

Fig. 4.17: The maximum wall shear stress defined over both time and space as a function of inter-bubble distance d/R_0 for cases of $(h/R_0, \Delta p)$ = (1.1, 5 MPa). The vertical axis is normalized by the maximum wall shear stress in the single bubble case, $\tau_{\max}(z_{\max}; d \to \infty,\ h/R_0 = 1.1,\ \Delta p =$ 5 MPa) = 8.7 MPa.

4.6 Summary

In summary, the wall shear flow formation accompanied by the bubble collapse near a rigid wall was quantified for understanding its performance in context of physical cleaning. We simulated the so-called Rayleigh collapse, which is the collapse of single spherical air bubble (100 μm in radius) in water driven by a sudden pressure rise (ranging from 2 to 10 MPa) at ambience. Simulations were based on the three-dimensional, compressible Navier–Stokes equations. The formation of microjet during the bubble collapse was reproduced correctly (see Figs. 4.4 and 4.5) and we found out the wall shear flow formation is accompanied by the shock wave from the bubble collapse and the jet impingement (see Fig. 4.8). The parametric study for the standoff distance, which determines the initial position of the bubble from the wall, provided the knowledge that the bubble-collapse-induced wall shear stress attenuates exponentially by taking a further standoff distance. The attenuation rate was modeled an empirical power law function (see Fig. 4.10). Finally, we simulated the collapse of a pair of bubbles near a rigid wall to quantify the effect of bubble-bubble interaction in the wall shear flow formation. Two bubbles located laterally to the wall and the inter-bubble distance were changed as a parameter and the other configurations were the same as the single bubble case. The effect of the bubble-bubble interaction clearly appeared in the microjet speed and the angle (see Fig. 4.11). Its effect became lesser by taking a longer inter-bubble distance (see Fig. 4.12). More importantly, wall shear stress evolution was crucially suppressed due to the presence of the neighbor bubble (see Figs. 4.15 and 4.16). We observed the effect of bubble-bubble interaction increased exponentially as two bubbles got closer (see Fig. 4.17). We may say this fact is closely related to the cleaning mechanism and PRE of the ultrasonic cleaning which involves the inception of cavitation clouds near a substrate.

Chapter 5

Concluding remarks

5.1 Conclusions

In this thesis, compressible gas-liquid flow problems consisting of high-speed droplet impact and cavitation bubble collapse near a wall were studied in order to characterize the effect of surface erosion and cleaning given rise to these flows. Direct numerical simulation was carried out based on a shock/interface capturing method. In what follows, numerical investigations we accomplished are summarized and several insights into physical cleaning are recalled.

In Chapter 2, we numerically investigated the possibility of cavitation occurrence in high-speed droplet impact against a deformable wall. We simulated the experiment of Field *et al.* (1989) in which cavitation was observed within the droplet colliding with a solid wall. The Euler flow simulation was able to accurately reproduce important features of the wave propagation within the droplet. The subsequent one-way-coupling simulation based on the Rayleigh–Plesset-type calculation (with the equilibrium radius of bubble nuclei varied from submicrons to microns) suggested the possibility of having cavitation caused by wave interaction within the droplet. More importantly, pressure radiation from the cavitation bubble collapse may overwhelm the initial water-hammer shock; this trend is emphasized for the case of homogeneous-like cavitation that arises from the growth of nanobubble nuclei. Therefore, such cavitation may give rise to additional erosion in the

problem of high-speed droplet impact.

In Chapter 3, we numerically studied high-speed droplet impact against dry/wet rigid walls and discuss it in the context of particle removal. We simulate the high-speed impact of a spherical water droplet with varying the impact velocity and the thickness of a water film at the wall surface, based on the axisymmetric two-dimensional compressible Navier–Stokes equations. First, we studied the acoustic phenomena in the droplet-impact problem. The water-hammer pressure is found to be attenuated by having the thicker liquid film and its decay rate can be fitted empirically by an exponential function. Next, we studied the hydrodynamic phenomena including side jet formation and wall shear flow generation after the acoustic events. In the case of dry walls, the side jet forms in the lateral direction to the wall surface and very large wall shear stress appears just after the passage of the moving contact line. On the contrary, in the case of wet walls, the jet results in the formation of a crown-shape free surface. The wall shear stress is damped significantly under the existence of the liquid film; flow separation can be caused by flow deceleration in the crown-shape liquid film, depending on the film thickness (relative to the droplet diameter). Finally, we considered the case of very small polystyrene particles (10 nm in diameter) attached at the wall of a quartz surface and evaluated with the one-way-coupling manner the particle removal from a balance of the adhesive force (of van der Waals type) and the hydrodynamic force (under the Stokes' approximation). As expected, the particle removal area is augmented by having larger impact velocity and thinner films. We may say that the present simulation approach is helpful when it comes to exploring the optimal cleaning conditions at which the performance of cleaning by the wall shear flow is maximal while the erosion caused by the water-hammer shock loading is minimal.

In Chapter 4, the wall shear flow formation accompanied by the bubble collapse near a rigid wall was quantified for understanding its performance in context of physical clean-

ing. We first simulated the so-called Rayleigh collapse, the collapse of single spherical air bubble in water driven by a sudden pressure rise at ambience, based on the three-dimensional, compressible Navier–Stokes equations. The formation of micro-jet during the bubble collapse was reproduced correctly and we found out the wall shear flow formation is accompanied by the shock wave from the bubble collapse and the jet impingement. The parametric study for the stand-off distance, which determines the initial position of the bubble from the wall, provided the knowledge that the bubble-collapse-induced wall shear stress attenuates exponentially by taking a further stand-off distance and the attenuation rate was modeled an empirical power law function. Finally, we simulated the collapse of a couple of bubbles near a rigid wall to quantify the effect of bubble-bubble interaction in the wall shear flow formation. Two bubbles located laterally facing the wall and the distance between them were changed as parameter and the other configurations were the same as the single bubble study. The effect of bubble-bubble interaction clearly appeared in the speed and the angle of the micro-jet and its effect became lesser by taking a further distance between the bubble pair. More importantly, wall shear stress evolution was crucially suppressed due to the presence of the neighbor bubble. We observed the effect of bubble-bubble interaction increased exponentially as two bubbles got closer. This fact may be closely related to the cleaning mechanism and PRE of the ultrasonic cleaning which involves the inception of cavitation clouds near a substrate.

5.2 Recommendations for future work

5.2.1 Cavitation modeling

In Chapter 2, we claim the possibility of having cavitation in high-speed droplet impact, but the magnitude of cavitation-induced pressure emission is not fully quantified due to some simplifications. In reality, cavitation usually involves some complex phenomena as follows. For instance, the spherical bubble collapse can be so violent that the extreme col-

lapse pressure will give rise to plasma formation (Barber *et al.*, 1997; Hilgenfeldt *et al.*, 1998; Liverts & Apazidis, 2016), which may reduce the energy for the pressure emission. There are another issues of bubble fission (Brennen, 2002; Delale & Tunç, 2004) and higher-order liquid compressibility corrections (Lezzi & Prosperetti, 1987) that tend to damp bubble collapse and will thus reduce its pressure radiation. More importantly, cavitation often appears as a cloud of bubbles where bubble-bubble interaction will play a key role to control the bubble dynamics and produce more violent cavitation collapse. To simply model the effects of cloud bubble dynamics, mixture model of continuum bubbly flow (Wang & Brennen, 1999; Ando *et al.*, 2011; Fuster & Colonius, 2011; Maeda & Colonius, 2018) could be implemented. Namely, two-way-coupling simulation between the Euler equations and the Rayleigh Plesset type equation is then conducted. However, the contribution of non-spherical bubble dynamics is neglected in the above models and it remains a central research topic in the recent numerical study. Though the dynamics of cloud bubble has been already directly simulated by researchers (Tiwari *et al.*, 2015; Ochiai & Ishimoto, 2017), some improvements are still required. For instance, positions of bubble center are spatially fixed and the presence of the preexisting bubbles are assumed (i.e., phase change is neglected).

5.2.2 Physical investigations of high-speed droplet impact and particle removal

In the present study of the droplet impact in Chapter 3, dynamics of the single spherical droplet impact perpendicular to a dry/wet wall is investigated. For a further step, consideration of multiple droplet interactions (e.g., monodisperse droplet train impact (Okorn-Schmidt *et al.*, 2013)) could be conducted. According to the result in Section 3.6, wall shear flow formation depends on the water film thickness (before the impact) and the water film is found to be thinned by the droplet impact. In this sense, secondary droplet impact may give rise to stronger wall shear flow. Moreover, investigation of non-

axisymmetric behavior would be helpful to improve the actual cleaning processes: oblique impact against a wall, for instance. Since the axisymmetric behavior of the droplet impact results in the flow stagnation at the center position of the droplet on the wall, the oblique impact is expected to be more favorable for the wall shear flow formation. It would also be attractive to incorporate with droplet deformation due to the high-speed migration (Meng & Colonius, 2015) before collision because the present study assumes spherical droplet as an initial condition. The non-sphericity of the droplet would also affect the droplet morphology especially in the case of oblique impact. Therefore, we recommend the future research incorporating the capillary effect and extending to the three-dimensional simulation. The surface tension model could be implemented following the work of Meng (2016). Regarding the extension to the three-dimensional simulation, computation with cylindrical coordinates would be a possible idea to minimize the grid effect (Mohseni & Colonius, 2000; Mignone, 2014).

Regarding the particle removal, the present study was evaluated it based on instantaneous torque balances. Thus, the mechanism of particle reattachment is currently neglected. To fully understand the physical mechanism of the particle removal, time evolution of the hydrodynamic torques will be important, which possibly keeps lifting up the contaminant particles. For small particles (O(10 nm) in diameter), the time evolution of the hydrodynamic force would be calculated at Lagrangian points in contact with the rigid wall in one-way-coupling manner. For larger particles, it would require modeling of the flow disturbance due to the presence of the adherent particles. More importantly, investigation of the correlation between the present simple criterion of particle removal and actual PRE in experiments will follow. This evaluation of particle removal would then become a meaningful indicator for experimental works that measures wall shear stress in several physical cleaning applications.

5.2.3 Physical investigations of bubble collapse

For a further investigation of the bubble collapse in Chapter 4, consideration of non-sphericity of the initial bubble and wall-attached hemisphere bubble will be interesting because the jet formation have to differ from the spherical bubble collapse near a wall. It will also be instructive to simulate the bubble oscillation and collapse under an ultrasonic field (Ochiai & Ishimoto, 2017) to provide more practical insights. Namely, the far-field pressure would be extended to a time-dependent variable. Boyd & Becker (2018) While the present study is focusing on the collapse stage, the bubble oscillation would also play a role to remove particles especially in a megasonic cleaning (Busnaina & Gale, 1997; Ochiai & Ishimoto, 2017). Then, challenging issues would be consideration of the surface tension (Schmidmayer *et al.*, 2017; Fuster & Popinet, 2018) and the time-cost of the simulation. Since the prolongation of the simulation time may result in the increasing of the interface smearing, implementation of an interface sharpening algorithm will be beneficial. For instance, THINC (tangent of hyperbola for interface capturing) scheme achieves the interface sharpening by computing numerical fluxes at material interfaces by a hyperbolic tangent function (Shyue & Xiao, 2014; Deng *et al.*, 2017).

For more understanding of the effects of bubble-bubble interactions, additional key parameters will be accounted for: combinations of different bubble sizes, positional relationships (inter-bubble distance and angle) and non-sphericity of initial bubbles. These parametric studies would help to fully understand the complex dynamics of bubble cluster, which includes the effect of non-spherical collapse. However, when the number of bubbles is increased, it has to be challenging because of the numerous initial configurations. Considering such circumstances, further investigation of the collapse of a bubble pair would be essential to predict the dynamics of a larger bubble cluster, because the dynamics of a bubble in the cluster could be described by superposition of the bubble-bubble interactions with respective bubbles. If the non-spherical motion of bubbles is neglected,

this concept results in the model of continuum bubbly flow as mentioned in Section 5.2.1. To take into account the non-spherical behavior (i.e., micro-jet formation) in a reduced bubbly flow model, further insights into the dynamics of the collapse of a bubble pair should be required.

Appendix A

Modeling of particle adhesion force by JKR theory

For particles of our concern (10 nm in diameter), van der Waals force dominates other particle adhesion forces (Burdick *et al.*, 2005; Zoeteweij *et al.*, 2009). Accounting for the effect of particle deformation caused by adhesion against a flat surface, the van der Waals force is written as (Busnaina *et al.*, 2002)

$$F_{\mathrm{vdW}} = \frac{A_{\mathrm{H}} d}{12 H_{\mathrm{p}}^2}\left(1 + \frac{2a_{\mathrm{JKR}}^2}{H_{\mathrm{p}} d}\right), \tag{A.1}$$

where A_{H} is the material-dependent Hamaker constant, d is the particle diameter, H_{p} is the particle-to-surface distance (typically, $H_{\mathrm{p}} = 0.4$ nm (Visser, 1995)), and a_{JKR} is the contact radius determined by Johnson–Kendall–Roberts (JKR) theory (Johnson, 1997; Israelachvili, 2011; Zhang *et al.*, 2000) (see Fig. 3.3). In this theory, the contact radius is related to the work done by the adhesion and is thus given by:

$$a = \sqrt[3]{\frac{3\pi \cdot W_{\mathrm{a}} \cdot d^2}{2K}}, \tag{A.2}$$

where W_{a} is the work done by particle adhesion:

$$W_{\mathrm{a}} = \frac{A_{\mathrm{H}}}{12\pi \cdot h^2}. \tag{A.3}$$

The deformation constant K is defined by

$$K = \frac{4}{3}\left[\frac{1-\nu_{\mathrm{p1}}^2}{Y_1} + \frac{1-\nu_{\mathrm{p2}}^2}{Y_2}\right]^{-1}, \tag{A.4}$$

Table A.1: Material properties of PSL (particle) and quartz for the evaluation of particle deformation.

Material	Young's modulus Y [GPa]	Poisson's ratio ν_p [–]
PSL	3.1	0.29
quartz	74	0.17

where Y is Young's modulus, ν_p is Poisson's ratio, and subscripts 1 and 2 refer to the particle and the surface, respectively. As a representative example, we consider the removal of a polystylene latex (PSL) sphere from quartz surfaces which is immersed in water, based on the experiment of Burdick *et al.* (2005). According to their experimental measurement, the average Hamaker constant A_H for PSL to quartz in water is 1.02×10^{-20} Nm. Other properties are listed in Table A.1.

Appendix B

Kinetic energy dissipation during the droplet impact

To estimate the water temperature rise in the wall shear flow induced by the droplet impact, we investigate the evolution of kinetic energy dissipation ϵ (with the assumption of constant μ_{L} and μ_{G}):

$$\epsilon \equiv \frac{2\mu}{\rho}\left[\left\{\frac{\partial u_z}{\partial z} - \frac{1}{3}\left(\frac{\partial u_z}{\partial z} + \frac{\partial u_r}{\partial r} + \frac{u_r}{r}\right)\right\}^2 + \left\{\frac{\partial u_r}{\partial r} + \frac{u_r}{r} - \frac{1}{3}\left(\frac{\partial u_z}{\partial z} + \frac{\partial u_r}{\partial r} + \frac{u_r}{r}\right)\right\}^2 + \frac{1}{2}\left(\frac{\partial u_z}{\partial r} + \frac{\partial u_r}{\partial z}\right)^2\right], \tag{B.1}$$

which can be computed by postprocessing the simulated velocity field. Since kinetic energy dissipation corresponds to the irreversible conversion of mechanical energy to thermal energy via the action of viscosity, it can be used to estimate temperature increase. Figure B.1 illustrates the kinetic energy dissipation per unit mass during the droplet impingement ($V_{\mathrm{i}} = 50$ m/s, the highest speed in our problem setup) for dry and wet cases ($l/D = 0.5$) at the same time frame in Figures 3.6 and 3.8 (d)-(f). The kinetic energy dissipation inside the droplet is emphasized near the wall (and its crown-shape rim for the wet case) where the velocity gradient becomes steeper. We obtain the largest dissipation in the dry case in which the wall shear stress induced by the droplet impact is much larger than that in the wet cases. Hence, we consider the dry case at which the temperature rise is expected to be maximal. In this case, the maximal dissipation that appears at the wall is approximately at 10^8 J/(kg s) and its duration is about 4 μs. The local heat deposition is

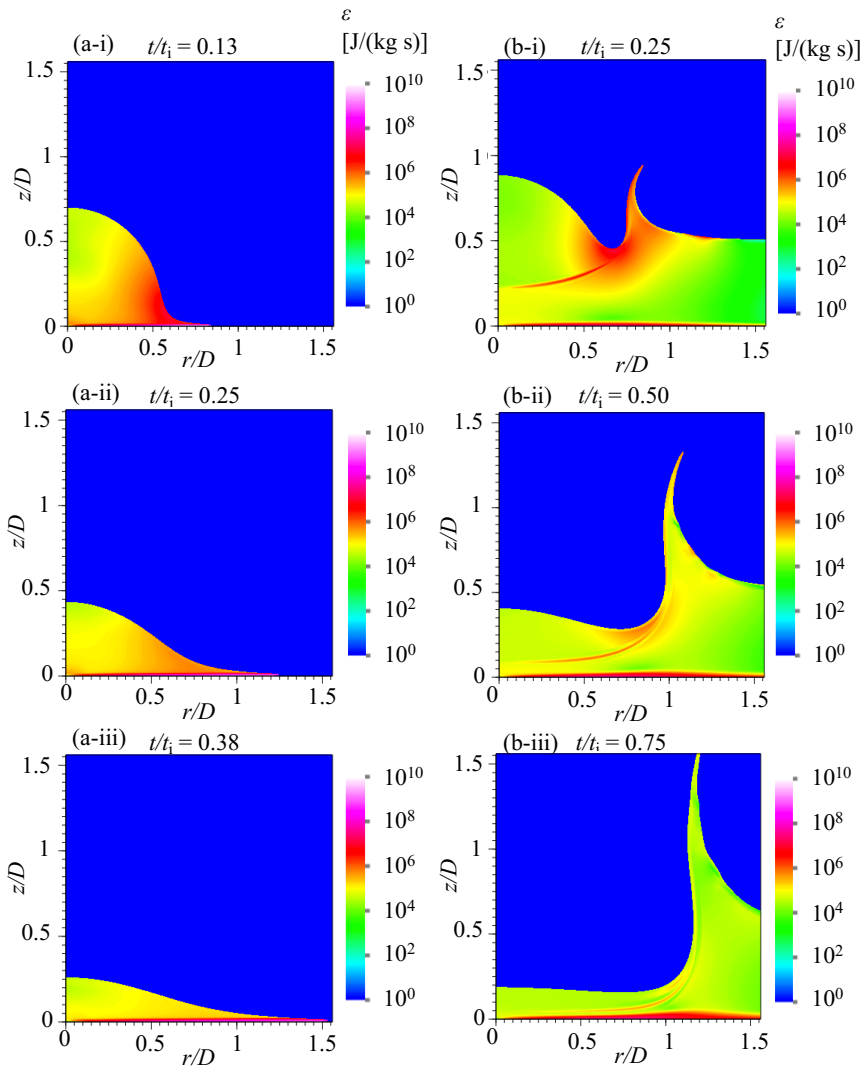

Fig. B.1: The liquid-phase kinetic energy dissipation rate at representative times (i) to (iii) for $V_i = 50$ m/s and for different film thickness (i) $l/D = 0$ and (ii) $l/D = 0.5$.

estimated as the product of these values and the temperature rise (i.e., its division by the specific heat capacity of the water) is predicted at $O(0.1\ \text{K})$. Therefore, the temperature rise within the droplet is at most $O(0.1\ \text{K})$ in our problem setup and has thus a negligible impact on values of the physical properties.

Bibliography

Agudo, J. R., Illigmann, C., Luzi, G., Laukart, A., Delgado, A. & Wierschem, A. 2017*a* Shear-induced incipient motion of a single sphere on uniform substrates at low particle Reynolds numbers. *J. Fluid Mech.* **825**, 284–314.

Agudo, J. R., Luzi, G., Han, J., Hwang, M., Lee, J. & Wierschem, A. 2017*b* Detection of particle motion using image processing with particular emphasis on rolling motion. *Rev. Sci. Instrum.* **88** (5), 051805.

Allaire, G., Clerc, S. & Kokh, S. 2002 A five-equation model for the simulation of interfaces between compressible fluids. *J. Comput. Phys.* **181**, 577–616.

Ando, K., Colonius, T. & Brennen, C. E. 2011 Numerical simulation of shock propagation in a polydisperse bubbly liquid. *Int. J. Multiphase Flow* **37** (6), 596–608.

Arndt, R. E. A. 1981 Cavitation in fluid machinery and hydraulic structures. *Ann. Rev. Fluid Mech.* **13**, 273–328.

Banitabaei, S. A. & Amirfazli, A. 2017 Droplet impact onto a solid sphere: Effect of wettability and impact velocity. *Phys. Fluids* **29** (6), 062111.

Barber, B. P., Hiller, R. A., Löfstedt, R., Putterman, S. J. & Weninger, K. R. 1997 Defining the unknowns of sonoluminescence. *Phys. Rep.* **281**, 65–143.

Beig, S. A. 2018 A computational study of the inertial collapse of gas bubbles near a rigid surface. PhD thesis, University of Michigan.

Beig, S. A., Aboulhasanzadeh, B. & Johnsen, E. 2018 Temperatures produced by inertially collapsing bubbles near rigid surfaces. *J. Fluid Mech.* **852**, 105–125.

Beig, S. A. & Johnsen, E. 2015 Maintaining interface equilibrium conditions in compressible multiphase flows using interface capturing. *J. Comput. Phys.* **302**, 548–566.

Boelens, A. M. P. & de Pablo, J. J. 2018 Simulations of splashing high and low viscosity droplets. *Phys. Fluids* **30** (7), 072106.

Boyd, B. & Becker, S. 2018 Numerical modelling of an acoustically-driven bubble collapse near a solid boundary. *Fluid Dyn. Res.* **50** (6).

Brenn, G., Helpioe, T. & Durst, F. 1997 A new apparatus for the production of monodisperse sprays at high flow rates. *Chem. Eng. Sci.* **52** (No. 2), 237–244.

Brennen, C. E. 2002 Fission of collapsing cavitation bubbles. *J. Fluid Mech.* **472**, 153–166.

Brennen, C. E. 2014 *Cavitation and Bubble Dynamics*. New York, USA: Cambridge University Press.

Brennen, C. E. 2015 Cavitation in medicine. *Interface Focus* **5** (5).

Brujan, E. A. 2011 *Cavitation in Non-Newtonian Fluids: Wtih Biomedical and Bioengineering Applications*. Springer.

Brujan, E. A., Keen, G. S., Vogel, A. & Blake, J. R. 2002 The final stage of the collapse of a cavitation bubble close to a rigid boundary. *Phys. Fluids* **14** (1), 85.

Brunton, J. H. & Camus, J. J. 1970 The flow of liquid drop during impact. *Proc. Third Int'l Conf. on Rain Erosion and Assoc. Phenomena* pp. 327–352.

Brunton, J. H. & Rochester, M. C. 1979 Erosion of solid surfaces by the impact of liquid drops. *Treatise on Mater. Sci. Tech.* **16**, 185–248.

Burdick, G. M., Berman, N. S. & Beaudoin, S. P. 2005 Hydrodynamic particle removal from surfaces. *Thin Solid Films* **488**, 116–123.

Busnaina, A. A. & Gale, G. W. 1997 Removal of silica particles from silicon substrates using megasonic cleaning. *Particulate Sci. Technol.* **15**, 361–369.

Busnaina, A. A., Lin, H., Moumen, N., Feng, J.-w. & Taylor, J. 2002 Particle adhesion and removal mechanisms in Post-CMP cleaning processes. *IEEE Trans. Semicond. Manuf.* **15** (4), 374–382.

Caupin, F. & Herbert, E. 2006 Cavitation in water: a review. *C. R. Physique* **7**, 1000–1017.

Ceccio, S. L. & Brennen, C. E. 1991 Observations of the dynamics and acoustics of travelling bubble cavitation. *J. Fluid Mech.* **233**, 633–660.

Chahine, G. L. & Hsiao, C.-T. 2015 Modelling cavitation erosion using fluid-material interaction simulations. *Interface Focus* **5**, 20150016.

Chahine, G. L., Kapahi, A., Choi, J. K. & Hsiao, C. T. 2016 Modeling of surface cleaning by cavitation bubble dynamics and collapse. *Ultrason. Sonochem.* **29**, 528–549.

Charalampous, G. & Hardalupas, Y. 2017 Collisions of droplets on spherical particles. *Phys. Fluids* **29** (10), 103305.

Chen, C.-Y., Panigrahi, B., Chong, K.-S., Li, W.-H., Liu, Y.-L. & Lu, T.-Y. 2018 Hydrodynamic investigation of a wafer rinse process through numerical modeling and flow visualization methods. *J. Fluids Eng.* **140** (8).

Cheng, L. 1977 Dynamic spreading of drops impacting onto a solid surface. *Ind. Eng. Chem., Process Des. Dev.* **16** (2), 192–197.

Cook, S. 1928 Erosion by water-hammer. *Proc. R. Soc. of London, Ser. A* pp. 481–488.

Coralic, V. & Colonius, T. 2014 Finite-volume WENO scheme for viscous compressible multicomponent flows. *J. Comput. Phys.* **274**, 95–121.

Coward, A. V., Renardy, Y. Y., Renardy, M. & Richards, J. R. 1997 Temporal evolution of periodic disturbances in two-layer Couette flow. *J. Comput. Phys.* **132**, 346–361.

Crum, L. A. 1994 Sonoluminescence, sonochemistry, and sonophysics. *J. Acoust. Soc. Am.* **95** (1), 559–562.

Dadone, A. & Grossman, B. 1994 Surface boundary conditions for the numerical solution of the euler equations. *AIAA J.* **32**, 285–293.

van Dam, D. B. & Le Clerc, C. 2004 Experimental study of the impact of an ink-jet printed droplet on a solid substrate. *Phys. Fluids* **16** (9), 3403.

Dear, J. P. & Field, J. E. 1988 High-speed photography of surface geometry effects in liquid/ solid impact. *J. Appl. Phys.* **63** (4), 1015–1021.

Del Grosso, V. A. & Mader, C. W. 1972 Speed of sound in pure water. *J. Acoust. Soc. Am.* **52** (5B), 1442–1446.

Delale, C. F. & Tunç, M. 2004 A bubble fission model for collapsing cavitation bubbles. *Phys. Fluids* **16** (11).

Deng, X., Inaba, S., Xie, B., Shyue, K.-M. & Xiao, F. 2017 Implementation of BVD (boundary variation diminishing) algorithm in simulations of compressible multiphase flows. *arXiv preprint arXiv:1704.08041* .

Dijkink, R. & Ohl, C.-D. 2008 Measurement of cavitation induced wall shear stress. *Appl. Phys. Lett.* **93** (25).

Engel, O. G. 1955 Waterdrop collisions with solid surfaces. *J. R. Natl. Stand.* **54** (5), 281–298.

Erkan, N. & Okamoto, K. 2014 Full-field spreading velocity measurement inside droplets impinging on a dry solid surface. *Exp. Fluids* **55**, 1845.

Fan, F.-G., Soltani, M., Ahmadi, G. & Hart, S. C. 1997 Flow-induced resuspension of rigid-link fibers from surfaces. *Aerosol Sci. Technol.* **27** (2), 97–115.

Fernando, W. J. N., Lok, Y. H., Don, M. M., Madhaven, V. & Tay, W. S. 2011 Experimental and modeling studies of particle removal in post silicon chemical mechanical planarization cleaning process. *Thin Solid Films* **519** (10), 3242–3248.

Field, J. E., Camus, J. J., Tinguely, M., Obreschkow, D. & Farhat, M. 2012 Cavitation in impacted drops and jets and the effect on erosion damage thresholds. *Wear* **290–291**, 154–160.

Field, J. E., Dear, J. P. & Ogren, J. E. 1989 The effects of target compliance on liquid drop impact. *J. Appl. Phys.* **65** (2), 533–540.

Henry de Frahan, M. T., Varadan, S. & Johnsen, E. 2015 A new limiting procedure for discontinuous galerkin methods applied to compressible multiphase flows with shocks and interfaces. *J. Comput. Phys.* **280**, 489–509.

Frommhold, P. E., Mettin, R. & Ohl, C.-D. 2015 Height-resolved velocity measurement of the boundary flow during liquid impact on dry and wetted solid substrates. *Exp. Fluids* **56**, 76.

Fujikawa, S. & Akamatsu, T. 1980 Effects of the non-equilibrium condensation of vapour on the pressure wave produced by the collapse of a bubble in a liquid. *J. Fluid Mech.* **97**, 481–512.

Fujisawa, K., Yamagata, T. & Fujisawa, N. 2018 Damping effect on impact pressure from liquid droplet impingement on wet wall. *Annals Nucl. Energy* **121**, 260–268.

Fuster, D. & Colonius, T. 2011 Modelling bubble clusters in compressible liquids. *J. Fluid Mech.* **688**, 352–389.

Fuster, D. & Popinet, S. 2018 An all-Mach method for the simulation of bubble dynamics problems in the presence of surface tension. *J. Comput. Phys.* **374**, 752–768.

Gale, G. W. & Busnaina, A. A. 1999 Roles of cavitation and acoustic streaming in megasonic cleaning. *Particulate Sci. Technol.* **17** (3), 229–238.

Gilmore, F. R. 1952 The growth or collapse of a spherical bubble in a viscous compressible liquid. *California Institute of Technology Engineering Report* **26**, 1–40.

Glauert, M. B. 1956 The wall jet. *J. Fluid Mech.* **1**, 625–643.

Gojani, A. B., Ohtani, K., Takayama, K. & Hosseini, S. H. R. 2009 Shock Hugoniot and equations of states of water, castor oil, and aqueous solutions of sodium chloride, sucrose and gelatin. *Shock Waves* pp. 1–6.

Gottlieb, S. & Shu, Chi-Wang 1998 Total variation diminishing Runge–Kutta schemes. *Math. Comput.* **67** (221), 73–85.

Guo, Y. & Lian, Y. 2017 High-speed oblique drop impact on thin liquid films. *Phys. Fluids* **29** (8), 082108.

Haller, K. K., Poulikakos, D., Ventikos, Y. & Monkewitz, P. 2003 Shock wave formation in droplet impact on a rigid surface: lateral liquid motion and multiple wave structure in the contact line region. *J. Fluid Mech.* **490**, 1–14.

Haller, K. K., Ventikos, Y., Poulikakos, D. & Monkewitz, P. 2002 Computational study of high-speed liquid droplet impact. *J. Appl. Phys.* **92** (5), 2821.

Hansson, I., Kedrinskii, V. & Mørch, K. A. 1982 On the dynamics of cavity clusters. *J. Phys. D: Appl. Phys* **15**, 1725–1734.

Harkin, A., Nadim, A. & Kaper, T. J. 1999 On acoustic cavitation of slightly subcritical bubbles. *Phys. Fluids* **11** (2), 274.

Harten, A., Lax, P. D. & van Leer, B. 1983 On upstream differencing and Godunov-type schemes for hyperbolic conservation laws. *SIAM Rev.* **25** (No. 1), 35–61.

Henry, C. & Minier, J.-P. 2014 Progress in particle resuspension from rough surfaces by turbulent flows. *Prog. Energy Combust. Sci.* **45**, 1–53.

Herbert, E., Balibar, S. & Caupin, F. 2006 Cavitation pressure in water. *Phys. Rev. E* **74** (041603).

Heymann, F. J. 1969 High-speed impact between a liquid drop and a solid surface. *J. Appl. Phys.* **40**, 5113–5122.

Hilgenfeldt, S., Brenner, M. P., Grossmann, S. & Lohse, D. 1998 Analysis of Rayleigh–Plesset dynamics for sonoluminescing bubbles. *J. Fluid Mech.* **365**, 171–204.

Huang, X., Wan, K.-T. & Taslim, M. E. 2018 Axisymmetric rim instability of water droplet impact on a super-hydrophobic surface. *Phys. Fluids* **30** (9), 094101.

Huang, Y. C., G., H. F. & Mitchell, T. M. 1973 Note on shock-wave velocity in high-speed liquid-solid impact. *J. Appl. Phys.* **44** (4), 1868–1869.

Huh, C & Scriven, L. E. 1971 Hydrodynamic model of steady movement of a solid/liquid/fluid contactline. *J. Colloid Interface Sci.* **35** (1).

Ida, M. 2009 Multibubble cavitation inception. *Phys. Fluids* **21** (11), 113302.

Israelachvili, J. N. 2011 *Intermolecular and Surface Forces*, 3rd edn. Elsevier.

Johnsen, E. 2007 Numerical Simulations of Non-spherical Bubble Collapse. PhD thesis, California Institute of Technology.

Johnsen, E. & Colonius, T. 2006 Implementation of WENO schemes in compressible multicomponent flow problems. *J. Comput. Phys.* **219** (2), 715–732.

Johnsen, E. & Colonius, T. 2009 Numerical simulations of non-spherical bubble collapse. *J. Fluid Mech.* **629**, 231–262.

Johnson, K. L. 1997 Adhesion and friction between a smooth elastic spherical asperity and a plane surface. *Proc. R. Soc. Lond. A* **453**, 163–179.

Kennedy, C. F. & Field, J. E. 2000 Damage threshold velocities for liquid impact. *J. Mater. Sci.* **35**, 5331–5339.

Kern, W. 1990 The evolution of silicon wafer cleaning technology. *J. Electrochem. Soc.* **137** (6), 1887–1892.

Khodaparast, S., Boulogne, F., Poulard, C. & Stone, H. A. 2017 Water-based peeling of thin hydrophobic films. *Phys. Rev. Lett.* **119** (15), 154502.

Kim, H.-Y., Park, S.-Y. & Min, K. 2003 Imaging the high-speed impact of microdrop on solid surface. *Rev. Sci. Instrum.* **74** (11), 4930–4937.

Kim, T.-H. & Kim, H.-Y. 2014 Disruptive bubble behaviour leading to microstructure damage in an ultrasonic field. *J. Fluid Mech.* **750**, 355–371.

Knapp, R. T. 1955 Recent investigations of the mechanics of cavitation and cavitation damage. *Trans. ASME* **77**, 1045–1053.

Kobayashi, K., Nagayama, T., Watanabe, M., Fujii, H. & Kon, M. 2018 Molecular gas dynamics analysis on condensation coefficient of vapour during gasvapour bubble collapse. *J. Fluid Mech.* **856**, 1045–1063.

Kohli, R. & Mittal, K. L. 2011 *Developments in Surface Contamination and Cleaning: Methods for Removal of Particle Contaminants*, , vol. Three. Elsevier.

Lauterborn, W. & Bolle, H. 1975 Experimental investigations of cavitation-bubble collapse in the neighbourhood of a solid boundary. *J. Fluid Mech.* **72**, 391–399.

Le Métayer, O. & Saurel, R. 2016 The Noble-Abel Stiffened-Gas equation of state. *Phys. Fluids* **28** (4), 046102.

Lesser, M. B. 1981 Analytic solutions of liquid-drop impact problems. *Proc. R. Soc. Lond. A* **377**, 289–308.

Lezzi, A. & Prosperetti, A. 1987 Bubble dynamics in a compressible liquid. part 2. second-order theory. *J. Fluid Mech.* **185**, 289–321.

Li, E. Q. & Thoroddsen, S. T. 2015 Time-resolved imaging of a compressible air disc under a drop impacting on a solid surface. *J. Fluid Mech.* **780**, 636–648.

Li, E. Q., Vakarelski, I. U. & Thoroddsen, S. T. 2015 Probing the nanoscale: the first contact of an impacting drop. *J. Fluid Mech.* **785** (R2).

Li, X., Strojwas, A., Swecker, A., Reddy, M., Milor, L. & Lin, Y.-T. 1997 Modeling of defect propagation/growth for yield impact prediction in VLSI manufacturing. *SPIE* **3216**, 167–178.

Liverts, M. & Apazidis, N. 2016 Limiting temperatures of spherical shock wave implosion. *Phys. Rev. Lett.* **116** (014501).

Ma, X., Huang, B., Li, Y., Chang, Q., Qiu, S., Su, Z., Fu, X. & Wang, G. 2018 Numerical simulation of single bubble dynamics under acoustic travelling waves. *Ultrason. Sonochem.* **42**, 619–630.

Maeda, K. & Colonius, T. 2018 Eulerian–Lagrangian method for simulation of cloud cavitation. *J. Comput. Phys.* **371**, 994–1017.

Mandre, S., Mani, M. & Brenner, M. 2009 Precursors to splashing of liquid droplets on a solid surface. *Phys. Rev. Lett.* **102** (134502).

Maxwell, A. D., Cain, C. A., Hall, T. L., Fowlkes, J. B. & Xu, Z. 2013 Probability of cavitation for single ultrasound pulses applied to tissues and tissue-mimicking materials. *Ultrasound Med. Biol.* **39** (No. 3), 449–465.

Maxwell, J. C. 1890 *The Scientific Papers of James Clerk Maxwell*, , vol. 2. University Press.

Meng, J. C. 2016 Numerical simulations of droplet aerobreakup. PhD thesis, California Institute of Technology.

Meng, J. C. & Colonius, T. 2015 Numerical simulations of the early stages of high-speed droplet breakup. *Shock Waves* **25**, 399–414.

Mignone, A. 2014 High-order conservative reconstruction schemes for finite volume methods in cylindrical and spherical coordinates. *J. Comput. Phys.* **270**, 784–814.

Miller, G. H. & G., P. E. 1996 A high-order Godunov method for multiple condensed phases. *J. Comput. Phys.* **128** (No. 0220), 134–164.

Mohseni, K. & Colonius, T. 2000 Numerical treatment of polar coordinate singularities. *J. Comput. Phys.* **157**, 787–795.

Mørch, K. A. 2015 Cavitation inception from bubble nuclei. *Interface Focus* **5** (20150006).

Murrone, A. & Guillard, H. 2005 A five equation reduced model for compressible two phase flow problems. *J. Comput. Phys.* **202** (2), 664–698.

Nagayama, K., Mori, Y., Shimada, K. & Nakahara, M. 2002 Shock Hugoniot compression curve for water up to 1 GPa by using a compressed gas gun. *J. Appl. Phys* **91** (1).

Navier, C. 1823 Memoirs de l'academie. *Royale des Sciences de l'Institut de France* **1**, 414–416.

Obreschkow, D., Dorsaz, N., Kobel, P., de Bosset, A., Tinguely, M., Field, J. & Farhat, M. 2011 Confined shocks inside isolated liquid volumes: A new path of erosion? *Phys. Fluids* **23** (10), 101702.

Ochiai, N. & Ishimoto, J. 2017 Numerical investigation of multiple-bubble behaviour and induced pressure in a megasonic field. *J. Fluid Mech.* **818**, 562–594.

O'Hern, T. J., d'Agostino, L. & Acosta, A. J. 1988 Comparison of holographic and coulter counter measurements of cavitation nuclei in the ocean. *J. Fluids Eng.* **110** (200).

Ohl, C.-D., Arora, M., Dijkink, R., Janve, V. & Lohse, D. 2006*a* Surface cleaning from laser-induced cavitation bubbles. *Appl. Phys. Lett.* **89** (7).

Ohl, C. D., Arora, M., Ikink, R., de Jong, N., Versluis, M., Delius, M. & Lohse, D. 2006*b* Sonoporation from jetting cavitation bubbles. *Biophys. J.* **91** (11), 4285–4295.

Okorn-Schmidt, H. F., Holsteyns, F., Lippert, A., Mui, D., Kawaguchi, M., Lechner, C., Frommhold, P. E., Nowak, T., Reuter, F., Pique, M. B., Cairos, C. & Mettin, R.

2013 Particle cleaning technologies to meet advanced semiconductor device process requirements. *ECS J. Solid State Sci. Tech.* **3** (1), N3069–N3080.

O'Neill, M. E. 1968 A sphere in contact with a plane wall in a slow linear shear flow. *Chem. Eng. Sci.* **23**, 1293–1298.

Pasandideh-Fard, M., Bhola, S., Chandra, S. & Mostaghimi, J. 1998 Deposition of tin droplets on a steel plate: simulations and experiments. *Int. J. Heat Mass Transfer* **41**, 2929–2945.

Pasandideh-Fard, M., Qiao, Y. M., Chandra, S. & Mostaghimi, J. 1996 Capillary effects during droplet impact on a solid surface. *Phys. Fluids* **8** (3), 650.

Patanker, S. V. 1991 *Computation of Conduction and Duct Flow Heat Transfer*. Taylor and Francis.

Perigaud, G. & Saurel, R. 2005 A compressible flow model with capillary effects. *J. Comput. Phys.* **209**, 139–178.

Philipp, A. & Lauterborn, W. 1998 Cavitation erosion by single laser-produced bubbles. *J. Fluid Mech.* **361**, 75–116.

Plesset, M. S. & Chapman, R. B. 1971 Collapse of an initially spherical vapour cavity in the neighbourhood of a solid boundary. *J. Fluid Mech.* **47** (2), 283–290.

Preston, A. T., Colonius, T. & Brennen, C. E. 2007 A reduced-order model of diffusive effects on the dynamics of bubbles. *Phys. Fluids* **19** (12), 123302.

Prosperetti, A., Crum, L. A. & Commander, K. W. 1988 Nonlinear bubble dynamics. *J. Acoust. Soc. Am.* **83** (2), 502–514.

Qiu, S., Ma, X., Huang, B., Li, D., Wang, G. & Zhang, M. 2018 Numerical simulation of single bubble dynamics under acoustic standing waves. *Ultrason. Sonochem.* **49**, 196–205.

Rayleigh, L. 1917 On the pressure developed in a liquid during the collapse of a spherical cavity. *Phil. Mag.* **34**, 94–98.

Regulagadda, K., Bakshi, S. & Das, S. K. 2017 Morphology of drop impact on a super-hydrophobic surface with macro-structures. *Phys. Fluids* **29**, 082104.

Reuter, F., Gonzalez-Avila, S. R., Mettin, R. & Ohl, C.-D. 2017*a* Flow fields and vortex dynamics of bubbles collapsing near a solid boundary. *Phys. Rev. Fluids* **2** (6), 064202.

Reuter, F., Lauterborn, S., Mettin, R. & Lauterborn, W. 2017*b* Membrane cleaning with ultrasonically driven bubbles. *Ultrason. Sonochem.* **37**, 542–560.

Reuter, F. & Mettin, R. 2018 Electrochemical wall shear rate microscopy of collapsing bubbles. *Phys. Rev. Fluids* **3** (6).

Rimai, D. S., Quesnel, D. J. & Busnaina, A. A. 2000 The adhesion of dry particles in the nanometer to micrometer-size range. *Colloids and Surfaces* **165**, 3–10.

Sanada, T., Ando, K. & Colonius, T. 2011 A computational study of high-speed droplet impact. *Fluid Dyn. Mater. Processing* **7** (4), 329–340.

Sanada, T. & Watanabe, M. 2015 Photoresist and thin metal film removal by steam and water mixed spray. *J. Photopolym. Sci. Technol.* **28** (2), 289–292.

Sanada, T., Watanabe, M., Shirota, M., Yamase, M. & Saito, T. 2008 Impact of high-speed steam-droplet spray on solid surface. *Fluid Dyn. Res.* **40** (7–8), 627–636.

Sasaki, H., Ochiai, N. & Iga, Y. 2016 Numerical analysis of damping effect of liquid film on material in high speed liquid droplet impingement. *Int. J. Fluid Machinery Systems* **9** (1), 57–65.

Sato, M., Sotoku, K., Yamaguchi, K., Tanaka, T., Kobayashi, M. & Nadahara, S. 2011 Analysis on threshold energy of particle removal in spray cleaning technology. *ECS Transactions* **41** (5), 75–82.

Saurel, R. & Abgrall, R. 1999 A multiphase Godunov method for compressible multifluid and multiphase flows. *J. Comput. Phys.* **150**, 425–467.

Schmidmayer, K., Petitpas, F., Daniel, E. & Favrie, N. 2017 A model and numerical method for compressible flows with capillary effects. *J. Comput. Phys.* **334**, 468–496.

Sharma, P., Flury, M. & Zhou, J. 2008 Detachment of colloids from a solid surface by a moving air-water interface. *J. Colloid Interface Sci.* **326** (1), 143–150.

Shima, A. & Tomita, Y. 1981 The behavior of a spherical bubble near a solid wall in a compressible liquid. *Ingenieur-Archiv* **51**, 243–255.

Shirota, E. & Ando, K. 2015 Estimation of mechanical properties of gelatin using a microbubble under acoustic radiation force. *J. Phys. Conf.* **656** (012001).

Shyue, K.-M. & Xiao, F. 2014 An eulerian interface sharpening algorithm for compressible two-phase flow: The algebraic thinc approach. *J. Comput. Phys.* **268**, 326–354.

Song, S., Soemoto, K., Wakimoto, T. & Katoh, K. 2014 A study on removal of infinitesimal particles on a wall by high speed air jet (numerical simulation of hydrodynamic removal force). *J. JSEM* **14**, s94–s100.

Strasberg, M. 1953 The pulsation frequency of nonspherical gas bubbles in liquids. *J. Acoust Soc. Am.* **25** (3), 536–537.

Stricker, L., Prosperetti, A. & Lohse, D. 2011 Validation of an approximate model for the thermal behavior in acoustically driven bubbles. *J. Acoust. Soc. Am.* **130** (5), 3243–3251.

Supponen, O., Obreschkow, D., Kobel, P., Tinguely, M., Dorsaz, N. & Farhat, M. 2017 Shock waves from nonspherical cavitation bubbles. *Phys. Rev. Fluids* **2** (093601).

Supponen, O., Obreschkow, D., Tinguely, M., Kobel, P., Dorsaz, N. & Farhat, M. 2016 Scaling laws for jets of single cavitation bubbles. *J. Fluid Mech.* **802**, 263–293.

Tatekura, Y., Fujikawa, T., Jinbo, Y., Sanada, T., Kobayashi, K. & Watanabe, M. 2015 Observation of water-droplet impacts with velocities of O(10 m/s) and subsequent flow field. *ECS J. Solid State Sci. Technol.* **4** (9), N117–N123.

Tatekura, Y., Watanabe, M., Kobayashi, K. & Sanada, T. 2018 Pressure generated at the instant of impact between a liquid droplet and solid surface. *R. Soc. Open Sci.* **5** (181101).

Thalakkotor, J. J. & Mohseni, K. 2016 Unified slip boundary condition for fluid flows. *Phys. Rev. E* **94** (023113).

Thompson, H. D., Webb, B. W. & Hoffman, J. D. 1985 The cell Reynolds number myth. *Int. J. Numer. Methods in Fluids* **5**, 305–310.

Thompson, K. W. 1987 Time dependent boundary conditions for hyperbolic systems. *J. Comput. Phys.* **68**, 1–24.

Thompson, P. A. 1972 *Compressible Fluid Dynamics*. USA: McGRAW-HILL.

Thompson, P. A. & Robbins, M. O. 1989 Simulations of contact-line motion: Slip and the dynamic contact angle. *Phys. Rev. Lett.* **63** (7), 766–769.

Thoroddsen, S. T., Thoraval, M. J., Takehara, K. & Etoh, T. G. 2011 Droplet splashing by a slingshot mechanism. *Phys. Rev. Lett.* **106** (3), 034501.

Tiwari, A., Freund, J. B. & Pantano, C. 2013 A diffuse interface model with immiscibility preservation. *J. Comput. Phys.* **252**, 290–309.

Tiwari, A., Pantano, C. & Freund, J. B. 2015 Growth-and-collapse dynamics of small bubble clusters near a wall. *J. Fluid Mech.* **775**, 1–23.

Tomita, Y. & Shima, A. 1986 Mechanisms of impulsive pressure generation and damage pit formation by bubble collapse. *J. Fluid Mech.* **169**, 535–564.

Tryggvason, G., Scardovelli, R. & Zaleski, S. 2011 *Direct Numerical Simulations of Gas-Liquid Multiphase Flows*. Cambridge University Press.

Tsuda, S., Hyodo, H. & Watanabe, S. 2015 Validation of bubble dynamics equation for a nano-scale bubble via molecular dynamics simulation. *J. Phys. Conf.* **656** (012039).

Visser, C. W., Frommhold, P. E., Wildeman, S., Mettin, R., Lohse, D. & Sun, C. 2015 Dynamics of high-speed micro-drop impact: numerical simulations and experiments at frame-to-frame times below 100 ns. *Soft Matter* **11** (9), 1708–1722.

Visser, C. W., Tagawa, Y., Sun, C. & Lohse, D. 2012 Microdroplet impact at very high velocity. *Soft Matter* **8** (41), 10732.

Visser, J. 1995 Particle adhesion and removal: A review. *Particulate Sci. Technol.* **13**, 169–196.

Vogel, A. & Lauterborn, W. 1988 Time-resolved particle image velocimetry used in the investigation of cavitation bubble dynamics. *Appl. Optics* **27** (No. 9), 1869–1876.

Vreugdenhil, C. B. 1982 The effect of the cell-Reynolds number in the numerical solution of the convection-diffusion equation. PhD thesis, Delft University of Technology.

Wal, R. L. V., Berger, G. M. & Mozes, S. D. 2006 The splash/non-splash boundary upon a dry surface and thin fluid film. *Exp. Fluids* **40** (1), 53–59.

Wang, Y.-C. & Brennen, C. E. 1999 Numerical computation of shock waves in a spherical cloud of cavitation bubbles. *J. Fluids Eng.* **121**, 872–880.

Warnez, M. T. & Johnsen, E. 2015 Numerical modeling of bubble dynamics in viscoelastic media with relaxation. *Phys. Fluids* **27** (6), 063103.

Watanabe, M., Sanada, T., Hayashida, A. & Isago, Y. 2009 Cleaning technique using high-speed steam-water mixed spray. *Solid State Phenomena* **145–146**, 43–46.

Weiss, D. A. & Yarin, A. L. 1999 Single drop impact onto liquid films: neck distortion, jetting, tiny bubble entrainment, and crown formation. *J. Fluid Mech.* **385**, 229–254.

Yamashita, T. & Ando, K. 2019 in press Low-intensity ultrasound-induced cavitation and streaming in oxygen-supersaturated water: Role of cavitation bubbles as physical cleaning agents. *Ultrason. Sonochem.* .

Yamashita, T., Yamauchi, R. & Ando, K. 2018 Progress in ultrasonic cleaning research. *Japanese J. Multiphase Flow* **32** (2).

Yang, Y. X., Wang, Q. X. & Keat, T. S. 2013 Dynamic features of a laser-induced cavitation bubble near a solid boundary. *Ultrason. Sonochem.* **20** (4), 1098–1103.

Yarin, A. L. & Weiss, D. A. 1995 Impact of drops on solid surfaces: self-similar capillary waves, and splashing as a new type of kinematic discontinuity. *J. Fluid Mech.* **283**.

Zeng, Q., Gonzalez-Avila, S. R., Dijkink, R., Koukouvinis, P., Gavaises, M. & Ohl, C.-D. 2018 Wall shear stress from jetting cavitation bubbles. *J. Fluid Mech.* **846**, 341–355.

Zhang, F., Busnaina, A. A., Fury, M. A. & Wang, S.-Q. 2000 The removal of deformed submicron particles from silicon wafers by spin rinse and megasonics. *J. Electron. Mater.* **29** (No. 2), 199–204.

Zoeteweij, M. L., van der Donck, J. C. J. & Verslus, R. 2009 Particle removal in linear shear flow: Model prediction and experimental validation. *J. Adhes. Sci. Tech.* **23**, 899–911.